Theoretical Investigations of Intersubband Relaxation in Quantum Wells

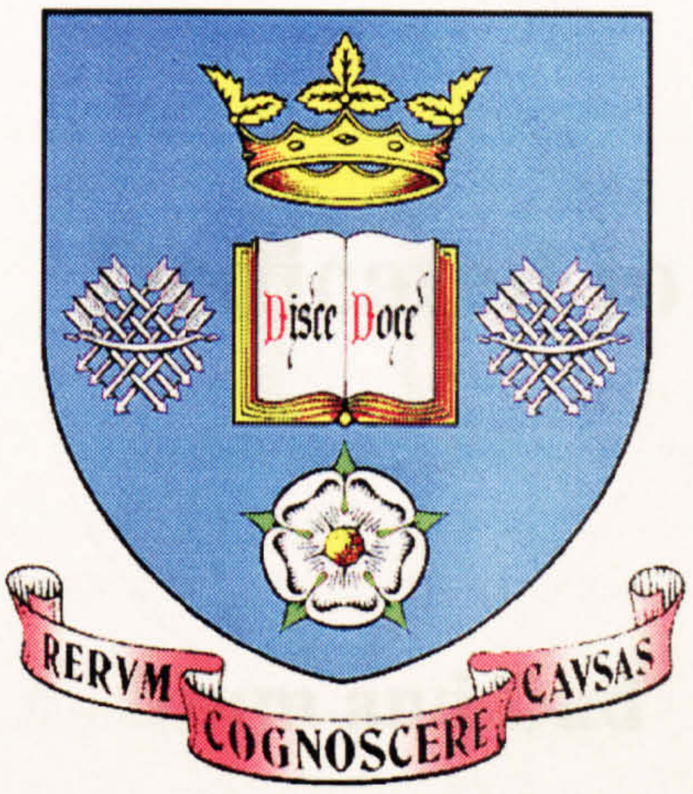

A thesis submitted in accordance with the requirements of the University of Sheffield for the degree of Doctor of Philosophy

by

Somporn Khan-ngern

Department of Physics & Astronomy

University of Sheffield

FEBRUARY 2002

Dedicated to

Mum and Dad

Theoretical Investigations of Intersubband Relaxation in Quantum Wells

Somporn Khan-ngern

Summary

In this thesis intersubband relaxation of electrons in quantum wells is theoretically investigated. Firstly, the in-plane kinetic energy, and also well width dependences of electron intra- or intersubband scattering rates (or times), associated by longitudinal optical (LO) phonon emission in a semiconductor single quantum well (SQW) structure are presented. Semi-analytic calculations are carried out for a GaAs/$Al_{0.3}Ga_{0.7}As$ SQW structure. The results show that the scattering rates (both for intra- and intersubband scattering) weakly depend on in-plane kinetic energy of the electron. Furthermore, the resulting calculations of well width dependence show that intrasubband scattering times gradually increase with well width contrasting with the intersubband scattering times which display a monotonic decrease.

A theoretical study of the condition to achieve inverted population in a semiconductor double quantum well (DQW) structure is also presented. The LO-phonon assisted tunneling rates, based on the Fröhlich interaction and Fermi's golden rule, has been performed for a GaAs/$Al_{0.3}Ga_{0.7}As$ DQW structure. The calculated results show that the tunneling rates monotonically decrease with the energy difference $E_1 - E_1^*$, and strongly depend on the magnitude of the transfer integral M.

This work has been extended to calculate the electron transport and its kinetics, due to various types of scattering and tunneling mechanisms in a triple barrier resonant tunneling structure (TBRTS). A system of coupled kinetic equations that describe the nonequilibrium electrons in the structure has been solved analytically to obtain subband distribution functions and gain spectra.

Finally, the concept of sequential tunneling has been introduced to explain an in-plane magnetic field dependence of resonant tunneling in a TBRTS. Typical current-voltage characteristics and derivatives for the TBRTS with particular design parameters have been calculated. It is found in the second derivative of the current that the resonance between E_1 and E_1^* is manifested as a visible feature in the background of a wide E_2 resonance. This feature has a sharp local maximum in the absence of applied magnetic field, and becomes flattened with increasing magnetic field in agreement with experiments.

Acknowledgements

I am first grateful to my supervisors Prof. G. J. Rees and Dr. I. A. Larkin for their constant guidance and support during the four years of work resulting in this thesis. I would also like to thank Dr. L. R. Wilson for his invaluable discussions and comments, following a very rapid reading of the manuscript. Thanks also go to my great friends, Mark and Rik for their skimming of the first draft of the manuscript.

I am also grateful to Dr. J. W. Cockburn and Prof. M. S. Skolnick for useful discussions and various support. I would also like to acknowledge the immensely financial support provided by the Royal Thai Government over the four years, and also the financial assistance given by the Department of Physics & Astronomy, University of Sheffield.

I am also eternally grateful for variously emotional support from my beloved friends, Diane, Doris and Kanchana. Thanks also go to all the people who have made my time in Sheffield enjoyable.

Most of all I am indebted to my wife and my son.

Contents

List of Figures

List of Tables

Chapter 1

Intersubband transitions in quantum wells

1.1 Outline of Thesis

This chapter begins with a brief introduction to semiconductor heterostructures, quantum wells (QWs) and superlattices. The remainder of the chapter describes intersubband transitions in QWs, which play an essential role in the lasing action in Quantum Cascade Laser (QCL) structures.

In Chapter 2, a microscopic lattice dynamic model is introduced to calculate scattering times for intra- and intersubband transitions due to electron-longitudinal-optical (LO)-phonon interaction in a single quantum well (SQW) structure. The scattering times are investigated in terms of in-plane kinetic energy of the electron. Well width dependence of the intersubband scattering times is also presented.

In Chapter 3, the technique developed in Chapter 2 is applied to calculate tunneling rates for interwell transitions due to electron-LO-phonon scattering in a double quantum well (DQW) structure. The focus is on the investigation of the tunnelling rates as a function of the difference in confinement energy between the states involved. The calculations are presented in an analytical form taking into account the different effective mass of the electron in the quantum well and barrier materials.

Chapter 4 applies the Boltzmann kinetic equation to the study of nonequilibrium electrons in DQW structures. The kinetic equation, which involves terms describing the electron-electron (e-e) and electron-LO-phonon (e-LO) scattering, as well as electron escape and electron generation processes, have been analytically solved for the subband distribution functions. The resulting calculations provide a comprehensive description of the lasing process in intersubband lasers.

Chapter 5 compares details experimental measurements with theoretical calculations for the tunneling current in a triple barrier resonant tunneling structures (TBRTS) incorporating asymmetric coupled QWs with magnetic field applied perpendicular to the direction of current flow.

Concluding remarks and future work relating to this work are presented in Chapter 6.

1.2 Heterostructures, quantum wells and superlattices

1.2.1 Heterostructures

Modern techniques of semiconductor crystal growth have resulted in what is known as band-gap engineering. Using III-V semiconductors Molecular Beam Epitaxy (MBE) and Metal-Organic Chemical Vapour Deposition (MOCVD) allow the growth of ultra thin layers of semiconductor materials with a controlled energy band gap. These layers can be grown epitaxially on top of one another providing there is a reasonable match of the crystal lattice constant between layers.

Continued developments of these techniques are currently the subject of a new field of semiconductor device research. Many new device structures such as Heterojunction Bipolar Transistors (HBT), High Electron Mobility Transistors (HEMT) and Resonant Tunneling Diodes (RTD), are designed using the principles of band-gap engineering. The RTD, which utilizes the electron-wave resonance occurring in double potential barriers, emerged as a pioneering device in this field [1,2]. The idea of resonant tunneling was extensively investigated both in a fundamental viewpoint and also its applications [3-6], shortly after MBE appeared in the research field of compound semiconductor crystal growth. Since then, the RTD has attracted a great amount of interests and has been investigated both from the standpoint of quantum transport physics and also its application in functional quantum devices. Despite its simple structure, the RTD is indeed a good laboratory for electron-wave experiments, which can investigate various manifestations of quantum transport in semiconductor nanostructures. It has played a significant role in disclosing the fundamental physics of the electron-wave in semiconductors, and enabling the study of more complex and

advanced quantum mechanical systems such as the electron intersubband transitions in QCL structures.

1.2.2 Quantum wells and superlattices

Band-gap engineering enables the production of conduction and valence bandedge profiles of a typical quantum well as shown in Figure 1.1(a). The barrier material has a larger band gap than the well material, causing the motion of electrons (e) and holes (h) in the growth direction to be restricted. The confinement potential quantizes the motion of the carriers (e or h) in the growth direction, giving rise to a number of dis-crete energy levels. These energy levels which are known as subband energies have an associated dispersion in the plane of the quantum well (for the idealised paralolic bands)

$$E_n(k_{xy}) = \varepsilon_n + \frac{\hbar^2 k_{xy}^2}{2m^*_{e(h)}} \quad ; \; n = 1,2,3,\cdots \tag{1.1}$$

where k_{xy} is the magnitude of in-plane wavevector of e or h, $m^*_{e(h)}$ is the effective mass, and ε_n is the energy at the bottom of the nth subband. In the infinitely deep well approximation the confinement energy ε_n is simply $\frac{\hbar^2}{2m^*_{e(h)}}\left(\frac{n\pi}{L}\right)^2$; $n = 1,2,3,\cdots$, where L stands for the well width.

In addition, modern crystal growth techniques also allow the growth of multiple quantum well (MQW) structures, which are schematically shown in Figure 1.1(b). This structure can be formed by periodic variation of alloy composition during crystal growth. For a MQW consisting of a series of quantum wells separated by barriers wide enough that wavefunction of a carrier in one well does not penetrate into an adjacent well each well has the same eigenstates as would an individual well; *i.e.* they are effec-tively isolated from one another. When the barrier thickness decreases, the probability of an electron tunneling from one well to another increases; *i.e.* the wave function of the carrier in one well can be non-zero in an adjacent well. For a structure consisting of two such wells separated by a thin barrier the eigenstates split into two. For N such wells the splitting gets into N states. As N increases a continuous distribution of

allowed states, called a *miniband*, is formed. The formation of these minibands is exactly analogous to the formation of bands in the tight binding model of bulk semiconductors. Such a structure is known as a *superlattice*.

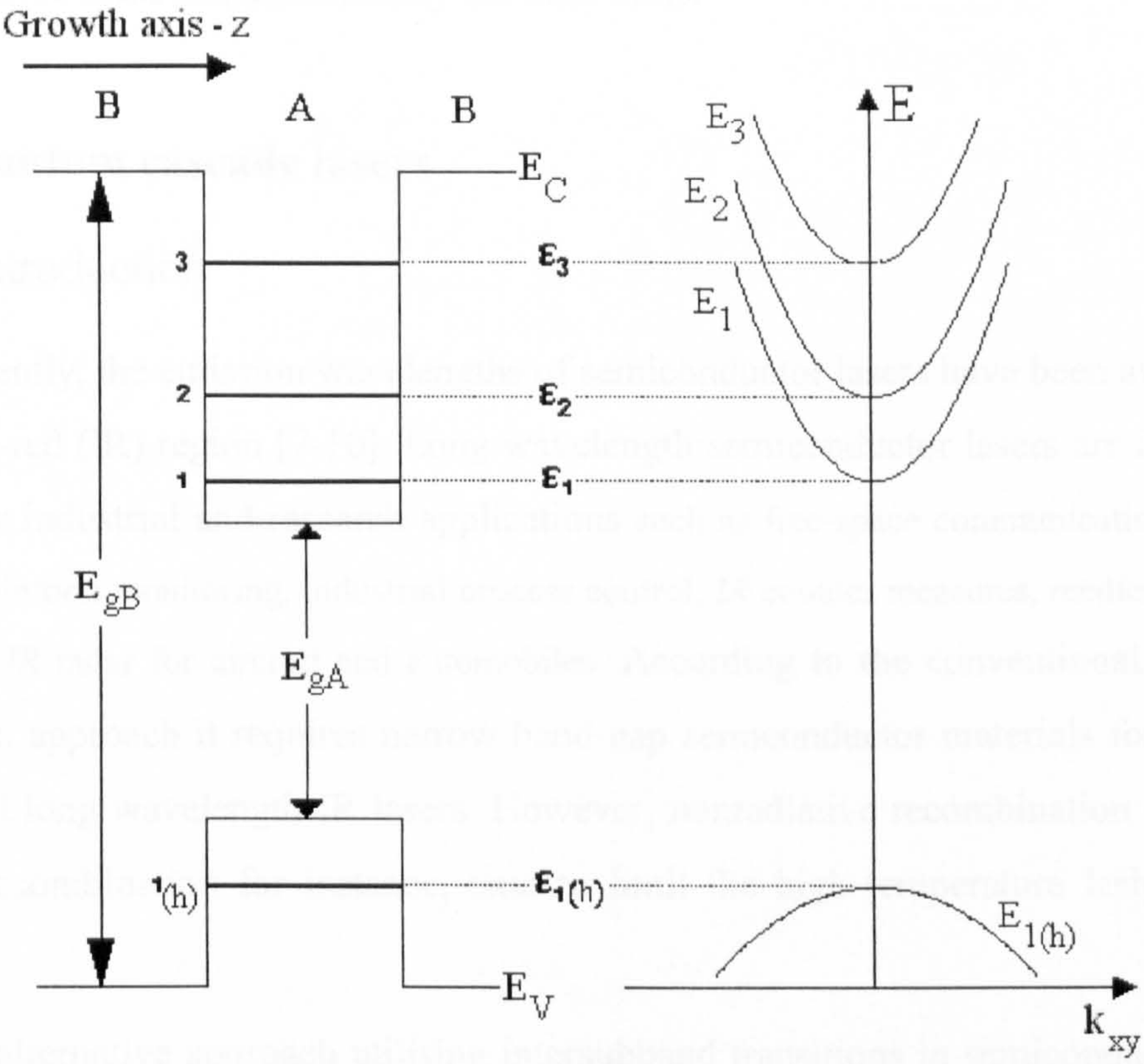

(a) Quantum well heterostructure

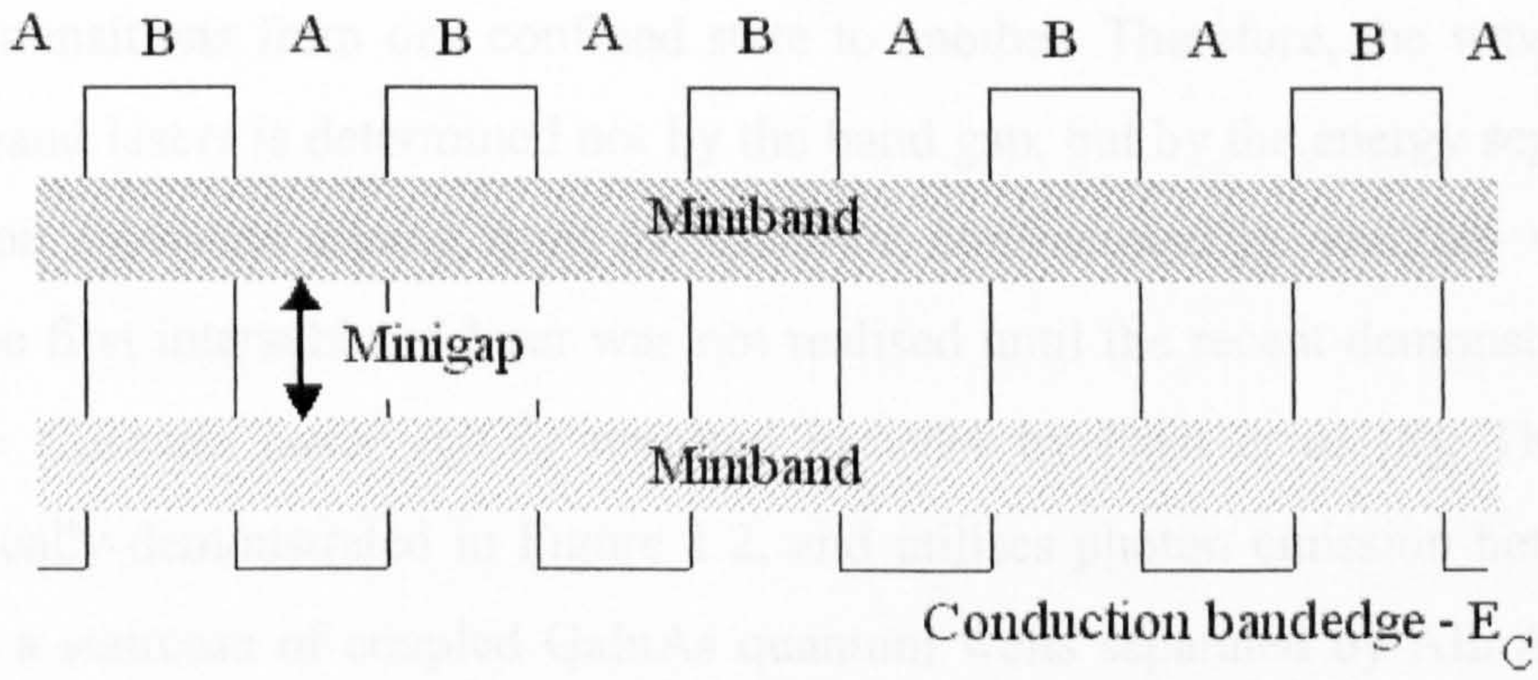

(b) Superlattice

Figure 1.1 Conduction bandedge profiles of **(a)** a SQW heterostructure with the idealised parabolic dispersions of electrons (or holes), and **(b)** a superlattice formed by periodic variation of alloy (materials A and B) composition during crystal growth processes with the resulting minibands and minigap.

The superlattice can be viewed as a bulk material which has its periodicity in one direction modified resulting in both the dispersion energy in the growth direction and also the effective mass of the carriers being modified. When the barriers are very thin this effective mass is approximately the bulk mass.

1.3 Quantum cascade lasers

1.3.1 Introduction

Recently, the emission wavelengths of semiconductor lasers have been available in the infra-red (IR) region [7-10]. Long wavelength semiconductor lasers are in demand for many industrial and research applications such as free-space communications, atmospheric pollution monitoring, industrial process control, *IR* counter measures, medical diagnostics, and *IR* radar for aircraft and automobiles. According to the conventional interband transition approach it requires narrow band-gap semiconductor materials for realising mid- and long wavelength IR lasers. However, nonradiative recombination processes, Auger recombination for instance, tend to limit the high temperature lasing performance.

An alternative approach utilising intersubband transitions in semiconductor quantum well structures for long wavelength IR lasers was first suggested in 1972 by Kazarinov and Suris [7]. In this unipolar structure coherent photons are generated by electron transitions from one confined state to another. Therefore, the wavelength of intersubband lasers is determined not by the band gap, but by the energy separation of conduction subbands arising from the quantum confinement in quantum well structures. The first intersubband laser was not realised until the recent demonstration of a *Quantum Cascade Laser (QCL)* reported in 1994 by Faist *et al* [8]. The QCL is schematically demonstrated in Figure 1.2, and utilises photon emission between subbands in a staircase of coupled GaInAs quantum wells separated by AlInAs barriers. Each injected electron is recycled, ideally producing an additional photon, as it cascades through each period of the laser.

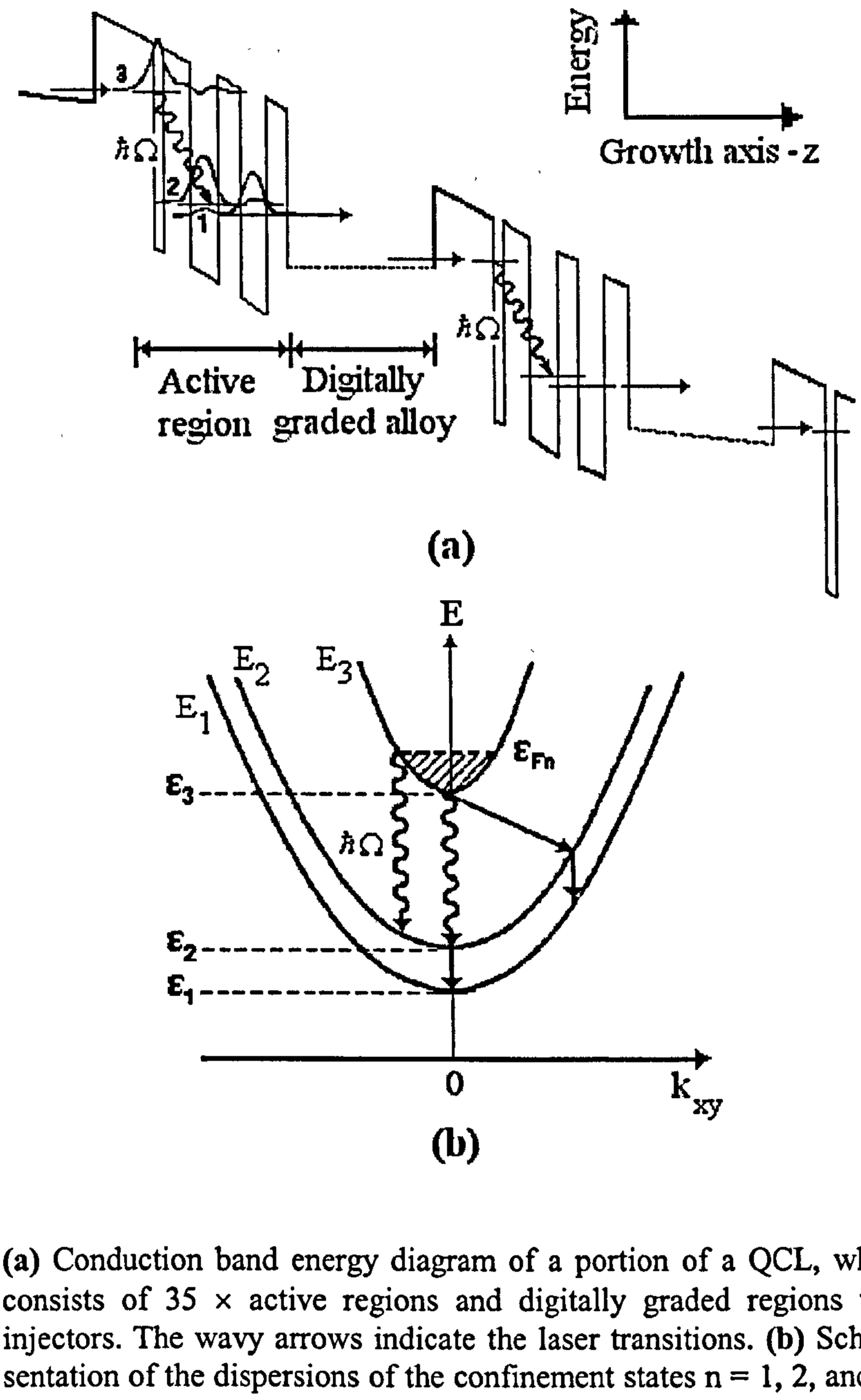

Figure 1.2 **(a)** Conduction band energy diagram of a portion of a QCL, which typically consists of 35 × active regions and digitally graded regions which act as injectors. The wavy arrows indicate the laser transitions. **(b)** Schematic representation of the dispersions of the confinement states n = 1, 2, and 3 parallel to the QW plane; k_{xy} is the corresponding in-plane wave vector of electron. The bottom of these subbands correspond to energy levels n = 1, 2, and 3 indicated in (a). The wavy arrows indicate all radiative transitions originating from the electron population in the subband n = 3 down to the subband n = 2. The quasi-Fermi energy ε_{Fn} corresponding to the population inversion at threshold measured from the bottom of the n = 3 subband. The straight arrows represent the intersubband nonradiative transitions due to LO-phonon scattering processes [8].

The main obstacle to achieving the intersubband lasing is nonradiative relaxations between subbands due to optical phonon scattering (discussed in more detail later in the following chapters). The typical phonon relaxation time (~ 1 ps) is much shorter than the radiative time, which is longer than 1 ns, resulting in a very low radiative efficiency ($<10^{-3}$). However, specially designed multiple barrier heterostructures can provide population inversion that giving rise to lasing without reducing the current injection efficiency.

In the following subsection the basic principles of intersubband transitions in QWs, and also some basic aspects of quantum effects and relaxation processes in semiconductor nanostructures, which play an essential role in the QCL are presented.

1.3.2 Basic principles of intersubband transitions in quantum wells

According to whether the optical transition is between quantum states in adjacent QWs, so-called *interwell* photon-assisted tunneling transitions shown in Figure 1.3(a), or between states in the same QW, so-called *intrawell* transitions shown in Figure 1.3(b), the approaches towards intersubband lasing can be devided in two categories [9,10]. The interwell photon-assisted tunneling transition, originally suggested for generating and amplifying IR light by Kazarinov and Suris [7], occurs between the ground state of a QW and one of the excited states of the adjacent well in a superlattice structure under an external electric field parallel to the growth direction. A population inversion can be easily established between the two quantum states due to the barrier-separated feature of the two states, and the laser energy can be tuned over a wide range by varying the electric field strength. However, since the overlap of their wavefunctions is quite small, the transition rate between the two states is small, and a high electron injection is required to obtain sufficient gain to overcome losses in the system, leading to a very high threshold current.

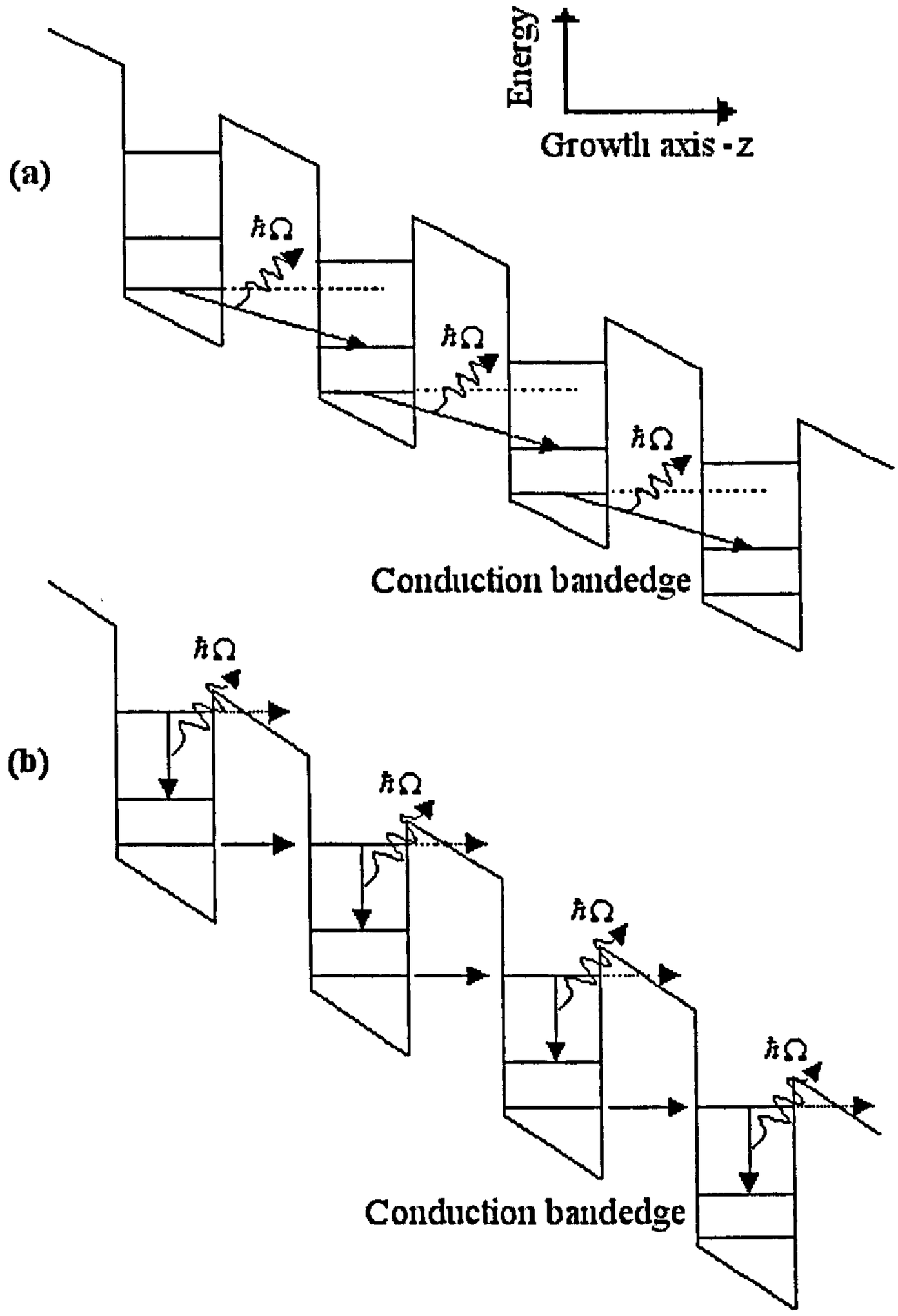

Figure 1.3 Illustrations of optical intersubband transitions: **(a)** interwell photon-assisted tunneling transitions, and **(b)** intrawell transitions associated with electron resonant tunneling between QWs [9].

In the second scheme, the intrawell optical transition rate is much larger, but the nonradiative relaxation between the two states in the same well is also faster, which results in difficulties in achieving population inversion between the two states. For a clear comparison between the two approaches, it is helpful to have a more analytic evaluation. Starting from the lasing threshold gain condition [9,11]

$$\Gamma_{opt} \cdot g_{th} = \alpha_m + \alpha_i \ , \tag{1.2}$$

where Γ_{opt} is the optical confinement factor, g_{th} is the gain at threshold, α_m is the mirror losses due to finite facet reflectivity, and α_i is the internal losses for the optical wave which results from various mechanisms such as free-carrier absorption and scattering at the heterostructure interfaces. Since α_i, α_m, and Γ_{opt} are mainly concerned with the optical wave in the QW structure, it can be assumed that α_i, α_m, and Γ_{opt} would not be significantly affected by the different transition schemes (inter- or intra-well transitions). Thus, the same threshold gain g_{th} is required in the two approaches. How the threshold gain is reached differs in the two approaches?

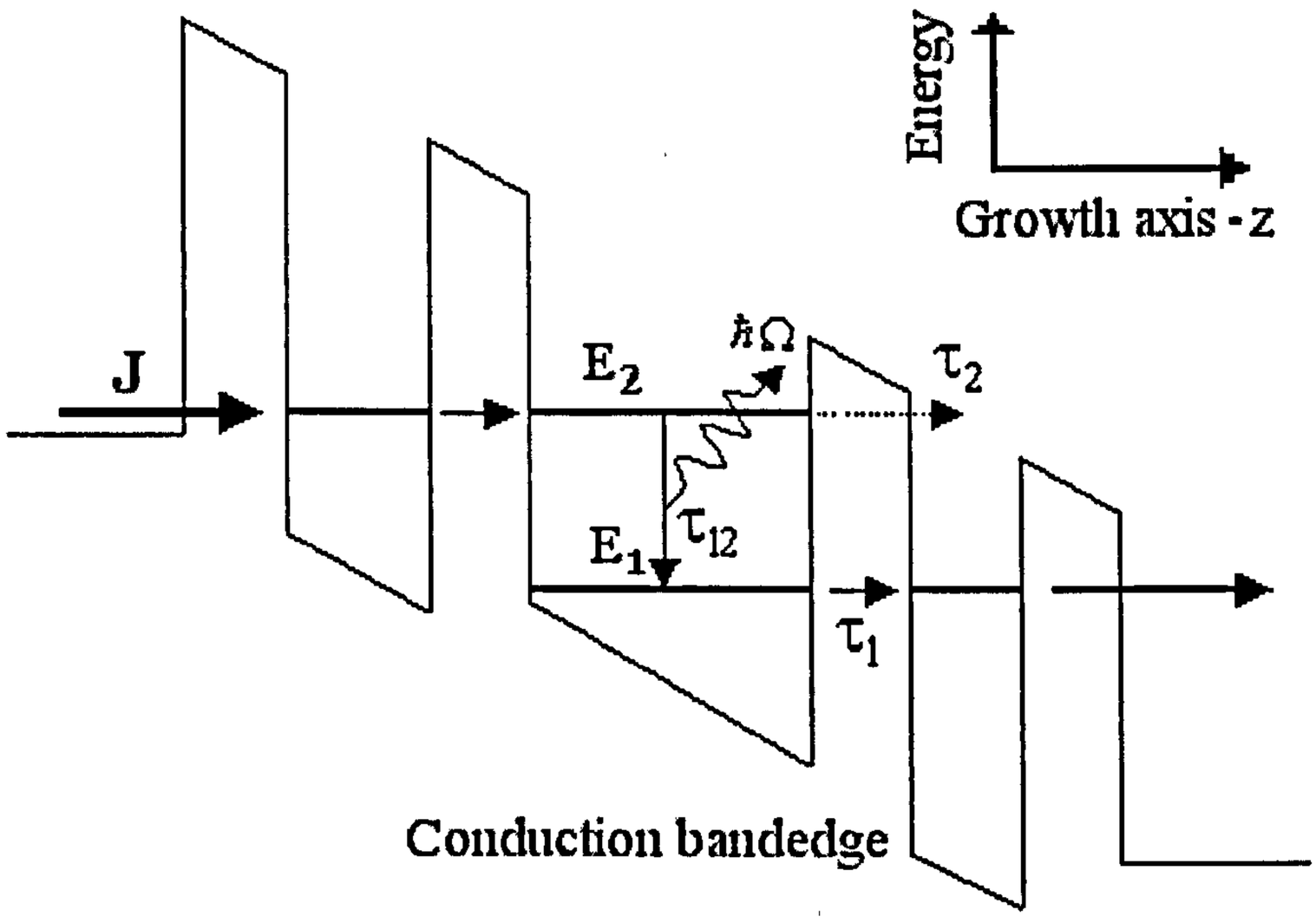

Figure 1.4 Schematic diagram of a QCL structure with a wide well as the lasing unit and two narrow QWs as the electronic energy filters by resonant tunneling [9].

Considering the steady state of a two-level system shown in Figure 1.4, one can obtain

$$n_2 - n_1 = \frac{J}{e}\left(\frac{\tau_2}{\tau_2 + \tau_{12}}\right)(\tau_{12} - \tau_1) \tag{1.3}$$

where n_1 is the electron density at the the lower energy level E_1, n_2 the electron density at the upper energy level E_2, J the current density injected into the upper level, τ_1 the electron lifetime at the lower level, τ_{12} the electron relaxation (including nonradiative and radiative contributions) time from E_2 to E_1, and τ_2 is the time

required for an electron in the upper level to escape from the well in ways other than through the lower level.

From Eq.(1.3), it is clear that the relaxation τ_{12} must be longer than the electron lifetime τ_1 in order to establish the population inversion, which is essential to intersubband lasing. Since the overlap wavefunctions between two states in adjacent wells is smaller, the relaxation time τ_{12} for the interwell transition is longer than the relaxation time τ_{12} for the intrawell transition, and thus population inversion can be established more easily by the interwell photon-assisted tunneling transition. Additionally, due to the longer relaxation time τ_{12}, the escape time τ_2 at the upper level, which is approximately the same in the two transition schemes, has a more significant impact in reducing the current injection efficiency in the case of interwell transition. If the lifetime τ_1 at the lower level is much smaller than the relaxation time τ_{12} in either case, one can show that the threshold current density for intrawell transitions is lower than the threshold current density for interwell transitions. Therefore, it is preferable to make the lower level lifetime τ_1 much smaller than the relaxation time τ_{12} and use the intrawell transition approach to intersubband lasing to achieve a low threshold current. However, reducing the lifetime at the lower level to a value much smaller than the relaxation time without affecting the current injection efficiency is a difficult task.

Since the typical value of the electron relaxation time τ_{12}, due to LO phonon emission between subbands with energy separation higher than the LO phonon energy ($\varepsilon_{LO} \approx 36\,\text{meV}$ for GaAs QW), is of the order of 1 ps [12-14], a sufficiently thin barrier layer is required for the lower lifetime τ_1 to be smaller than τ_{12}. However, such a thin barrier layer does not provide good confinement of electrons in the upper level, leading to large leakage current. Modified QW structures with alternating wide and narrow well acting as electronic energy filters, have been suggested to overcome this problem [15-17]. Here energy filters selectively inject and remove electrons via resonant tunneling as schematically shown in Figure 1.4. However, because the nonradiative relaxation by LO phonons is so fast, a sufficient population inversion cannot be easily achieved without a large amount of current injection and careful device design.

In the far-IR spectrum, the dominant nonradiative relaxation τ_{ac}, via acoustic phonon scattering between subbands, is on the order of 100 ps. Thus the population inversion can be achieved more efficiently, and the radiative efficiency could be raised. Making use of the difference in the relaxation times above and below the optical phonon energy for stimulated far-IR emission in a multilevel scheme has been suggested by Andronov [16], and can be constructed in DQW system made of a narrow well as the injected current region, and a wide well as the lasing region. Since the energy separation between subbands is smaller, thermal fluctuation may be a serious problem in far-IR lasing action, and low operating temperatures may be required. In contrast, in the wavelength ranges of the mid-IR spectrum, the nonradiative relaxation of electrons between subbands by optical phonon scattering is unavoidable. Therefore, in order to achieve intersubband lasing in practice at these wavelengths, it is highly desirable to suppress the nonradiative decay processes in QWs. A common feature shared by these two approaches, whether the transition is interwell or intrawell, is that the electron transport in the QW structures is based on conventional intraband tunneling, in which a delicate balance is attempted to simultaneously fulfill two essentially distinct physical requirements for the realisation of an efficient population inversion [17], which are good confinement of electrons at the upper energy level and a fast electron tunneling rate at the lower level. This leads us to get through problems in practical implementation.

The goal of this thesis is to generalize theoretical explanations of electron relaxation in the QCL operation, and also study how to design a QCL structure to achieve a high radiative efficiency with a low threshold current thus optimizing its performance and operating temperature.

Chapter 2

Longitudinal optical phonon scattering in single quantum well structures

In this chapter in-plane kinetic energy, and also well width dependence of electron scattering times; both for intra- and intersubband scattering, due to LO phonon emission in semiconductor SQW structures are investigated. The focus is on comparisons between the intra- and intersubband scattering times of electrons in a QW. The results have been performed for GaAs/$Al_xGa_{1-x}As$ material systems, which are of considerable experimental interest. In addition, a comparison of the scattering times calculated using the semi-analytic approach described in this chapter with the numerical results reported in Ref. 12 by Ferreira and Bastard is also presented.

2.1 Introduction

Electron-phonon interaction in polar semiconductor QWs has attracted a great amount of interest both from a fundamental viewpoint and also due to its importance for device performance. For instance, the cooling of photoexcited carriers, carrier tunneling, and the mobility of high-speed heterostructure devices are primarily governed by the scattering of electrons associated with LO phonons. The investigation of this interaction has been studied using either a dielectric continuum model [18-24] or microscopic lattice dynamic models [25-30]. Dielectric continuum model ignores the effect of individual layers of atoms but it has the considerable advantage of making the interaction very simple. In some parameter regimes, the use of dielectric continuum model is well established and the electron scattering times calculated by using this model compare well with experimental results [31-33]. However, scaling of the

electron-LO-phonon interaction with diminishing device length presents a serious challenge to the accurate use of such model. As a result, there has recently been an increasing need for more rigorous analysis and detailed knowledge of electron-LO-phonon interactions in reduced dimensional systems. This has been the main motivation for the emergence of *ab initio* microscopic models [28,29]. Though such models provide the most accurate analysis of the structure, they have not been used extensively. This can attributed to the fact that the *ab initio* microscopic analysis involves very arduous and time consuming first-principle calculations of lattice dynamics [34,35] rather than employing adjustable parameters [36,37].

2.2 LO-Phonon scattering in single quantum well structures

In general, any device can be viewed as a complex array of scatterers shown in Figure 2.1. The time-dependent Schrödinger equation, including the microscopic time-varying scattering potential $U_s(\vec{r},t)$ due to the entire array of scatterers is [38]

$$i\hbar\frac{\partial\Psi(\vec{r},t)}{\partial t} = \left[-\frac{\hbar^2}{2m^*}\nabla^2 + E_C(\vec{r}) + U_s(\vec{r},t)\right]\Psi(\vec{r},t) = E\Psi(\vec{r},t)\ , \qquad (2.1)$$

where $E_C(\vec{r})$ is the conduction bandedge energy profile, m^* the electron effective mass, and Ψ is the electron wavefunction with the corresponding total energy E.

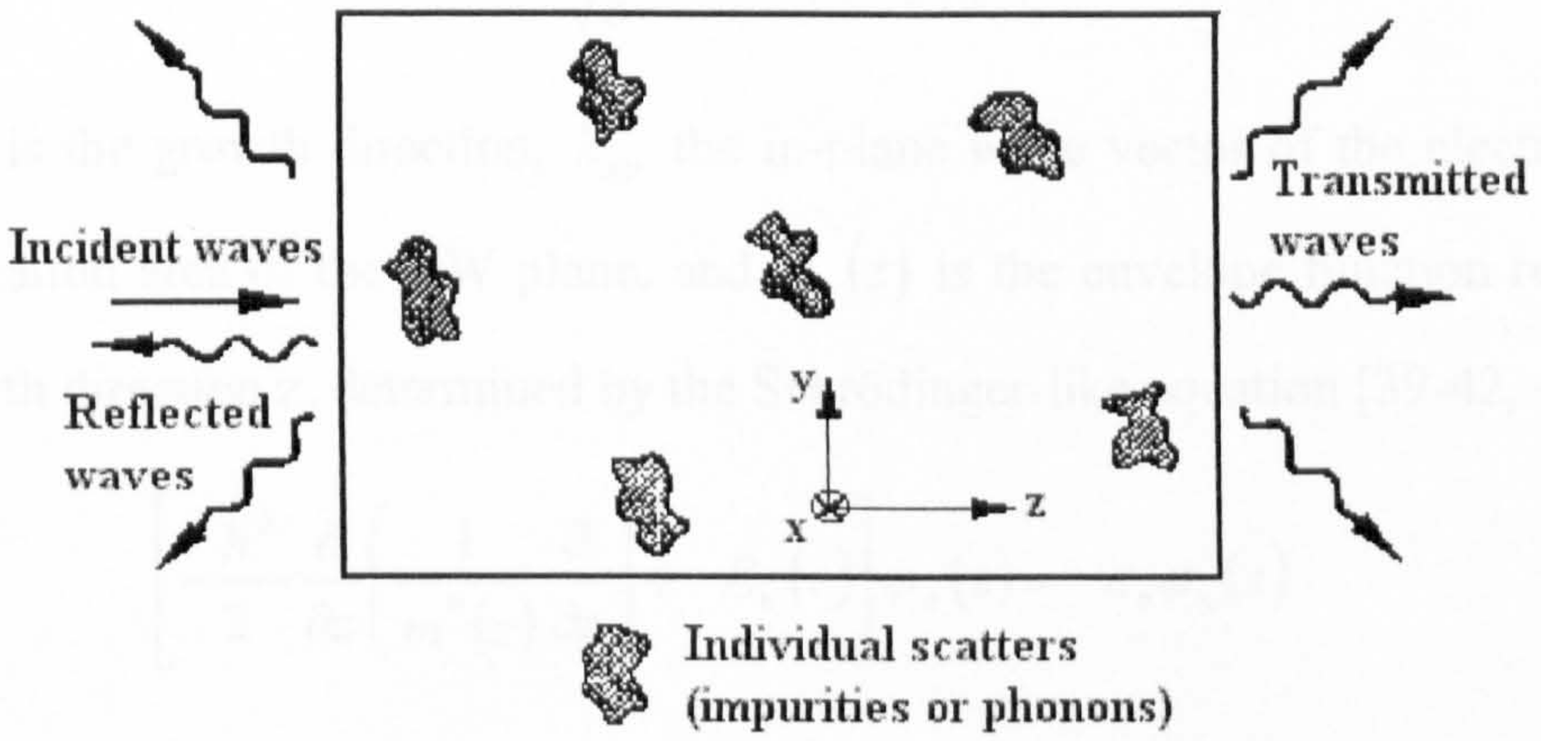

Figure 2.1 Transmission of electrons through a device with a scattering potential $U_s(\vec{r},t)$ composed of localised scattering potentials due to individual scatterers (impurities or phonons) [38].

2.2.1 Electron confinement in a SQW structure

With modern epitaxial growth techniques, the alloy composition can be varied on an atomic scale to produce structures such as that shown in Figure 2.2. The structure consists of a narrow band-gap semiconductor (material B) layer embedded between two wider band-gap (materials A and C) layers resulting in the band discontinuities, which are such that the motion of both types of carriers (e or h) in the growth direction is restricted. The electron confinement energies in the conduction band can be calculated in the envelope function approximation [39-42], using a Kane model [43] for describing the electron states of the parent A, B and C materials [44]. The electron wave function in each layer takes the form

$$\Psi^{A,B,C}(\vec{r}) = \sum_{n} u_n^{A,B,C}(\vec{r})\chi_n(\vec{r}) \tag{2.2}$$

where $\chi_n(\vec{r})$ is the envelope wavefunction, and $u_n^{A,B,C}(\vec{r})$ is the Bloch wave function in the A, B or C material.

By adopting a single-band spherical-effective-mass model to such the quasi-two-dimensional (quasi-2D) electrons and take as simplified boundary conditions on the envelope function with a periodic boundary condition in the QW plane, the envelope function $\chi_n(\vec{r})$ can be factorised

$$\chi_n(\vec{r}) = \frac{1}{\sqrt{S}}\exp(i\vec{k}_{xy}\cdot\vec{r})\varphi_n(z) \quad , \tag{2.3}$$

where z is the growth direction, $\vec{k}_{xy}$ the in-plane wave vector of the electron, S the normalization area of the QW plane, and $\varphi_n(z)$ is the envelope function restricted in the growth direction z, determined by the Schrödinger-like equation [39-42, 45]

$$\left[-\frac{\hbar^2}{2}\frac{\partial}{\partial z}\left(\frac{1}{m^*(z)}\frac{\partial}{\partial z}\right)+ E_c(z)\right]\varphi_n(z)= \varepsilon_n\varphi_n(z) \tag{2.4}$$

where $m^*(z)$ is the electron effective mass depending on z, $E_c(z)$ the conduction bandedge energy profile, and ε_n is confinement energy of the nth subband.

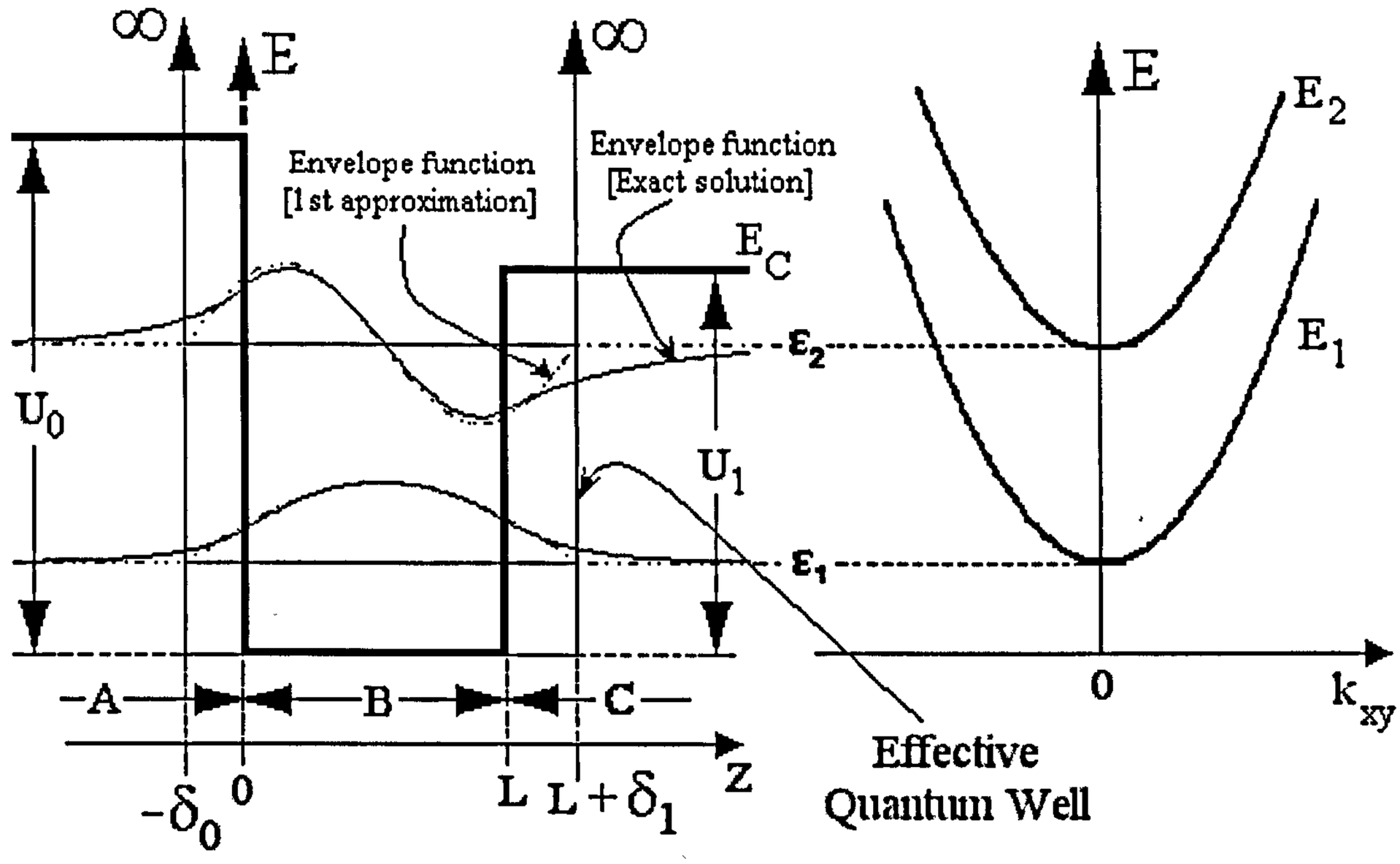

Figure 2.2 Schematic conduction bandedge profile of a SQW structure, which consists of A, B and C material with energy levels and the simplified envelope functions $\varphi_n(z)$, and also the associated total energy including the in-plane kinetic energy for each subband.

According to the connection rules it is necessary to have boundary conditions at the interfaces as follows: $\varphi_n(z)$ and $\frac{1}{m^*(z)}\left[\frac{\partial \varphi_n(z)}{\partial z}\right]$ are continuous [39,42,46-52]. The continuity of $\frac{1}{m^*(z)}\left[\frac{\partial \varphi_n(z)}{\partial z}\right]$ is necessary for the conservation of particle current passing through the surfaces in place of the usual continuity of the derivative of φ_n as derived in quantum mechanics textbooks. With these relevant boundary conditions the Schrödinger-like equation Eq.(2.4) can be exactly solved to yield the envelope functions and subband energies [39,45,47]. However, to make the results more practical it is very useful to take into account the finite barrier height in first approximation that gives for the effective well width [39,42,46-53]

$$L_{eff} = L + \delta_0 + \delta_1 , \qquad (2.5)$$

where L is the well width (material B), and

$$\left.\begin{aligned} \delta_0 &= \frac{\hbar}{\sqrt{2\left(m_B^* / m_A^*\right) m_B^* U_0}} \\ \delta_1 &= \frac{\hbar}{\sqrt{2\left(m_B^* / m_C^*\right) m_B^* U_1}} \end{aligned}\right\} , \tag{2.6}$$

here m_A^*, m_B^* and m_C^* are the electron effective masses of the materials A, B and C, respectively. U_0 and U_1 are the heights of the barriers adjusted to the QW; see also Figure 2.2.

As a consequence of the appropriate approximation above, solutions of Eq. (2.4) are obtained

$$\varphi_n(z) = \begin{cases} 0 & ; \; z < -\delta_0 \\ \sqrt{\dfrac{2}{L_{eff}}} \sin\left[k_z\left(z+\delta_0\right)\right] & ; -\delta_0 < z < L+\delta_1 \\ 0 & ; \; z > L+\delta_1 \end{cases} \tag{2.7}$$

where $k_z = \dfrac{n\pi}{L_{eff}}$; $n = 1,2,3,\cdots$; and the total electron energy associated with the state $\left|n, k_{xy}\right\rangle \equiv \chi_n\left(\vec{r}\right)$ is therefore

$$E_n\left(k_{xy}\right) = \frac{\hbar^2 k_{xy}^2}{2m_B^*} + \varepsilon_n \quad , \tag{2.8}$$

$$\varepsilon_n = \left(\frac{\hbar^2}{2m_B^*}\right)\left(\frac{\pi}{L_{eff}}\right)^2 n^2 \qquad ; \; n = 1,2,3,\cdots \tag{2.9}$$

In fact, this approach works well if the barriers are high enough; *i.e.* $\left(\dfrac{\hbar^2}{2m_B^*}\right)\left(\dfrac{\pi}{L_{eff}}\right)^2 \ll U_0, U_1$.

A symmetric SQW system, which consists of a single GaAs layer embedded between two thick $Al_xGa_{1-x}As$ layers, is now considered. The band-gap energy for $Al_xGa_{1-x}As$ is larger than that for GaAs. This results in the change of band gap energy (ΔE_g) being distributed between the conduction and valence bandedges. Thus,

$$\Delta E_g = E_g^{AlGaAs} - E_g^{GaAs} = \Delta E_C + \Delta E_V \quad , \tag{2.10}$$

where E_g^{AlGaAs} and E_g^{GaAs} are band-gap energies for $Al_xGa_{1-x}As$ and for GaAs, respectively. ΔE_C and ΔE_V are the conduction and valence band-offset, respectively. For such a long time it was believed that ΔE_C was $\approx 88\%$ of ΔE_g [45]. However, in recent years there has been a lot of argument over this, and it now seems that the figure is closer to 60% [38, 54-56].

For small *Al* contents ($0 \le x \le 0.45$) [55] :

$$\left.\begin{aligned} E_g^{AlGaAs}(x) &= 1.424 + 1.247x \qquad \text{(in eV units)} \\ m^*_{AlGaAs}(x) &= (0.067 + 0.083x)m_0 \end{aligned}\right\} , \tag{2.11}$$

where m^*_{AlGaAs} is the effective mass of electrons in $Al_xGa_{1-x}As$ materials, and m_0 is the free electron mass.

Table 2.1 Some useful material parameters of the $GaAs/Al_xGa_{1-x}As$ heterostructures.

Al contents	Effective masses	Changes of the band-gap energy	Conduction band-offset	Valence band-offset
x	m^*_{AlGaAs}	ΔE_g [meV]	ΔE_C [meV]	ΔE_V [meV]
0	$0.067\,m_0$	0	0	0
0.1	$0.075\,m_0$	125	75	50
0.2	$0.084\,m_0$	249	150	99
0.3	$0.092\,m_0$	374	224	150
0.40	$0.100\,m_0$	499	299	200
0.45	$0.104\,m_0$	561	337	224

2.2.2 Electron LO-phonon interactions: Fröhlich interactions

According to the microscopic lattice dynamical model, the electrons are described by the Hamiltonian [57]

$$\hat{H} = \hat{H}_0 + \hat{H}_{ph} + \hat{H}_{e-ph} \quad , \tag{2.12}$$

where $\hat{H}_0$ is a single-particle Hamiltonian

$$\hat{H}_0 = \frac{\hbar^2}{2m^*}\nabla^2 + U(\vec{r}) \quad , \tag{2.13}$$

here the potential energy $U(\vec{r})$ includes the electrostatic potential and conduction bandedge discontinuity, and $m^*(\vec{r})$ is the electron effective mass. $\hat{H}_{ph}$ is the Hamiltonian representing for a phonon bath maintained in thermodynamic equilibrium,

$$\hat{H}_{ph} = \sum_{\vec{q}} \hbar\omega_{\vec{q}} \left(a_{\vec{q}}^{+} a_{\vec{q}} + \frac{1}{2} \right) \quad , \tag{2.14}$$

and $\hat{H}_{e-ph}$ is the electron-phonon interaction given by

$$\hat{H}_{e-ph} = \frac{1}{\sqrt{V}} \sum_{\vec{q}} \alpha(\vec{q}) e^{i\vec{q}\cdot\vec{r}} \left(a_{\vec{q}}\, e^{-i\omega t} + a_{-\vec{q}}^{+}\, e^{i\omega t} \right), \tag{2.15}$$

where $\vec{q} \equiv \vec{Q} + \vec{q}_z$ is the phonon wave vector; here $\vec{Q}$ stands for in-plane phonon wave vector, and $\vec{q}_z$ the phonon wave vector in z direction. $a_{\vec{q}}$ and $a_{-\vec{q}}^{+}$ are the phonon annihilation and creation operators, respectively. $\alpha(\vec{q})$ is a coupling strength for a phonon of mode $\vec{q}$, ω the phonon angular frequency, and V is the normalization volume.

According to Fermi's golden rule, the scattering rates of an electron from an initial state $\left|m, k_{xy}^{i}\right\rangle$ in the mth subband to all final states $\left|n, k_{xy}^{f}\right\rangle$ in the nth subband accompanied by emission (or absorption) of a phonon with energy $\hbar\omega$ is [12,58,59]

$$\frac{1}{\tau_i} = \frac{2\pi}{\hbar} \int \left| \left\langle n, k_{xy}^{f} \middle| \hat{H}_{e-ph} \middle| m, k_{xy}^{i} \right\rangle \right|^2 \delta\left(E_i - E_f \mp \hbar\omega\right) dN_f \quad , \tag{2.16}$$

where the upper (lower) sign refers to emission (absorption) of the phonon. E_i and E_f are the total energies of the electron at initial and final states, respectively. In this expression the integration is done over the final density of states N_f. The illustration of scattering processes involving the LO phonon allowed by conservation of energy and conservation of momentum in the xy-plane is shown in Figure 2.3.

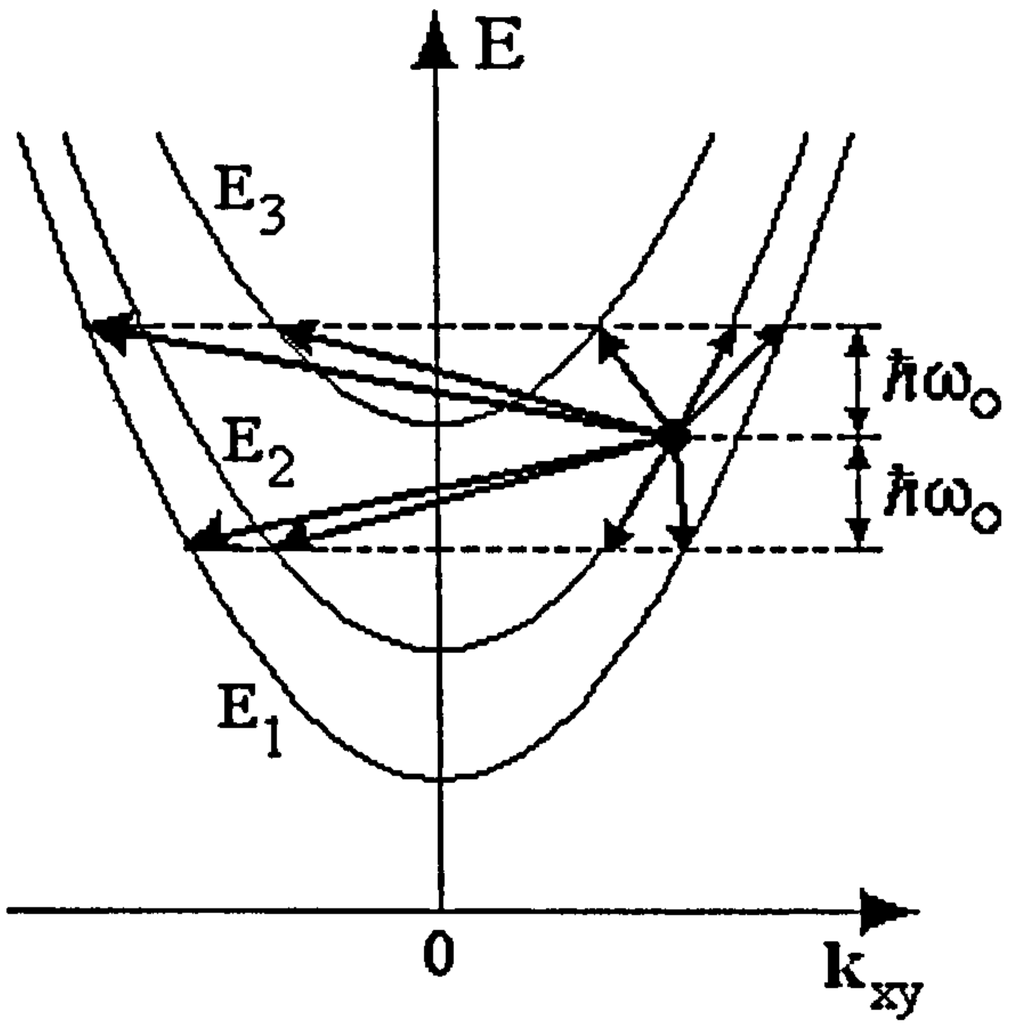

Figure 2.3 Illustration of scattering processes involving an LO phonon allowed by conservation of energy and conservation of momentum in the xy-plane.

For the LO-phonon scattering mode, the coupling strength $\alpha(\vec{q})$ is given by [19, 60,61]

$$|\alpha(\vec{q})|^2 = 2\pi \frac{\hbar\omega_0}{q^2}\left(\frac{e^2}{4\pi\varepsilon_0}\right)\left[\frac{1}{\kappa_\infty} - \frac{1}{\kappa_0}\right] \quad \text{(in SI units)}\ , \qquad (2.17)$$

where κ_∞ and κ_0 are the high-frequency and static dielectric constants of the QW, ε_0 the permittivity of vacuum, e the electronic charge, and $\hbar\omega_0$ is the LO-phonon energy. Using Eqs. (2.15), (2.16) and (2.17) the electron LO-phonon scattering rates from an initial state $\left|m,k_{xy}^{i}\right\rangle$ in the mth subband to all final states $\left|n,k_{xy}^{f}\right\rangle$ in the nth subband is therefore [12,60]

$$\frac{1}{\tau_i} = C_0 \iint I_{mn}(Q)\left[(N_0+1)\delta\left(E_i - E_f - \hbar\omega_0\right) + N_0\delta\left(E_i - E_f + \hbar\omega_0\right)\right] d^2k_{xy}^f , \quad (2.18)$$

$$C_0 = \frac{2\pi}{\hbar}\frac{1}{(2\pi)^3}(2\pi\hbar\omega_0)\left(\frac{e^2}{4\pi\varepsilon_0}\right)\left[\frac{1}{\kappa_\infty} - \frac{1}{\kappa_0}\right], \quad (2.19)$$

$$N_0 = \frac{1}{\exp\left(\dfrac{\hbar\omega_0}{k_B T}\right) - 1} , \quad (2.20)$$

$$Q = \sqrt{\left(k_{xy}^i\right)^2 + \left(k_{xy}^f\right)^2 - 2k_{xy}^i k_{xy}^f \cos\phi} \quad , \quad (2.21)$$

$$\frac{\left(\hbar k_{xy}^i\right)^2}{2m^*} = E_i - \varepsilon_m \equiv \varepsilon , \quad (2.22)$$

$$\frac{\left(\hbar k_{xy}^f\right)^2}{2m^*} = E_i - \varepsilon_n \mp \hbar\omega_0 = \varepsilon + (\varepsilon_m - \varepsilon_n) \mp \hbar\omega_0 , \quad (2.23)$$

where N_0 is the thermal population of LO phonons at temperature T, k_B the Boltzmann constant, ϕ the angular between $\vec{k}_{xy}^i$ and $\vec{k}_{xy}^f$, and ε is the in-plane kinetic energy of the electron. The term $I_{mn}(Q)$ is defined as [17,58,60]

$$I_{mn}(Q) = \int_{-\infty}^{+\infty} \frac{|G_{mn}(q_z)|^2}{Q^2 + q_z^2} dq_z \quad , \quad (2.24)$$

where

$$G_{mn}(q_z) = \int_0^{L_{eff}} \chi_m^*(\vec{r})\exp(iq_z z)\chi_n(\vec{r})dz \quad (2.25)$$

determines momentum conservation in the z direction; here $z \equiv z + \delta_0$. With the functions given by Eqs.(2.3) and (2.7), the exact formula for $I_{mn}(Q)$ can be given in the form [60]

$$I_{mn}(Q) = \frac{\pi}{Q}\iint \varphi_m(z)\varphi_n(z)\exp(-Q|z-z'|)\varphi_m(z')\varphi_n(z')dz\,dz' . \quad (2.26)$$

For a system operated at temperature $T = 0$ K the thermal population of phonons is equal to zero; *i.e.* $N_0 = 0$. In other words, only a spontaneous LO phonon emission exists. As a result, Eq. (2.18) reduces to

$$\frac{1}{\tau_i} = C_0 \iint I_{mn}(Q)\delta\left(E_i - E_f - \hbar\omega_0\right)d^2k_{xy}^f \quad . \tag{2.27}$$

By substituting $d^2k_{xy}^f = k_{xy}^f d\phi\, dk_{xy}^f = \frac{m^*}{\hbar^2} d\phi\, dE'$; here $E' = E_f + \hbar\omega_0$, the scattering rates become

$$\frac{1}{\tau_i} = C_0\left(\frac{m^*}{\hbar^2}\right) \int_0^{2\pi} I_{mn}(Q)d\phi \int_{E'} \delta(E_i - E')dE' \ , \tag{2.28}$$

and it is finally obtained,

$$\frac{1}{\tau_i} = C_0\left(\frac{m^*}{\hbar^2}\right) \int_0^{2\pi} I_{mn}(Q)d\phi \ . \tag{2.29}$$

To obtain the useful analytical expressions for the intra- and intersubband scattering rates, the considerations will be divided as follows:

(i) The intrasubband scattering rates ($m = n$)

The intrasubband scattering processes will be achieved if the in-plane kinetic energy of the electron is just enough to emit an LO phonon; i.e. $\varepsilon \geq \hbar\omega_0$. The integral $I_{mn}(Q)$ given by Eq.(2.26) can be obtained for two extreme conditions as follow [60]:

$$I_{nn}(Q) \cong \begin{cases} \dfrac{\pi}{Q} & ; \text{ for } Q \ \langle\langle \ q_z \\ \dfrac{\pi}{b_{nn}Q^2} & ; \text{ for } Q \ \rangle\rangle \ q_z \end{cases} , \tag{2.30}$$

where $\frac{1}{b_{nn}} \equiv 2 \int_0^{L_{eff}} \varphi_n^2(z)\varphi_n^2(z)dz = \frac{3}{L_{eff}}$. From the both resulting approximations given in Eq.(2.30) the formula for $I_{nn}(Q)$ can be approximately written in the form

$$I_{nn}(Q) \cong \frac{\pi}{Q(1 + b_{nn}Q)} \quad ; \text{ For all values of } Q \tag{2.31}$$

By substituting $I_{nn}(Q)$ given in Eq.(2.31) into Eq.(2.29), and using Eqs.(2.21)-(2.23), the intrasubband scattering rates is finally obtained

$$\frac{1}{\tau_{n\to n}(\beta)} = C_0\left(\frac{m^*}{\hbar^2}\right)\int_0^{2\pi}\frac{\pi}{Q_{\beta nn}\left[1+b_{nn}Q_{\beta nn}\right]}d\phi \ , \tag{2.32}$$

where $\tau_{n\to n}(\beta)\equiv\tau_i$ is the intrasubband scattering times, and $Q_{\beta nn}\equiv Q$.

From Eqs.(2.21)-(2.23), it can be obtained

$$Q_{\beta nn} = \sqrt{\left(\frac{2m^*}{\hbar^2}\right)\hbar\omega_0\beta}\cdot\left[1+\left(1-\frac{1}{\beta}\right)-2\sqrt{1-\frac{1}{\beta}}\cos\phi\right]^{1/2} , \tag{2.33}$$

where $\beta=\dfrac{\varepsilon}{\hbar\omega_0}$ is a dimensionless in-plane kinetic energy of the electron in units of LO-phonon energy $\hbar\omega_0$.

(ii) The intersubband scattering rates ($m\neq n$; here only $m>n$ is considered)

According to the analogous method above the results of Eq.(2.26) are [60]

$$I_{mn}(Q) \cong \begin{cases}\dfrac{2L}{\pi}\left[\dfrac{m^2+n^2}{\left(m^2-n^2\right)^2}\right] & ;\ \text{for}\ Q \ll q_z \\ \dfrac{\pi}{b_{mn}Q^2} & ;\ \text{for}\ Q \gg q_z\end{cases} , \tag{2.34}$$

where $\dfrac{1}{b_{mn}}\equiv 2\int_0^{L_{eff}}\varphi_m^2(z)\varphi_n^2(z)dz=\dfrac{2}{L_{eff}}$. From the results given in Eq.(2.34), the formula for $I_{mn}(Q)$ can be approximately written in the form

$$I_{mn}(Q) \cong \frac{\pi}{A_{mn}+b_{mn}Q^2} \quad ; \quad \text{For all values of } Q \tag{2.35}$$

where $A_{mn}=\dfrac{\pi^2\left(m^2-n^2\right)^2}{2L\left(m^2+n^2\right)}$. By substituting $I_{mn}(Q)$ given in Eq.(2.35) into Eq.(2.29), the intersubband scattering rates is obtained

$$\frac{1}{\tau_{m\to n}(\beta)} = C_0\left(\frac{m^*}{\hbar^2}\right)\int_0^{2\pi}\frac{\pi}{A_{mn}+\ b_{mn}Q_{\beta mn}^2}d\phi\ , \tag{2.36}$$

here $\tau_{m\to n}(\beta)\equiv\tau_i$ is the intersubband scattering time, and $Q_{\beta mn}\equiv Q$. Again, by using Eqs.(2.21)-(2.23)

$$Q_{\beta mn} = \sqrt{\left(\frac{2m^*}{\hbar^2}\right)\hbar\omega_0\beta}\cdot\left[1+\left(1+\frac{(\gamma-1)}{\beta}\right)-2\sqrt{1+\frac{(\gamma-1)}{\beta}}\cos\phi\right]^{1/2}, \tag{2.37}$$

where $\gamma\equiv\dfrac{\varepsilon_m-\ \varepsilon_n}{\hbar\omega_0} = \left(\dfrac{\pi^2\hbar^2}{2m^*}\right)\left(\dfrac{1}{\hbar\omega_0}\right)\left(\dfrac{m^2-\ n^2}{L_{eff}^2}\right)$.

2.3 Results and discussion

In this section semi-analytic calculations for electron LO-phonon scattering rates (or times) in a $GaAs/Al_{0.3}Ga_{0.7}As$ SQW structure are presented. Unless otherwise speci-fied, the following calculations have been performed with the material parameters: $\kappa_0=12.90$, $\kappa_\infty=10.92$, and $\hbar\omega_0=36\,\text{meV}$ [60]. According to Eqs.(2.32) and (2.36) the scattering rates (or times) can be plotted as a function of in-plane kinetic energy of the electron (Figure 2.4). To compare our calculations with the results reported by Ferreira and Bastard [12] the well-width dependence of these scattering rates (or times) are also investigated (Figure 2.5).

Figure 2.4 presents the resulting calculations of the in-plane kinetic dependence of the intra- (1→1) and intersubband (2→1) scattering rates (or times) for different well widths: L = 60, 80 and 100 Å at temperature T = 0 K. The results shows that both intra- and intersubband scattering rates (or times) weakly depend on in-plane kinetic energy of the electron. For the intrasubband scattering the rates are always zero at $\beta<1$. The reason for this is that electrons have no chance to emit LO phonons in this energy region

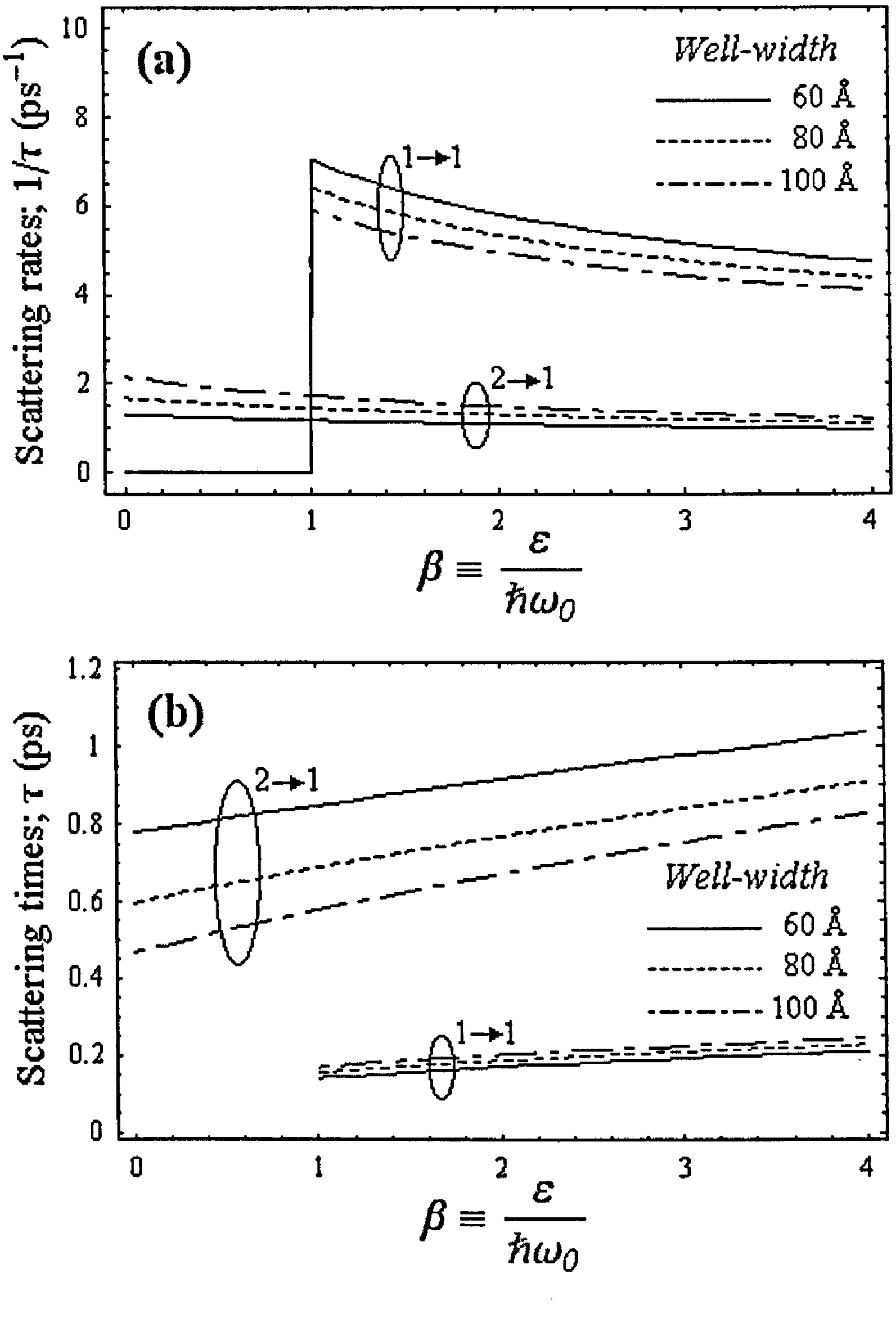

Figure 2.4 **(a)** In-plane kinetic dependence of the intra- (1→1) and intersubband (2→1) scattering rates due to an LO-phonon emission in GaAs/$Al_{0.3}Ga_{0.7}As$ SQW structures of well widths 60, 80 and 100 Å at temperature T = 0 K, and **(b)** the corresponding intra- and intersubband scattering times.

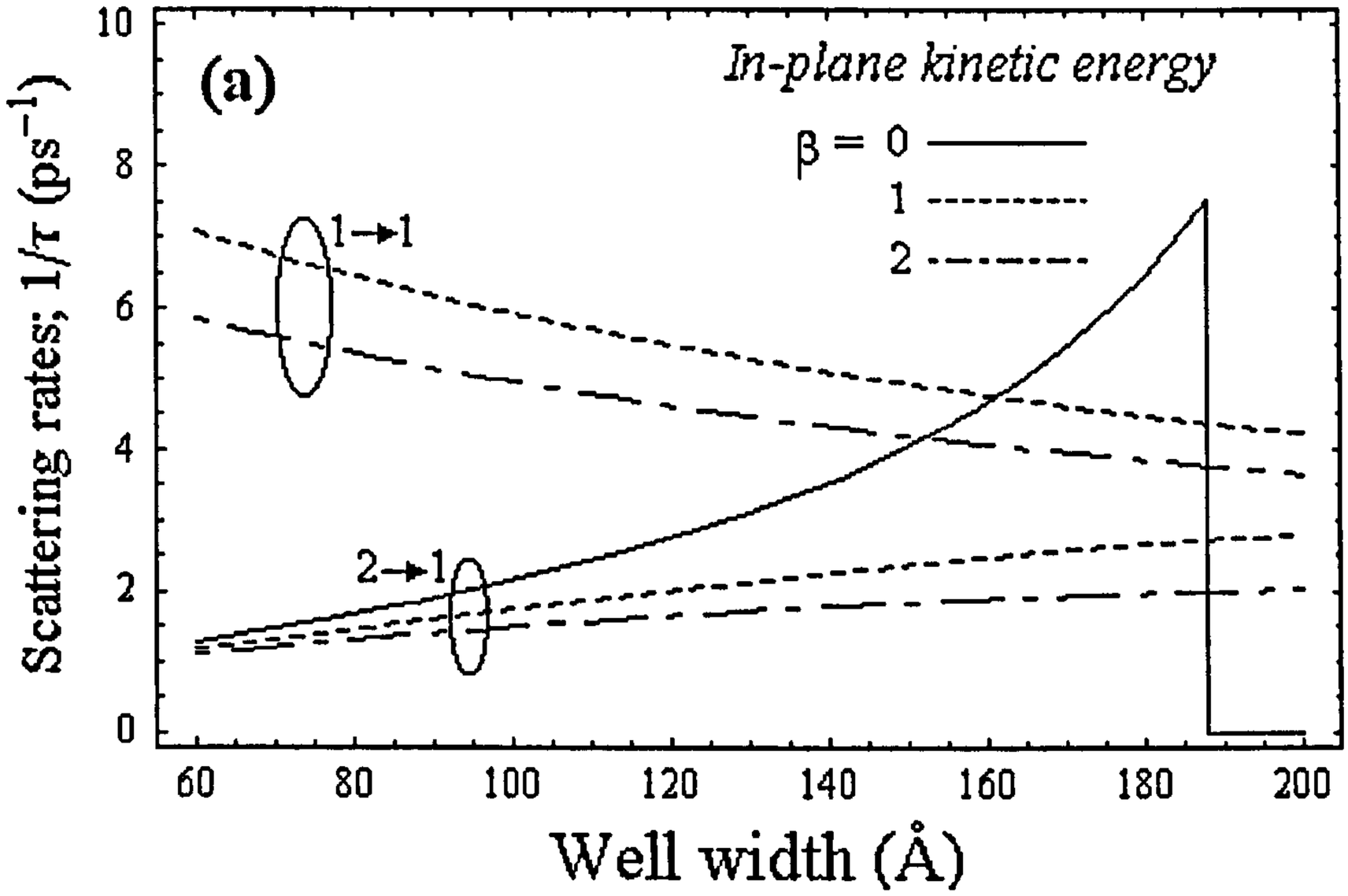

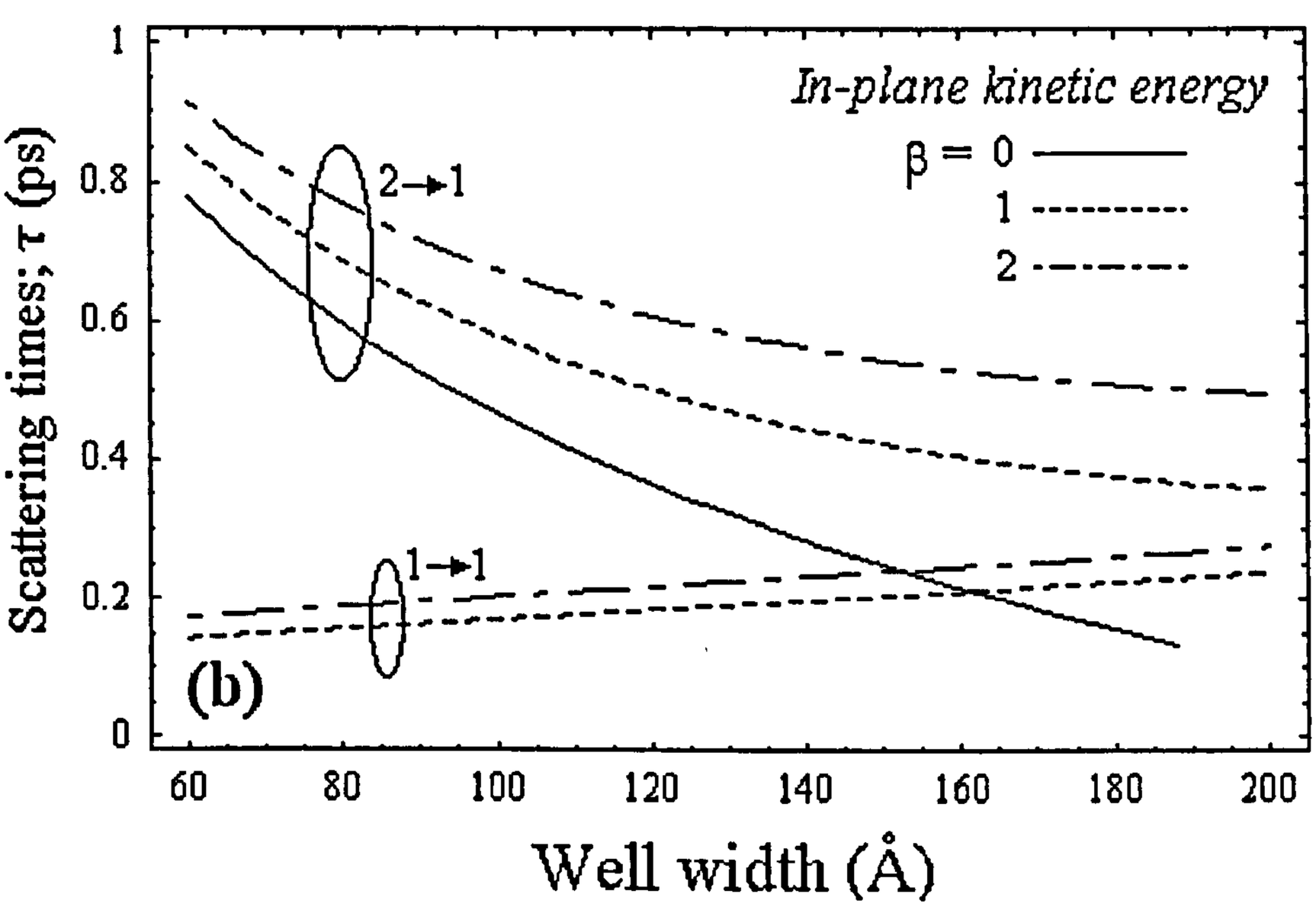

Figure 2.5 **(a)** Well width dependence of the intra- (1→1) and intersubband (2→1) scattering rates due to an LO-phonon emission in GaAs/$Al_{0.3}Ga_{0.7}As$ SQW structures for different in-plane kinetic energies; β = 0, 1 and 2, at temperature T = 0 K, and **(b)** the corresponding intra- and intersubband scattering times.

In Figure 2.5 the plots are obtained for the well width dependence of intra- (1→1) and intersubband (2→1) scattering rates (or times) at temperature T = 0 K. For a narrow QW with the well width $L < 100$ Å resulting in large values of the energy separation between the two subbands invloved, $E_2 - E_1 > 3\hbar\omega_0$, these scattering rates (or times) are not strongly dependent upon well width (see also Figure 2.4). For the intrasubband scattering (1→1) the resulting calculations show that the scattering times are almost independent on the well width.

For the intersubband scattering (2→1); especially for the cases of electron initial states with small in-plane kinetic energies ($\beta \to 0$), the rates monotonically increase with well width. When the quantum well becomes wider which results small values of the subband energy separation $E_2 - E_1$ the rates strongly increase with well width, and have a peak at the point at which $E_2 - E_1 = \hbar\omega_0$. For fairly wide QWs ($L > 180$ Å) that have $E_2 - E_1 < \hbar\omega_0$ the intersubband scattering due to LO phonon emission is impossible. Furthermore, it is clearly seen that the intersubband scattering (2→1) times are always longer than the intrasubband scattering (1→1) times for all cases of $\beta \geq 1$. It is also found that the inter- and intrasubband scattering times differ by less than a factor of 3 for $L > 100$ Å, but nearly an order of magnitude in narrow QWs.

Figure 2.6 compares the semi-analytic calculations of the scattering times, based on our approach, as a function of well width to the numerical results calculated by Ferreira and Bastard [12]. It can be seen that the semi-analytic results, especially for the intrasubband scattering, have a quite good agreement with the results reported in Ref. 12. This provides a strong support for the application of our simplistic methodolo-gy to other similar systems. Furthermore, the results also show that the intrasubband scattering time due to LO-phonon scattering is approximately on the order of 0.1 – 0.2 ps, while the intersubband scattering time exceeds to the order of 1 – 2 ps, depending upon the well width. It is, however, our approach having an advantage of that the analytic expressions given in Eqs.(2.32) and (2.36), respectively, for the intra- and intersubband scattering rates (or times) are quite simple and practical to generalize to other similar QW systems.

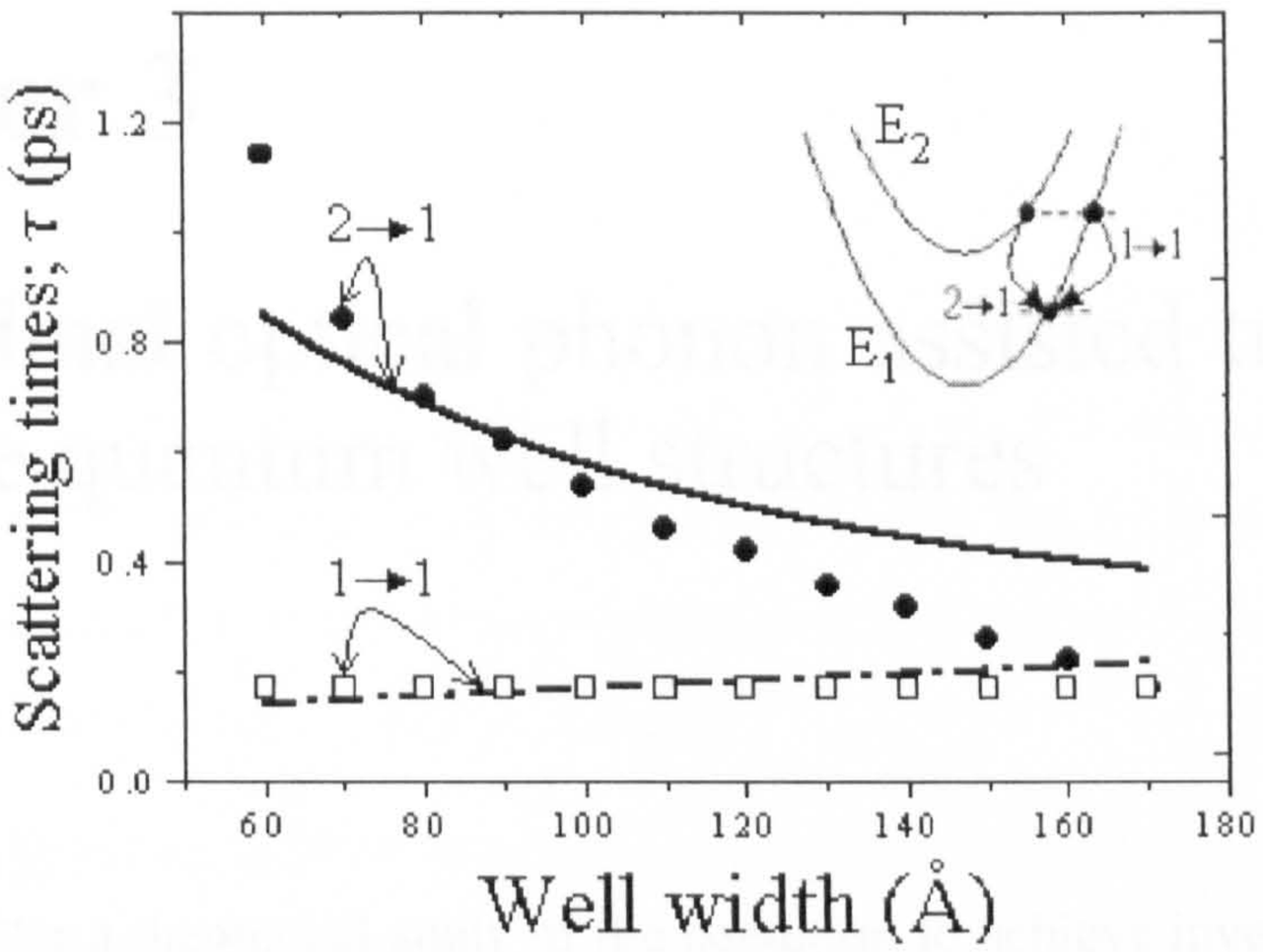

Figure 2.6 Comparison of the well width dependence of the intra- (1→1) and intersubband (2→1) scattering times, due to an LO-phonon emission in GaAs/$Al_{0.3}Ga_{0.7}As$ SQW structures at temperature $T = 0\,\mathrm{K}$, as calculated by our semi-analytic approach and by the numerical method described in Ref. 12. The lines, solid (——) and dash-dot (—·—·), are the semi-analytic results based on our methodology. The symbols (● and □) are numerical results of the scattering times extracted from a typical calculated result in Ref. 12.

2.4 Conclusions

In summary, starting from the Fröhlich interaction and Fermi's golden rule, the expressions for the intra- and intersubband scatering rates (or times) have been obtained. Semi-analytic calculations are carried out for a GaAs/$Al_{0.3}Ga_{0.7}As$ SQW structure. The results mainly show that the scattering rates, both for the intra- and intersubband scattering, weakly depend on in-plane kinetic energy of the electron. For the intrasubband scattering the rates gradually decrease at $\beta \geq 1$. If $\beta < 1$, electrons have no chance to emit LO phonons resulting that the rates are always zero in this region.

The investigation of the well width dependence of the intra- and intersubband scattering shows that the intrasubband scattering times gradually increase with well width while the intersubband scattering times monotonically decrease. For the QW structures with narrow well widths ($L < 100\,\text{Å}$) it is found that the intrasubband scattering times are always much shorter than that for intersubband scattering. These rates are close to each other for wider QWs.

Chapter 3

Longitudinal optical phonon assisted tunneling in double quantum well structures

In this chapter a theoretical study of the condition to achieve inverted population in a semiconductor DQW structure is presented. The aim is to calculate the tunneling rates for interwell transitions due to electron LO-phonon scattering in a DQW structure as shown schematically in Figure 3.1. This structure is similar to that used as an inter-subband lasing unit in QCL structures. It consists of a wider well (QW1) as a lasing unit, and a narrower well (QW2) as an electronic energy filter by various type of tunneling mechanisms. The tunneling rates are mainly investigated as a function of the difference in energy between the E_1 level of the QW1 and the E_1^* level of the QW2 (see Figure 3.1).

3.1 Introduction

Recently, it has been demonstrated that in order to achieve inverted population in a triple barrier resonant tunneling structure (TBRTS) one should ensure efficient re-moval of carriers from the E_1^* level [15,62,63]. Transport through the TBRTS has also been extensively theoretically [64-66] and experimentally [67-69] studied. The physics of resonant tunneling in these systems is much more than an extension of the results of the double-barrier case [1,2,70-77] since the former involves the coupling of quasi-bound states between two adjacent wells in the DQW structure. In most cases the experimental resonant position corresponds to theoretical prediction based on a 1D self-consistent solution of Poisson's and Schrödinger equations. However, the ampli-tude and width of the LO-phonon peak differ significantly from the 1D-model [68].

This discrepancy arises from scattering processes which accompany tunneling processes and result in sequential, rather than coherent, tunneling. This was clearly demonstrated in experiment with application of strong magnetic field parallel to the current [67-69]. These papers experimentally prove the essential role of LO phonons for sequential tunneling. Theoretically, the role of LO-phonon assisted tunneling in resonant tunneling was also extensively studied [67,70-75]. The main result for TBRTS shows that the resonant peak in the current-voltage characteristics became wider and a satellite peak appears at an LO-phonon energy.

Another LO-phonon assisted tunneling problem comes from the studies of a vertical transport in superlattices [78,79]. It was found that LO-phonon scattering is the most efficient process for hopping conductivity [80]. It has also been shown by Tsu and Döhler [78] that superlattice transport can be reduced to a DQW problem. The transfer integral for the DQW system was calculated by Calecki *et al* [79]. However, the calculation did not take into account that initial and final states should be orthogonal, and their result takes only the exponentially small overlap of wavefunctions in the barrier. This problem has be resolved numerically by Weil and Vinter [80], and their result shows that the main overlap comes from well regions, but not from the interbarrier overlap. This approach has been generalized by Ferreira and Bastard [12], and Harrison [81]. These calculations take into account the slope of conduction band in the heterostructure affected by applied electric field, and also consider other various mechanisms for interwell scattering such as the electron-electron (e-e) and electron-acoustic-phonon scattering. However, in both papers [12,81] the 1D-Schrödinger equation was treated numerically without taking into account the different effective masses of electrons in the wells and barriers. The exact analytic solution of the 1D-Schrödinger equation taking into account the different effective masses has been obtained by Allen and Richardson [64]. However, the results are not practical to calculate the matrix elements for the LO-phonon transitions.

3.2 Formalism of LO-phonon assisted tunneling in double quantum well structures

3.2.1 Electronic states in a DQW structure

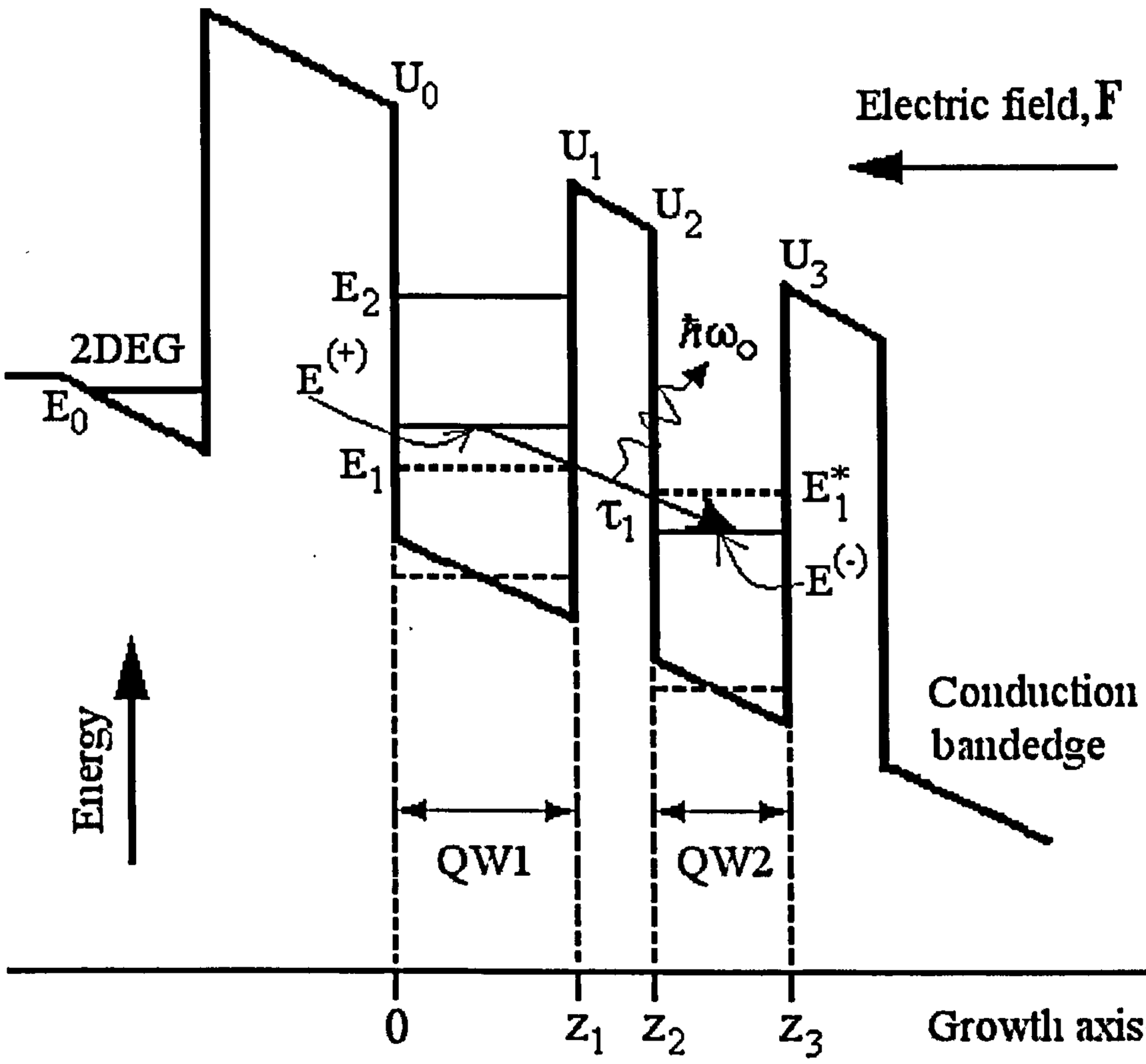

Figure 3.1 Schematic conduction bandedge profile of a DQW structure with a wider well (QW1) as a lasing unit and a narrower well (QW2) as an electronic energy filter by various types of tunneling mechanisms.

A GaAs/$Al_xGa_{1-x}As$ DQW structure is schematically shown in Figure 3.1. This has been used as an intersubband lasing structure, consisting of a wider well (QW1) as a lasing unit and a narrower well (QW2) as an electronic energy filter by various type of tunneling mechanisms. To create lasing efficiency, in general, it is necessary to achieve a sufficient population inversion between subbands E_2 and E_1 in the QW1. Population inversion occurs when the device has appropriate design parameters providing a good electron confinement at the upper subband E_2 and short electron lifetime at the lower subband E_1.

In this chapter the tunneling rates of electron from the subband E_1 are investigated. The investigation mainly focuses on a variation of the electron tunneling rates, $\frac{1}{\tau_1}$, as a function of the energy difference $E_1 - E_1^*$; where τ_1 is the tunneling time of the electron from subband E_1. The notations E_1, E_2 and E_1^* stand for the electron states in each of the wells when isolated from each other (see Figure 3.1).

However, in reality, one has to consider the system where two potential wells are connected via a barrier that permits a measure of quantum mechanical tunneling. For reasons of simplification, the DQW structure shown in Figure 3.1 can be simplified by neglecting the effect of linear potential drop in the wells, and consider it as a rectangular QW with finite-wall problem. To make the results more realistic it is useful to take into account finite barrier heights in first approximation (as employed in Chapter 2) that give for effective well widths of QW1, QW2 and barrier thickness in terms of a_c, d_c and b_c, respectively [39,42,46-53] :

$$a_c = L_1 + \delta_0 + \delta_1, \qquad d_c = L_2 + \delta_2 + \delta_3, \qquad b_c = b - \delta_1 - \delta_2 , \tag{3.1}$$

and

$$\delta_i = \frac{\hbar}{\sqrt{2\left(\frac{m_w^*}{m_b^*}\right)m_w^* U_i}} \quad ; \; i = 0,1,2,3 \tag{3.2}$$

where L_1 and L_2 are the well widths of QW1 and QW2, respectively. b refers to the middle barrier thickness, m_w^* and m_b^* stand for effective masses of the electron in the QWs, and in the barriers, respectively. U_i are the heights of the barriers adjusted to the QWs that takes into account applied electric field $\vec{F}$, given as

$$\left.\begin{aligned} U_0 &= \Delta E_C + eF\left(\frac{L_1}{2}\right), & U_1 &= \Delta E_C - eF\left(\frac{L_1 + b}{2}\right) \\ U_2 &= \Delta E_C + eF\left(\frac{L_2 + b}{2}\right), & U_3 &= \Delta E_C - eF\left(\frac{L_2}{2}\right) \end{aligned}\right\} \tag{3.3}$$

where ΔE_C is the conduction band-offset of the GaAs/$Al_xGa_{1-x}As$ heterostructure, F is the magnitude of the applied electric field, and e is the electronic charge. In general, this approach works well if the barrier is high enough; *i.e.* $\frac{\pi^2\hbar^2}{2m_w^* d_c^2} << \Delta E_C$.

According to the approach above, and neglecting the exponentially small tails of the wavefunctions as they give a small contribution to the LO-phonon matrix element, the ground state wavefunctions in each of the wells when isolated from each other can be given by

$$\varphi_1(z) = \begin{cases} 0 & ; \ z < -\delta_0 \\ \sqrt{\frac{2}{a_c}}\sin\left[\frac{\pi}{a_c}(z+\delta_0)\right] & ;-\delta_0 < z < z_1+\delta_1 \\ 0 & ; \ z > z_1+\delta_1 \end{cases} \tag{3.4}$$

$$\varphi_2(z) = \begin{cases} 0 & ; z < z_2-\delta_2 \\ \sqrt{\frac{2}{d_c}}\sin\left[\frac{\pi}{d_c}(z_3+\delta_3-z)\right] & ; z_2-\delta_2 < z < z_3+\delta_3 \\ 0 & ; z > z_3+\delta_3 \end{cases} \tag{3.5}$$

where φ_1 and φ_2 stand for the unperturbed states E_1 and E_1^*, respectively. Because wells are coupled, one can assume that the eigenfunction of the system is a linear combination of φ_1 and φ_2 [82-86]. Thus,

$$\varphi(z) = a_1\varphi_1(z) + a_2\varphi_2(z), \tag{3.6}$$

In this approach the values of a_1 and a_2 are determined from the eigenvalue equation

$$\begin{pmatrix} E_1 & M_{12} \\ M_{21} & E_1^* + i\Gamma \end{pmatrix}\begin{pmatrix} a_1 \\ a_2 \end{pmatrix} = E'\begin{pmatrix} a_1 \\ a_2 \end{pmatrix}, \tag{3.7}$$

where E' is the energy eigenvalue of the electron when wells are coupled. M_{12} is the transfer integral between the states E_1 and E_1^*; in this work it is assumed that $M_{12} = M_{21} = -M$, and Γ is half width of the E_1^* level. According to the approach introduced by Bar-Joseph and Gurvitz [86] the latter M can be given as

$$M = \frac{\hbar^2\kappa}{m_w^*\left(\frac{m_w^*}{m_b^*}\right)}\left(\frac{2}{\sqrt{L_1L_2}}\right)\left(\frac{E_1E_1^*}{U_1U_2}\right)^{1/2}\exp(-\kappa b), \tag{3.8}$$

where

$$\kappa = \frac{1}{2}\left[\sqrt{\frac{2m_w^*\left(\frac{m_w^*}{m_b^*}\right)}{\hbar^2}(U_1-E_1)} + \sqrt{\frac{2m_w^*\left(\frac{m_w^*}{m_b^*}\right)}{\hbar^2}(U_2-E_1^*)}\right]. \tag{3.9}$$

The resulting calculations for the DQW structure with well widths and barrier thickness: $L_1 = 66$ Å, $L_2 = 33$ Å and $b = 26$ Å, give the approximate values of M around 5.0 meV depending on the magnitude of electric field. However, experimental data reported by Li *et al* [15] gives M as about 7.5 meV for such the DQW structure.

Furthermore the perturbed energy eigenvalues satisfied Eq.(3.7) are determined by the secular equation,

$$\det\begin{pmatrix} E'-E_1 & M \\ M & E'-E_1^*-i\Gamma \end{pmatrix} = 0, \tag{3.10}$$

and it is finally obtained that

$$E^{(\pm)} = \left(\frac{E_1+E_1^*-i\Gamma}{2}\right) \pm \sqrt{\left(\frac{E_1-E_1^*+i\Gamma}{2}\right)^2 + M^2}\ . \tag{3.11}$$

The actual energy splitting clearly depends on the magnitude of the transfer integral M, and the half width Γ of the E_1^* level. With the introduction of $\varepsilon = \frac{E_1-E_1^*}{2}$ and $\omega = \sqrt{\varepsilon^2+\left(M^2-\frac{1}{4}\Gamma^2\right)}$ the normalized eigen wavefunctions are

$$\varphi^{(\pm)}(z) = C_1^{(\pm)}\varphi_1(z) + C_2^{(\pm)}\varphi_2(z), \tag{3.12}$$

where $C_1^{(\pm)} = \dfrac{\mp\sqrt{M^2 - \frac{1}{4}\Gamma^2}}{\sqrt{(\omega \mp \varepsilon)^2 + \left(M^2 - \frac{1}{4}\Gamma^2\right)}}$, and $C_2^{(\pm)} = \dfrac{\omega \mp \varepsilon}{\sqrt{(\omega \mp \varepsilon)^2 + \left(M^2 - \frac{1}{4}\Gamma^2\right)}}$.

3.2.2 The LO-phonon assisted tunneling in a DQW structure

According to Fermi's golden rule, the scattering rates of an electron from an initial state $\left|m, k_{xy}^i\right\rangle$ in the mth subband to all final states $\left|n, k_{xy}^f\right\rangle$ in the nth subband accompanied by emission (or absorption) of a phonon with energy $\hbar\omega$ is [12,58,59]

$$\frac{1}{\tau_i} = \frac{2\pi}{\hbar}\int \left|\left\langle n, k_{xy}^f \left| \hat{H}_{e-ph} \right| m, k_{xy}^i \right\rangle\right|^2 \delta\left(E_i - E_f \mp \hbar\omega\right) dN_f \qquad (3.13)$$

where the upper (lower) sign refers to emission (absorption) of the phonon. E_i and E_f are the total energies of the electron at initial and final states, respectively. In this expression the integration is done over the final density of states N_f. For the LO-phonon scattering mode the rate is therefore [12,60]

$$\frac{1}{\tau_i} = C_0 \iint I_{mn}(Q)\left[(N_0+1)\delta\left(E_i - E_f - \hbar\omega_0\right) + N_0\delta\left(E_i - E_f + \hbar\omega_0\right)\right] d^2k_{xy}^f , \qquad (3.14)$$

associated with the appropriate variables as given in Eqs.(2.19)-(2.23). The integral $I_{mn}(Q)$ can be obtained from Eq.(2.26), and it is simplified by considering the results only for an extreme condition of small Q values; *i.e.* $Q << q_z$.

By substituting wavefunctions given by Eq. (3.12) into Eq. (2.26)

$$I_{mn}(Q) \cong \frac{\pi}{Q}\left\{\frac{\left(C_1^{(+)}C_1^{(-)}\right)^2}{1+0.207Qa_c} + \frac{\left(C_2^{(+)}C_2^{(-)}\right)^2}{1+0.207Qd_c} + \frac{2C_1^{(+)}C_1^{(-)}C_2^{(+)}C_2^{(-)}}{1+Q\left(\frac{a_c}{2}+b_c+\frac{d_c}{2}\right)}\right\}, \qquad (3.15)$$

and the magnitude of the in-plane phonon wave vector Q given in Eq. (2.21) can be written as

$$Q = \sqrt{\left(\frac{2m_w^*}{\hbar^2}\right)\hbar\omega_0\,\beta}\cdot\left[1+\left(1+\frac{(\gamma-1)}{\beta}\right)-2\sqrt{1+\frac{(\gamma-1)}{\beta}}\cos\phi\right]^{1/2}, \tag{3.16}$$

where ϕ is the angle between $\vec{k}_{xy}^{\,i}$ and $\vec{k}_{xy}^{\,f}$. The dimensionless energy parameters β and γ are defined as follows:

$$\beta = \frac{\varepsilon}{\hbar\omega_0} = \frac{\hbar^2\left(k_{xy}^i\right)^2}{2m_w^*\hbar\omega_0}, \tag{3.17}$$

$$\gamma = \frac{E^{(+)}-E^{(-)}}{\hbar\omega_0} = \frac{\sqrt{\left(E_1-E_1^*\right)^2+\left(4M^2-\Gamma^2\right)}}{\hbar\omega_0}. \tag{3.18}$$

The expression for the LO-phonon assisted tunneling rates given in Eq.(3.14) associated with Eqs.(3.15)-(3.18), in general, can be applied to any LO-phonon scattering processes from the mth subband to the nth subband. It clearly shows that the rate $\frac{1}{\tau_i}$ depends on both β and γ.

3.3 Results and discussion

Semi-analytic calculations of the LO-phonon assisted tunneling rates have been performed for a GaAs/$Al_{0.3}Ga_{0.7}$As DQW structure with relevant characteristic parameters: $L_1 = 66$ Å, $b = 26$ Å, and $L_2 = 33$ Å. In Figure 3.2 the tunneling rates at temperature $T = 0\,\mathrm{K}$ for different values of M: 5.0 meV and 7.5 meV are investigated as a function of the energy difference $E_1 - E_1^*$. In these plots the resulting calculations of the LO-phonon assisted tunneling rates (solid line) are mainly to compare with the coherent tunneling rates (dash-dot line)

$$\left.\frac{1}{\tau_1}\right|_{coherent} = -\frac{1}{\hbar}\mathrm{Im}\,E^{(+)} \cong \frac{\Gamma}{2\hbar}\left(1-\frac{1}{\sqrt{1+\dfrac{4M^2-\Gamma^2}{\left(E_1-E_1^*\right)^2}}}\right), \tag{3.19}$$

(see for details in Chapter 5).

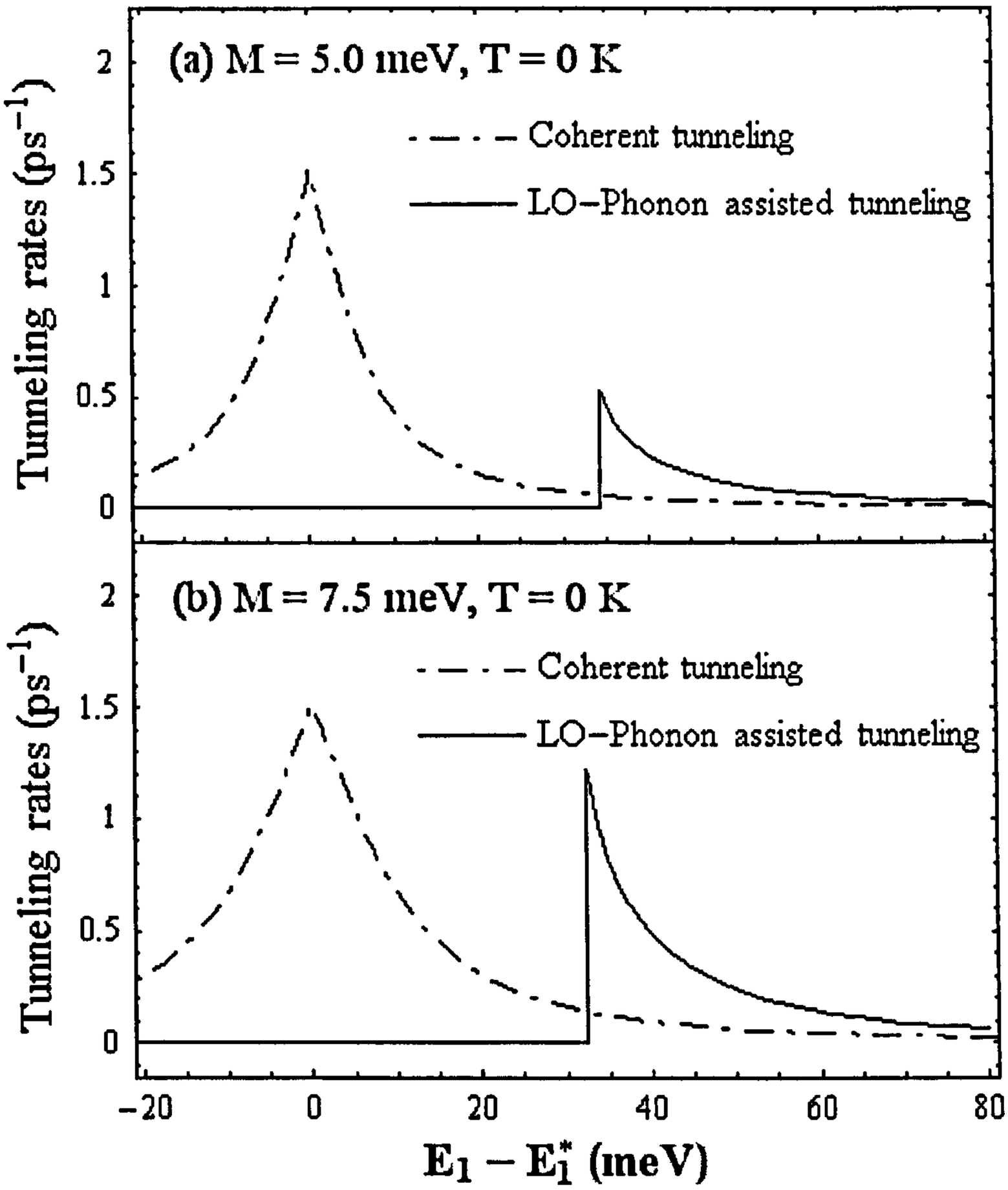

Figure 3.2 Electron tunneling rates as a function of the energy difference $E_1 - E_1^*$ at operating temperature $T = 0\,\mathrm{K}$ for different values of the transfer integral M : **(a)** 5.0 meV, and **(b)** 7.5 meV.

Figure 3.2(a) shows that for $M = 5.0\,\mathrm{meV}$ the tunneling rate due to electron-LO-phonon scattering is much less than the rates due to coherent tunneling. However, these rates of LO-phonon assisted tunneling and coherent tunneling become comparable to each other when the magnitude of the transfer integral M increases; see Figure 3.2(b). In general, the results show that it is possible to get effective LO-phonon assisted tunneling even though the rates are slightly less than that from coherent tunneling. However, the LO-phonon assisted tunneling has an advantage of a wider energy range and is less sensitive to nonparabolicity effects than coherent tunneling.

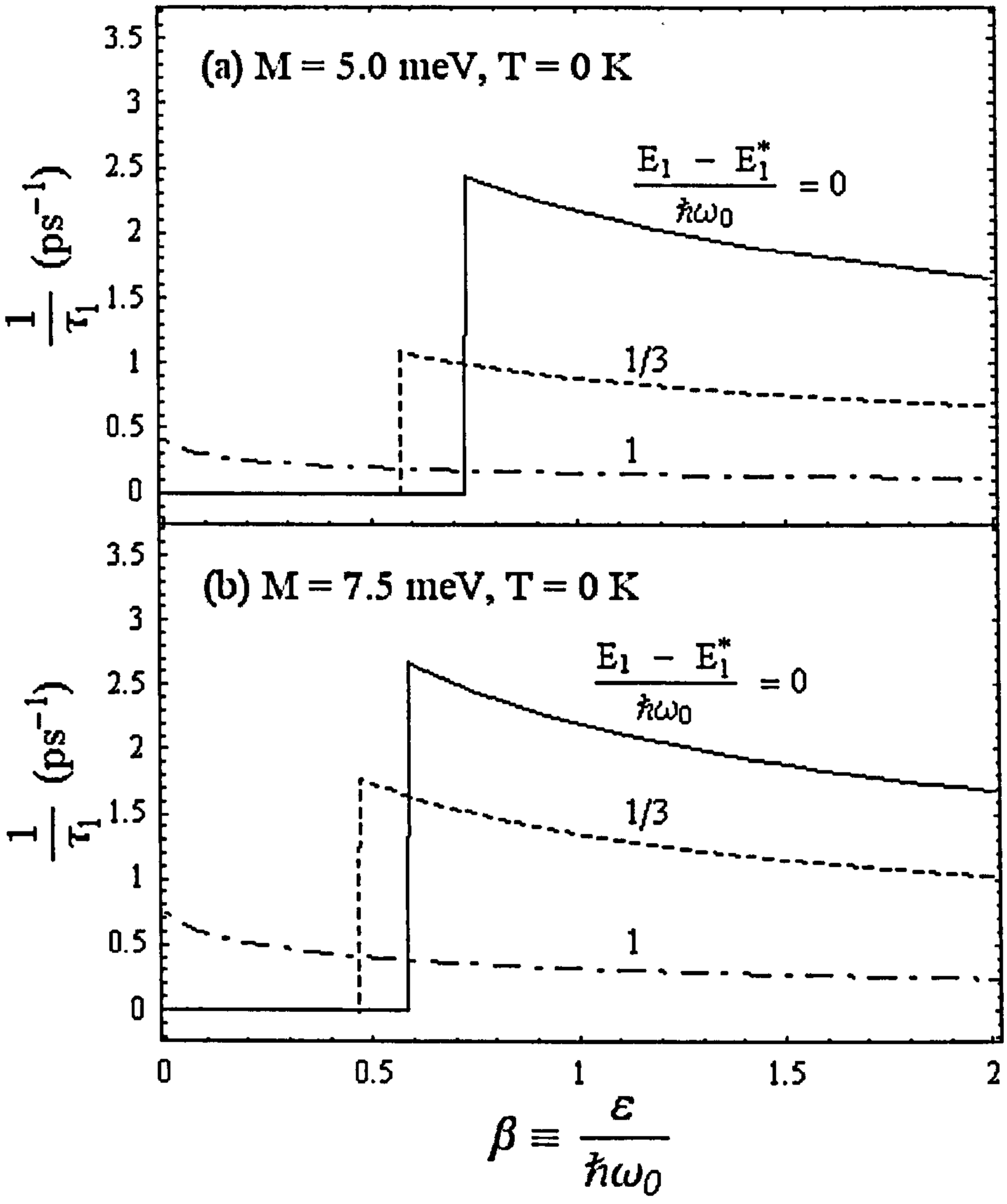

Figure 3.3 In-plane kinetic energy dependence of the LO-phonon assisted tunneling rates at operating temperature $T = 0$ K for different values of the transfer integral M : **(a)** 5.0 meV, and **(b)** 7.5 meV.

In addition, our formula can be used for roughly investigating the tunneling rates for hot electrons, i.e. $\beta \neq 0$. According to Eq.(3.16) one can easily find that the in-plane momentum transfer gradually increases with β. As a result, the integral $I_{mn}(Q)$ is slightly decreased that results in decreasing of the LO-phonon assisted tunneling rates at a particular value of the energy difference $E_1 - E_1^*$.

Figure 3.3 presents the in-plane kinetic energy dependence of LO-phonon assisted tunneling rates for different values of the dimensionless energy difference $\frac{E_1 - E_1^*}{\hbar\omega_0}$: 0,

$\frac{1}{3}$ and 1; assuming the transfer integral M : 5.0meV and 7.5meV. The calculated results mainly show that the tunneling rates due to LO-phonon scattering are weakly dependent upon the in-plane kinetic energy.

3.4 Conclusions

Starting from the Fröhlich interaction and Fermi's golden rule as described in Chapter 2, the tunneling rates due to electron-LO-phonon scattering in a semiconductor GaAs/$Al_xGa_{1-x}As$ DQW structure can be obtained. In general, the resulting calculations mainly show that the tunneling rates monotonically decrease with the energy difference $E_1 - E_1^*$, and strongly depend on the magnitude of the transfer integral M. These rates are calculated at temperature $T = 0$ K. However, the expression given by Eq.(3.14) is quite simple and practical to generalise to other systems considered at temperatures $T > 0$ K.

To calculate the tunneling rates more accurately, it should be mentioned that e-e scattering is also an effective inelastic scattering channel. In our geometry [62,63] the 2DEG in front of the first barrier is likely to have suitable density to ensure effective inelastic scattering. To compare this calculation with experiment it should be mentioned that only indirect measurements are available at the present moment. Furthermore, it has been also found that the average LO-phonon assisted tunneling rates depend strongly on the distribution function of in-plane kinetic energy of electrons [87-89]. As a result, for any particular case one needs to know which part of the distribution function is meaningful for the experiments. However, our results mainly give a simple way to calculate the tunneling rates for various conditions and geometries of the structure.

Chapter 4

Nonequilibrium electrons in double quantum well structures

A theoretical study of hot electrons in a triple-barrier DQW structure (see Figure 4.5) is presented. A system of coupled kinetic equations that describes the nonequilibrium population in each subband has been derived. An analytic solution of the model kinetic equation has been found. Our approach differs from previous treatments [90,91], where the electron distribution functions are based on the two extreme limits: (i) low electron concentration corresponding to $\frac{\tau_0}{\tau_{ee}} << 1$, and (ii) high electron concentration corresponding to $\frac{\tau_0}{\tau_{ee}} \geq 1$; here τ_0 and τ_{ee} refer to electron-LO-phonon (e-LO) scattering and electron-electron (e-e) energy relaxation times, respectively. In the present work, the distribution functions are investigated for the whole range of $\frac{\tau_0}{\tau_{ee}}$ ratios. The outcome of the kinetic equation for subband distribution functions provides a comprehensive description of gain in intersubband lasers.

4.1 Introduction

Studies of mid- and long-wavelength infrared (IR) lasers based on electronic intersubband transitions within the QWs in semiconductor low dimensional heterostructures have attracted a great amount of interest since the first demonstration of a QCL was reported by Faist *et al* [8]. Continued development of QCL operation, improving the threshold current and the maximum temperature of operation, requires a soundly-based understanding of the effects of changing design parameters on the intersubband

population kinetics. For efficient lasing, specially designed structures providing sufficient global population inversion between the two subbands involved are required. In our earlier work [62,63] it has been shown that to achieve inverted population in a $GaAs/Al_xGa_{1-x}As$ DQW structure (shown schematically in Figure 4.5) one should ensure an efficient removal of carriers from the E_1 subband. Population inversion occurs when the device has appropriate design parameters providing a good electron confinement for subband E_2 and short electron lifetime in the E_1 subband.

Recently, it has been shown by Faist *et al.* [92] that for lasing in the intersubband lasers, global population inversion is not a necessary condition but that nonparabolicities combined with the nonthermal electron distribution in the laser unit can make lasing action possible. This idea has been theoretically studied by Gelmont *et al.* [90,91]. The main calculations of these papers were directed to investigate the spectral line shape of radiative intersubband transitions in a QW. It has been found that the line shape of radiative intersubband transitions is determined by two factors:

(i) the electron intra- and intersubband scattering rates, and

(ii) the effective mass differences between the two subbands involved.

The interplay between these two factors leads to essential non-Lorentzian form of the spectral line. Calculations of spectral density of gain $g(\Omega)$ are described as a function of the electron distribution functions $f_1(\varepsilon_1)$ and $f_2(\varepsilon_2)$ in both subbands E_1 and E_2, where ε_1 and ε_2 are the kinetic energies in the subbands E_1 and E_2, respectively. Generally, the distribution functions are nonthermal and their actual shapes strongly affect the spectral density of gain [91]. At very low electron concentrations the distribution function $f_1(\varepsilon_1)$ is given by a quasi-discrete ladder with the occupation probabilities decreasing toward the subband bottom [91,93]. A thermal equilibrium distribution function based on arguments of fast e-e scattering is considered in the majority of these papers [91,93,94]. However, there is substantial gap between the two limiting cases, the very low and high electron concentration regimes of operation. The most typical shape is continuous, but the distribution function is strongly nonequilibrium. This behaviour, in fact, has been studied extensively via the ensemble Monte Carlo

technique (see particularly the work of Goodnick, Lugli and their collaborators) [88,95,96].

Our approach has an advantage of that it is more convenient to build up a model to investigate the kinetics of electron scattering in other similar systems by changing the relevant controlled parameters. However, there are some limitations of this model that will be discussed later in Section 4.5.

4.1.1 Optical Transitions : Optical matrix elements and selection rules for intersubband transitions

The intersubband transition rate for electrons confined in the conduction band of QW structures can be calculated by time dependent perturbation theory, in particular the Fermi golden rule [83, 84]:

$$W = \frac{2\pi}{\hbar}\sum_{i,f}\left|\left\langle f,\vec{k}_{xy}^{f}\left|\hat{H}_{e-photon}\right|i,\vec{k}_{xy}^{i}\right\rangle\right|^{2}\delta\left(E_{f}\left(\vec{k}_{xy}^{f}\right)-E_{i}\left(\vec{k}_{xy}^{i}\right)\mp\hbar\omega\right), \qquad (4.1)$$

where i and f represent initial and final states with total energies E_i and E_f, respectively, the $\mp\hbar\omega$ is for photon to absorption (upper sign) or emission (lower sign), and $\hat{H}_{e-photon}$ is the *electron-photon interaction Hamiltonian*; here $\vec{k}_{xy}=k_x\hat{e}_x+k_y\hat{e}_y$ is the transverse wave vector of the electron. According to the *electric-dipole approximation*, which treats the electric field as constant across the electronic states, *the optical matrix element* has the form [83]

$$M_{fi} = \left\langle f,\vec{k}_{xy}^{f}\left|\hat{H}_{e-photon}\right|i,\vec{k}_{xy}^{i}\right\rangle = \left\langle f,\vec{k}_{xy}^{f}\left|\vec{\xi}\cdot\hat{p}\right|i,\vec{k}_{xy}^{i}\right\rangle, \qquad (4.2)$$

where $\hat{p}=-i\hbar\vec{\nabla}=-i\hbar\left(\hat{e}_x\frac{\partial}{\partial x}+\hat{e}_y\frac{\partial}{\partial y}+\hat{e}_z\frac{\partial}{\partial z}\right)$ is the momentum operator, and $\vec{\xi}$ is the polarization vector of light.

As an example, consider photon absorption (or emission) between bound states in the quantum well aligned along z, shown in Figure 4.1. We have known from Section 2.2 that the electron wave function is factorized into a product of an envelope wave function restricted in the growth direction, $\varphi_i(z)$, and a transverse plane wave as given in Eq.(2.3).

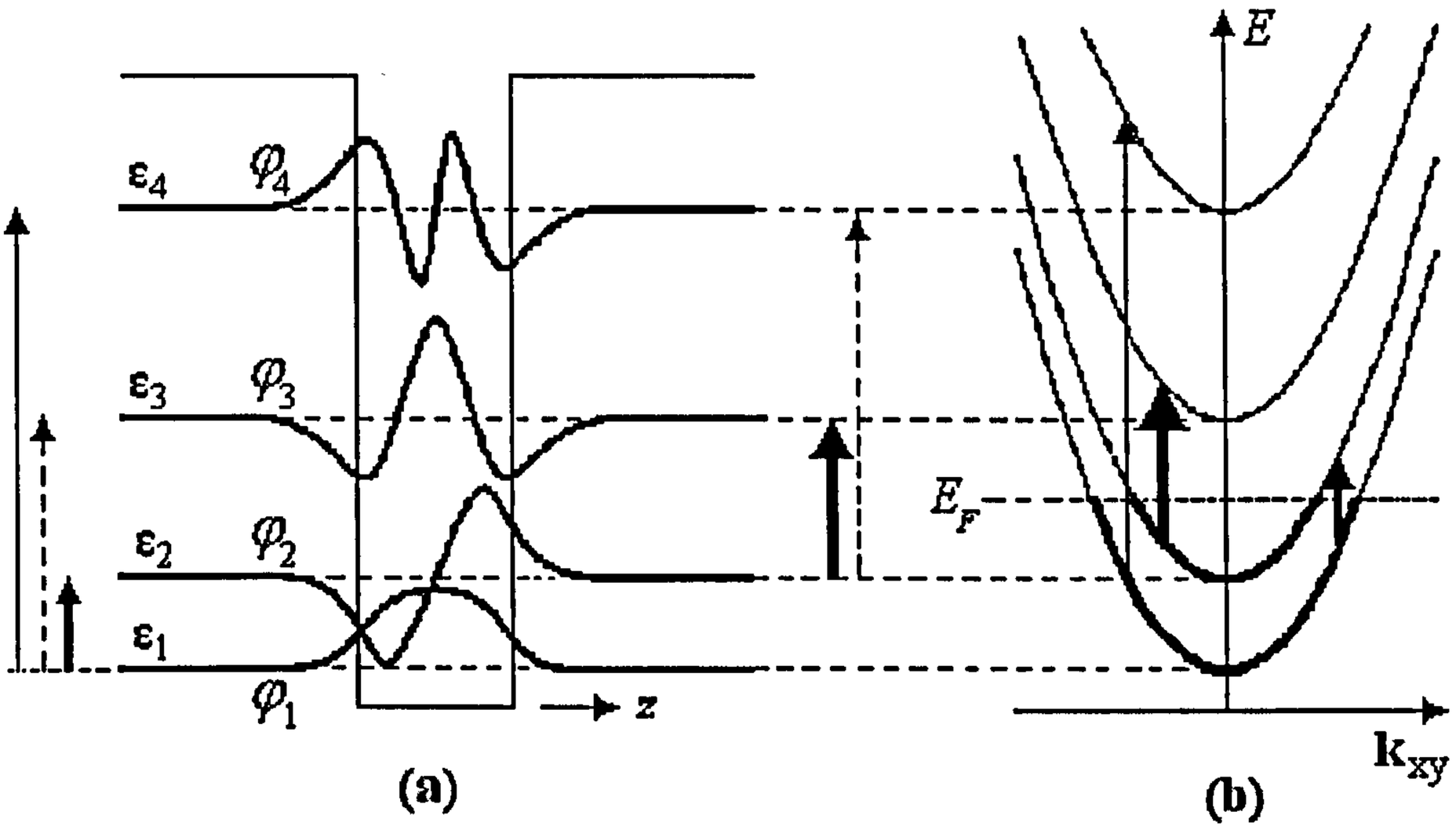

Figure 4.1 Optical absorption by transitions between electronic states in a quantum well. **(a)** Envelope functions along the growth direction with energy levels. The thickness of the arrows are rough indications of the coupling strengths of the transitions, with broken lines indicating forbidden transitions. **(b)** Band structure in the transverse $\vec{k}_{xy}$ plane showing the vertical nature of the allowed transitions, with the Fermi level E_F.

Firstly, suppose that light propagates normal to the QW layers so that the polarization vector of the light is either $\vec{\xi} = \xi \hat{e}_x$ or $\vec{\xi} = \xi \hat{e}_y$, where ξ is for the magnitude of the polarization vector. In the case $\vec{\xi} = \xi \hat{e}_x$, $\vec{\xi} \cdot \hat{p} = -i\hbar\xi \dfrac{\partial}{\partial x}$ which affects only the transverse plane wave of the bound state. Thus,

$$\left(\vec{\xi} \cdot \hat{p}\right)\left|i, \vec{k}_{xy}^{\,i}\right\rangle = \xi \hbar k_x \left|i, \vec{k}_{xy}^{\,i}\right\rangle , \tag{4.3}$$

and

$$M_{fi} = \left\langle f, \vec{k}_{xy}^{\,f}\left|\vec{\xi} \cdot \hat{p}\right|i, \vec{k}_{xy}^{\,i}\right\rangle = \xi \hbar k_x \left\langle f, \vec{k}_{xy}^{\,f}\left|i, \vec{k}_{xy}^{\,i}\right.\right\rangle = 0 . \tag{4.4}$$

Physically, this means that no light is absorbed with this polarization and the same obviously holds for the case $\vec{\xi} = \xi \hat{e}_y$. Thus light propagates normal to the QW layer cannot be absorbed in these transitions.

Now consider the case $\vec{\xi} = \xi \hat{e}_z$, the electric field normal to the QW plane, which requires light to propagate in the plane of the well. In this case, $\vec{\xi} \cdot \hat{p} = -i\hbar\xi \dfrac{\partial}{\partial z}$, which affects only the envelope wave function $\varphi_n(z)$ of the bound state. Thus

$$\left.\begin{aligned} M_{fi} &= \left\langle f, \vec{k}_{xy}^{f} \middle| \vec{\xi} \cdot \hat{p} \middle| i, \vec{k}_{xy}^{i} \right\rangle = \xi \left\langle f, \vec{k}_{xy}^{f} \middle| \hat{p}_z \middle| i, \vec{k}_{xy}^{i} \right\rangle \\ &= \xi \langle f | \hat{p}_z | i \rangle \delta\left(\vec{k}_{xy}^{f} - \vec{k}_{xy}^{i}\right) \end{aligned}\right\}, \tag{4.5}$$

This implies that the optical matrix element $M_{fi} \sim \langle f | \hat{p}_z | i \rangle$ if $\vec{k}_{xy}^{f} = \vec{k}_{xy}^{i}$; *i.e.* the transitions preserve the conservation of the transverse momentum of the electrons, and zero otherwise. Thus, optical transitions are vertical in transverse $\vec{k}_{xy}$ plane, as shown in Figure 4.1. Another important task is to evaluate the matrix element

$$\langle f | \hat{p}_z | i \rangle = -i\hbar \int_{-\infty}^{+\infty} dz \varphi_f^*(z) \frac{\partial}{\partial z} \varphi_i(z) . \tag{4.6}$$

As we have known that the envelope wave functions, $\varphi_n(z)$, in a symmetric well schematically shown in Figure 4.1(a) are either even or odd. The derivative changes the parity, and the matrix element will be non-zero only if one state is even and the other odd; *i.e.* $|f - i| = 1,3,5,\cdots$. This is a *selection rule* that governs which transitions can be allowed in optical absorption (or emission). For example, optical absorption is permitted from the lowest state ($n = 1$) to $n = 1,3,5,\cdots$, but not to odd values of n (Figure 4.1). The result can apply to any symmetric well, however it can be defeated by deliberately growing an asymmetric well.

In addition, instead of using the matrix elements themselves, it is useful to introduce a quantity, so-called *the oscillator strength* F_{fi}, to characterize the strength of an optical transition, defined by [83, 84]

$$F_{fi} = \frac{2}{m^* \hbar\omega} \left| \langle f | \hat{p}_z | i \rangle \right|^2 = \frac{2m^*\omega}{\hbar} \left| \langle f | z | i \rangle \right|^2 . \tag{4.7}$$

The latter matrix element z_{fi} is called *the dipole matrix element*, and is commonly quoted. The strengths of optical transitions can be manipulated through the oscillator

strength by changing the shape of the QW, or by modifying the occupations through doping, injection of carriers, pumping, or simply a change in temperature.

4.1.2 Distribution Functions :

Fermi-Dirac and Boltzmann Distribution Functions

Distribution function is a function representing the average number of particles that occupy a state, which depends on the nature of the particles concerned. For instance, electrons, protons, and other particles carrying a half-integer spin, so-called *fermions*, obey the *Pauli exclusion principle*, which states that no more than on fermion can occupy a given state. The Pauli exclusion principle for fermion restricts the occupation number of a state to be either zero or one. The average occupation is governed by the Fermi-Dirac distribution function $f(E,E_F,T)$,

$$f(E,E_F,T) = \frac{1}{\exp\left[\dfrac{E-E_F(T)}{k_BT}\right]+1}. \qquad (4.8)$$

where k_B is the Boltzmann constant. The energy $E_F(T)$ is usually called the *Fermi level* in semiconductors, which generally depends on the temperature T. The Fermi-Dirac function plotted for several temperatures is shown in Figure 4.2.

The important feature of the Fermi-Dirac distribution function is that it takes values between zero and one, as it is expected from the exclusion principle. The transition from one to zero becomes more rapid as the temperature decreases, and it becomes a Heaviside unit step function in the limit of zero temperature,

$$f(E,E_F,T=0\mathrm{K}) = \Theta\left(E_F^0-E\right). \qquad (4.9)$$

Thus all states below E_F^0 are completely filled, and those above are empty. In fact, the notation E_F^0 of $E_F(T)$ at zero temperature is the strict definition of the Fermi level, and the quantity $E_F(T)$ is generally called the *chemical potential* μ; *i.e.* $E_F = \lim_{T\to 0}\mu$. However, standard usage in semiconductor physics is to call both the *Fermi level.*

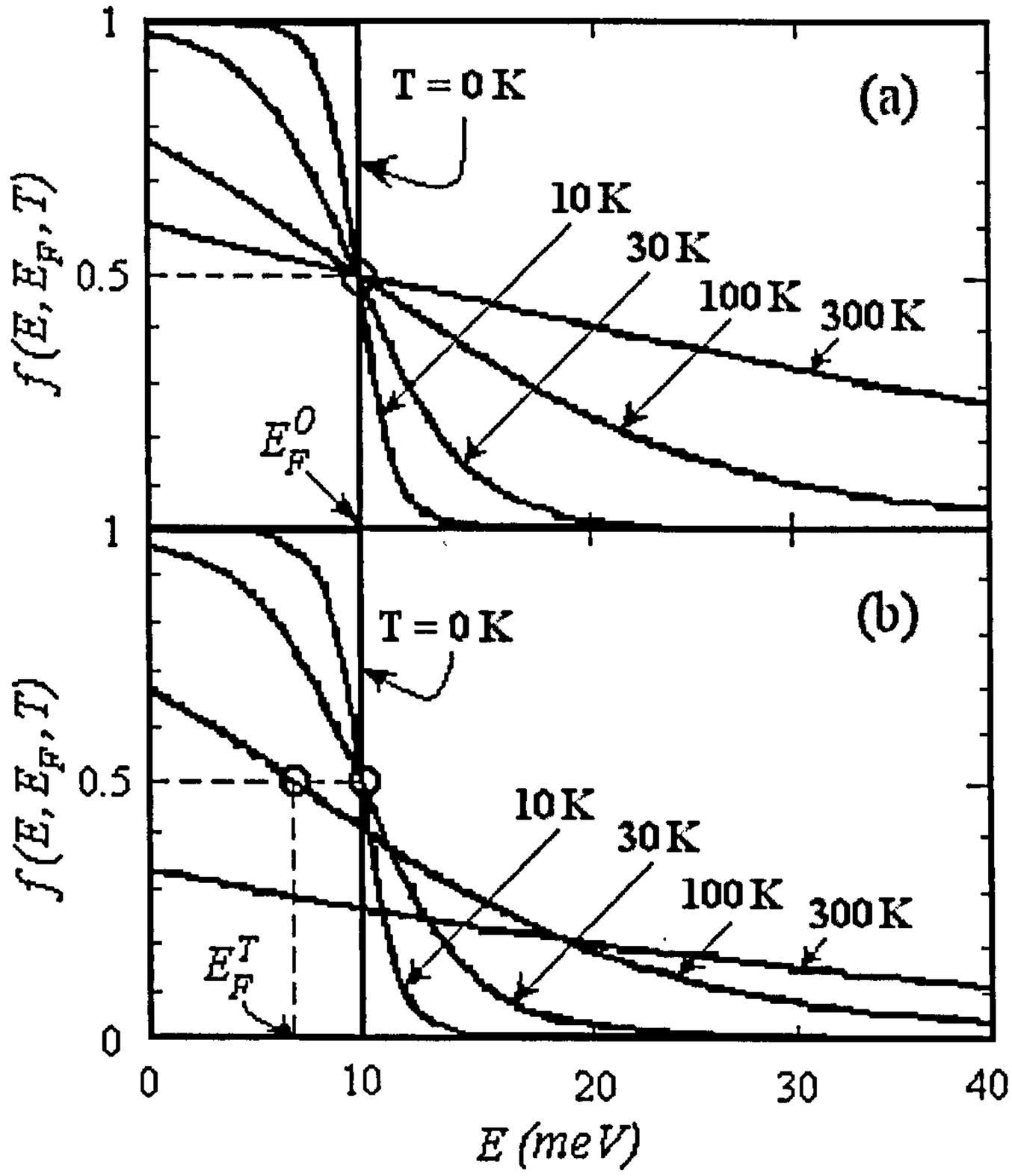

Figure 4.2 Fermi-Dirac distribution function at different temperatures : 0 K, 10K, 30K, 100K and 300K. **(a)** For the case of a constant Fermi level $E_F = 10$ meV. **(b)** For a two-dimensional electron gas (2DEG) in GaAs at constant density $n_{2D} \approx 3\times10^{11}\,\mathrm{cm}^{-2}$. The Fermi level E_F moves downward from E_F^0 as the temperature rises [83].

At the energies far above E_F; on the other word $E - E_F >> k_B T$, the exponential term in Eq.(4.8) is much larger than one. Thus the distribution function becomes

$$f(E, E_F, T) \approx \exp\left(-\frac{E - E_F}{k_B T}\right). \tag{4.10}$$

This is the *Boltzmann distribution*. In our present work, the calculated distribution function of electrons in each subband is mainly investigated at the energies far above E_F. The Fermi-Dirac and Boltzmann distribution functions are plotted together for comparison in Figure 4.3.

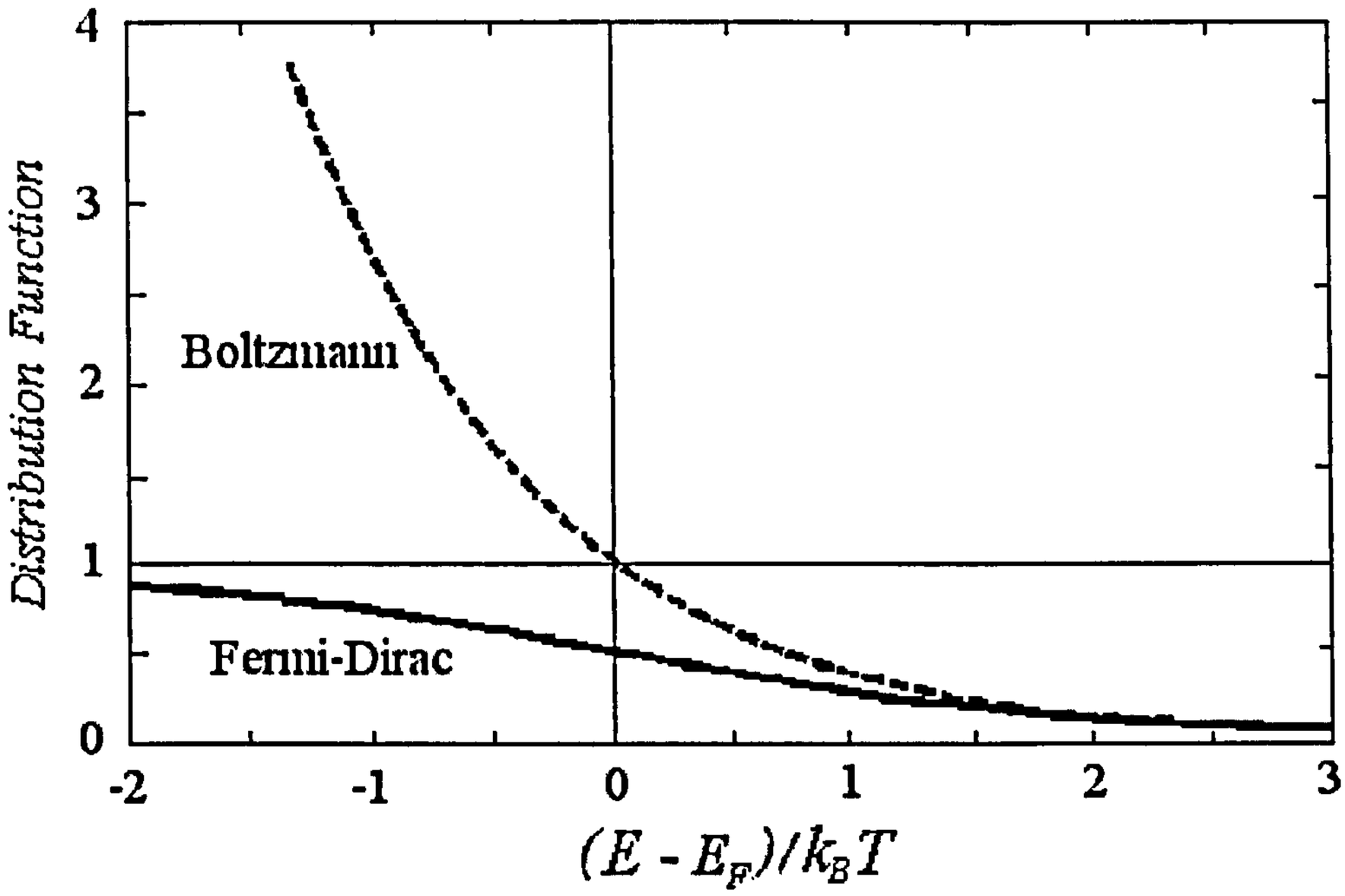

Figure 4.3 Fermi-Dirac and Boltzmann distribution functions plotted on a common scale against $\frac{E - E_F}{k_B T}$.

4.1.3 Basic Laser Physics :

Spontaneous and stimulated emission (or absorption)

The laser *(LASER ≡ Light Amplification by Stimulated Emission of Radiation)* is a source of highly directional, monochromatic and coherent light. The last three letters in the word *LASER* are intended to imply how the device operates by the *stimulated emission of radiation*. In general, the emission of radiation when excited electrons fall to lower energy states occur randomly and can therefore be categorized as *spontaneous emission*. This mean that the instant rate at which electrons fall from the subband E_2 to a lower subband E_1 (see Figure 4.4) is proportional to the number of electrons remaining in E_2 (the population of E_2). Thus, it is expected an exponential emptying of the electrons to the lower subband with a spontaneous decay time $\tau_{spon.}$ describing how much time an electron spends in the E_2 subband. However, if conditions are appropriate, the electron in the upper subband can be stimulated to fall to the lower one

by emitting photon in a time $\tau_{stim.}$ much shorter than its spontaneous decay time; *i.e.* $\tau_{stim.} << \tau_{spon.}$. The stimulus is due to the presence of photons of the proper frequency.

Let us consider an electron in the subband E_2 waiting to drop to the lower subband E_1 with the emission of a photon of energy $\hbar\Omega = E_2 - E_1$ shown in Figure 4.4. Now we assume that this electron in the upper level is immersed in an intense field of photons, each having energy $\hbar\Omega = E_2 - E_1$, and in phase with the other photons. The electron is induced to fall from E_2 to E_1, contributing a photon whose wave is *in phase* with the radiation field. If this process continues and other electrons are stimulated to emit photons in the same fashion, a large radiation field can build up. This radiation will be monochromatic since each photon will have energy of precisely $\hbar\Omega = E_2 - E_1$ and will be coherent, because all the released photons will be in phase and reinforcing. This process of stimulated emission can be described quantum mechanically to relate the probability of emission to the intensity of the radiation field.

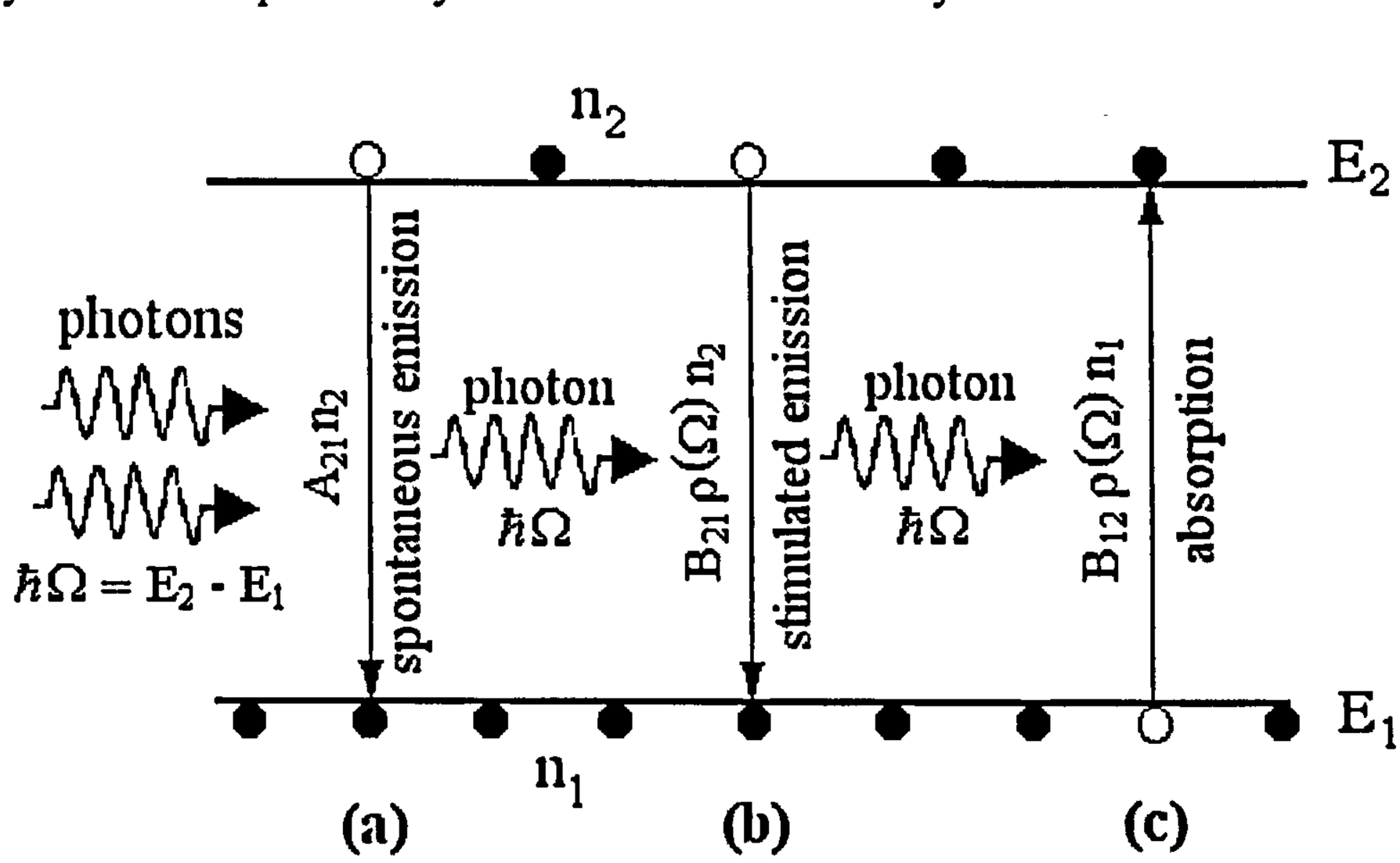

Figure 4.4 Schematic diagram of radiative processes of electrons in subbands E_1 and E_2: **(a)** spontaneous emission, **(b)** stimulated emission, and **(c)** absorption.

A few observations about the relative rates at which the absorption and emission processes occur can be simply described by *Einstein method* [97,98]. If the electrons exist in a radiation field of photons with energy $\hbar\Omega$, such that the energy density of the field is $\rho(\Omega)$, then stimulated emission can occur along with absorption and spon-

taneous emission. The rate of stimulated emission is proportional to and to the energy density of the stimulating field $\rho(\Omega)$ and to the electron population in the upper subband n_2. Therefore, the stimulated rate can be written as $B_{12}\rho(\Omega)n_2$, where B_{12} is a proportionality factor for stimulated emission. The rate at which the electrons in E_1 absorb photons should also be proportional to the photon field energy density $\rho(\Omega)$ and to the electron population in E_1. The absorption rate can be given as $B_{21}\rho(\Omega)n_1$, where B_{21} is a proportionality factor for absorption. Finally, the rate of spontaneous emission is proportional only to the electron population in the upper subband. Introducing another proportionality factor for spontaneous emission A_{12}, the rate of the emission can be written as $A_{12}n_2$. For steady state at which the two emission rates must balance the rate of absorption to maintain constant populations n_1 and n_2, we have

$$B_{21}\rho(\Omega)n_1 = A_{12}n_2 + B_{12}\rho(\Omega)n_2 \ . \tag{4.11}$$

In general, the coefficients A_{12}, B_{12} and B_{21} are so-called the *Einstein coefficients*.

For thermal equilibrium, at which the Boltzmann distribution function takes into account the relative population will be

$$\frac{n_2}{n_1} = \exp\left(-\frac{E_2 - E_1}{k_B T}\right) = \exp\left(-\frac{\hbar\Omega}{k_B T}\right). \tag{4.12}$$

According to Planck's law, the radiation field is

$$\rho(\Omega) = \left(\frac{2\hbar\Omega^3}{\pi c^3}\right)\frac{1}{\exp\left(\frac{\hbar\Omega}{k_B T}\right) - 1}, \tag{4.13}$$

here c is the speed of light. Substituting these relevant terms into Eq.(4.10),

$$\left(\frac{\pi c^3}{2\hbar\Omega^3}\right)\frac{A_{12}}{B_{21}}\left[\exp\left(\frac{\hbar\Omega}{k_B T}\right) - 1\right] + \frac{B_{12}}{B_{21}} = \exp\left(\frac{\hbar\Omega}{k_B T}\right). \tag{4.14}$$

Because this expression, Eq.(4.14), must hold for all temperature T. Thus

$$\left(\frac{\pi c^3}{2\hbar\Omega^3}\right)\frac{A_{12}}{B_{21}} = 1 \quad ; \quad \frac{B_{12}}{B_{21}} = 1 \,. \tag{4.15}$$

Finally, with a presence of photon field

$$\frac{\text{Stimulated emission rate}}{\text{Spontaneous emission rate}} = \frac{B_{12}\rho(\Omega)}{A_{12}} = \left(\frac{2\hbar\Omega^3}{\pi c^3}\right)\rho(\Omega) \,. \tag{4.16}$$

As Eq.(4.16) indicates, the way to enhance the stimulated emission over spontaneous emission is to have a very large photon field energy density $\rho(\Omega)$. In the laser, this condition is fulfilled by providing an *optical resonant cavity* in which the photon density can build up to a large value through multiple internal reflections at certain frequencies. Similarly,

$$\frac{\text{Stimulated emission rate}}{\text{Asorption rate}} = \frac{B_{12}\rho(\Omega)n_2}{B_{21}\rho(\Omega)n_1} = \frac{n_2}{n_1} \,. \tag{4.17}$$

This suggests that it is possible to have stimulated emission dominated over absorption of photons from the radiation field if we have a right condition of maintaining more electrons in the upper subband than in the lower subband; *i.e.* $n_2 > n_1$. This condition is quite unnatural since, in general, $n_2 < n_1$ for any equilibrium case. Because of its unusual nature, the condition $n_2 > n_1$ is so-called *population inversion*.

In summary, Eq.(4.16) and (4.17) indicate that if the photon density is to build up through a predominance of stimulated emission over both spontaneous emission and absorption, the device must provide such the two relevant requirements: (i) an optical resonant cavity to encourage the photon field to build up, and (ii) a means of obtaining population inversion.

4.2 Formulation of the model kinetic equations

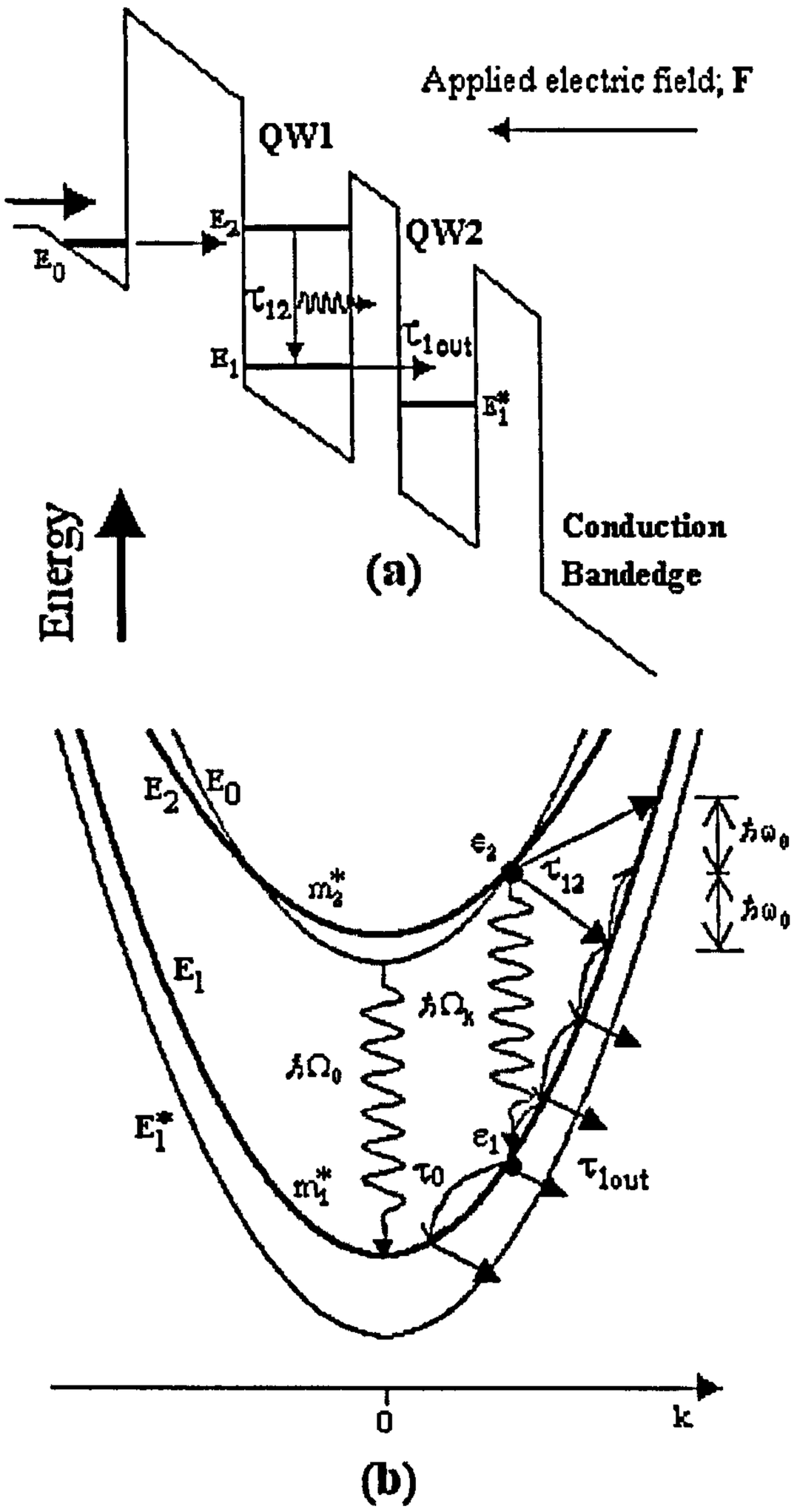

Figure 4.5 **(a)** Schematic diagram of the conduction bandedge of a DQW structure and kinetics of electrons scattering. **(b)** The subband diagram presenting the radiative intersubband transitions in the QW1, and also shown the nonradiative inter- and intrasubband transitions by emission or absorption of LO phonons.

Kinetics of electron scattering shown schematically in Figure 4.5 can be described by a model kinetic equation [99-101]

$$\frac{\partial f_i(\varepsilon_i)}{\partial t} = S_{LO}(\varepsilon_i)+C_{ee}(\varepsilon_i)+R_i(\varepsilon_i)+G_i(\varepsilon_i) \quad ; \quad i=1,2 \qquad (4.18)$$

where $f_i(\varepsilon_i)$ is the electron energy distribution function, corresponding to the occupation probability of kinetic energy states ε_i in subband E_i; here E_i denotes the total energy of electrons. We consider the dispersion relations $\varepsilon_{1,2}(k)$ in both subbands are different and nonparabolic. However, all the effects of interest here are simplified by regarding the subbands themselves as parabolic, but characterized by different effective mass m_1^* and m_2^* [91]

$$\varepsilon_{1,2}(k) = E_{1,2}(k)+E_{1,2}(0) = \frac{\hbar^2 k^2}{m_{1,2}^*}, \tag{4.19}$$

here $k \equiv k_{xy}$ is the magnitude of in-plane wave vector of the electron.

Electron-LO-phonon scattering: The term $S_{LO}(\varepsilon_i)$ is responsible for electron scattering by LO phonons in subband E_i [100]

$$S_{LO}(\varepsilon_i) = -\gamma(\varepsilon_i)f_i(\varepsilon_i) + B_i(\varepsilon_i), \tag{4.20}$$

$$\gamma(\varepsilon_i) = \frac{1}{\tau_0}\times[N_0+(N_0+1)\Theta(\varepsilon_i-\hbar\omega_0)], \tag{4.21}$$

$$B_i(\varepsilon_i) = \frac{1}{\tau_0}\times[(N_0+1)f_i(\varepsilon_i+\hbar\omega_0) + N_0\Theta(\varepsilon_i-\hbar\omega_0)f_i(\varepsilon_i-\hbar\omega_0)], \tag{4.22}$$

where Θ is a Heaviside step function, and τ_0 the intrasubband relaxation time due to a spontaneous LO-phonon emission. For a sufficient narrow QW of any shape, the time constant $\tau_0 \approx 0.1\,\text{ps}$ (for GaAs) [90,91,102]. N_0 is the phonon distribution function. If LO phonons are strongly nonequilibrium [103], the appropriate function is used instead of N_0. In our case it will lead to an effective LO phonon temperature which differs from the lattice temperature T_L. The function $\gamma(\varepsilon_i)$ describes the transverse phase relaxation rate due to the intrasubband scattering which is dominated by the interaction with LO phonons. The latter term $B_i(\varepsilon_i)$ is responsible for the scattering-in of the electron by emission (or absorption) of LO phonons.

Electron-electron scattering: To calculate the term $C_{ee}(\varepsilon_i)$ that describes e-e scattering processes, one has to consider the e-e scattering probability $W_{ee}(\varepsilon_i \to \varepsilon'_f)$ of interacting electrons from initial states ε_i in subband E_i to the final states ε'_f in subband E_f. In a system with isotropic or nearly isotropic electron distributions, the probability $W_{ee}(\varepsilon_i \to \varepsilon'_f)$ is given by [99]

$$W_{ee}(\varepsilon_i \to \varepsilon'_f) = \frac{1}{\pi} \int_0^{\pi} d\phi W_{ee}(\vec{k}_i \to \vec{k}'_f) , \tag{4.23}$$

$$W_{ee}(\vec{k}_i \to \vec{k}'_f) = \sum_{\vec{k}_j, \vec{k}'_g} f_j(\varepsilon_j) \frac{2\pi}{\hbar} \left| M_{\vec{k}'_f, \vec{k}'_g; \vec{k}_i, \vec{k}_j} \right|^2 \delta(\varepsilon_i + \varepsilon_j - \varepsilon'_f - \varepsilon'_g) , \tag{4.24}$$

where $M_{\vec{k}'_f, \vec{k}'_g; \vec{k}_i, \vec{k}_j}$ is the matrix element for the e-e scattering process of an electron with wave vector $\vec{k}_i$ in subband E_i and a second electron with wave vector $\vec{k}_j$ in subband E_j into the final states with wave vector k'_f and k'_g in subbands E_f and E_g, respectively. For the problem with isotropic electron distributions, the average of the probability $W_{ee}(\vec{k}_i \to \vec{k}'_f)$ over the angle ϕ between $\vec{k}_i$ and $\vec{k}'_f$ enters into the calculations as given in Eq.(4.23).

In order to simplify our calculations we neglect any mismatch in the properties of the narrow- and wide-gap semiconductor lattices and also disparities in the dielectric permittivity. An e-e interaction operator is therefore, $U_{ee} = \frac{e^2}{4\pi\varepsilon_0\kappa_\infty r}$; where r is the distance between two interacting electrons. The matrix element $M_{\vec{k}'_f, \vec{k}'_g; \vec{k}_i, \vec{k}_j}$ is consequently obtained [99]

$$M_{\vec{k}'_f, \vec{k}'_g; \vec{k}_i, \vec{k}_j} = \left\langle \vec{k}'_f, \vec{k}'_g \left| \frac{e^2}{4\pi\varepsilon_0\kappa_\infty r} \right| \vec{k}_i, \vec{k}_j \right\rangle = \frac{1}{S}\left(\frac{e^2}{2\varepsilon_0\kappa_\infty Q}\right)\delta_{\vec{k}'_f - \vec{k}'_g, \vec{k}_i - \vec{k}_j} , \tag{4.25}$$

where $Q = |\vec{k}'_f - \vec{k}'_g| = |\vec{k}_i - \vec{k}_j|$ is the relative in-plane wave vector of the interacting electrons, which determines the in-plane momentum transfer of the electrons, and S the surface area of the QW.

Finally, one can obtain the e-e scattering $C_{ee}(\varepsilon_i)$ in the collision integral form [99,100]

$$C_{ee}(\varepsilon_i) = \int_0^\infty d\varepsilon'_j \rho_j(\varepsilon'_j)\left[W_{ee}(\varepsilon'_j \to \varepsilon_i) f_j(\varepsilon'_j) - W_{ee}(\varepsilon_i \to \varepsilon'_j) f_i(\varepsilon_i)\right], \quad (4.26)$$

where $\rho_j(\varepsilon_j) = \frac{m_j^*}{\pi\hbar^2}$ is the 2D density of states in subband E_j.

The general expression for $C_{ee}(\varepsilon_i)$ given by Eq.(4.26) associated with Eqs.(4.23)-(4.25) is very complicated as it is a bilinear function of the electron distribution function, on the contrary to the other terms S_{LO}, R_i and G_i. To reduce it to a linear integral equation form one can put in Eq.(4.24) the Maxwellian distribution

$$f_i(\varepsilon_i) = n_i\left(\frac{\pi\hbar^2}{m_i^* k_B T_e}\right)\exp\left(-\frac{\varepsilon_i}{k_B T_e}\right), \quad (4.27)$$

where n_i is the number of electrons per unit area in subband E_i and T_e the electron temperature. Physically it means that scattering of the minority of high kinetic-energy electrons is affected only by the projection on the majority of quasi-thermalized electrons. In general, it is meaningful to include an elec-tron temperature T_e that differs from the lattice temperature T_L when the energy relaxation due to e-e scattering is faster than the energy relaxation due to LO-phonon scattering; *i.e.* $\tau_{ee} < \tau_0 \exp\left(-\frac{\hbar\omega_0}{k_B T_e}\right)$ [100]. Under these conditions the temperature T_e can be found using an energy balance equation. Even with this simplification the e-e scattering probability $W_{ee}(\varepsilon_i \to \varepsilon'_f)$ is still complicated and could be solved analy-tically only in some special cases [99,104]. To handle the problem analytically we use a property of the coulomb singularity of the matrix element $M_{\vec{k}'_f,\vec{k}'_g;\vec{k}_i,\vec{k}_j}$ at small momentum transfer. This singularity implies that scattering events with low energy transfer are dominant. As a result, one can use the Fökker-Planck-Landau (FPL) approximation to transform the collision integral Eq.(4.26) into a differential form [100,105]

$$C_{ee}(\varepsilon_i) = -\frac{1}{\rho_i(\varepsilon_i)}\frac{\partial}{\partial\varepsilon_i}[\rho_i(\varepsilon_i)J_{ee}(\varepsilon_i)] = \frac{\partial}{\partial\varepsilon_i}J_{ee}(\varepsilon_i)\,, \tag{4.28}$$

where the flux on the energy axis $J_{ee}(\varepsilon_i)$ is

$$J_{ee}(\varepsilon_i) = -\left[A_{ee}(\varepsilon_i) + D_{ee}(\varepsilon_i)\frac{\partial}{\partial\varepsilon_i}\right]f_i(\varepsilon_i)\,, \tag{4.29}$$

$$A_{ee}(\varepsilon_i) = \int_0^\infty d\varepsilon_i'\rho_i(\varepsilon_i')(\varepsilon_i-\varepsilon_i')W_{ee}(\varepsilon_i\to\varepsilon_i')\,, \tag{4.30}$$

$$D_{ee}(\varepsilon_i) = \frac{1}{2}\int_0^\infty d\varepsilon_i'\rho_i(\varepsilon_i')(\varepsilon_i-\varepsilon_i')^2W_{ee}(\varepsilon_i\to\varepsilon_i')\,, \tag{4.31}$$

where $A_{ee}(\varepsilon_i)$ is the dynamic friction, and $D_{ee}(\varepsilon_i)$ the energy-diffusion coefficients.

Recently, it has been numerically shown by Kinsler *et al.* [94] and Smet *et al.* [101] that e-e scattering is dominated by small angle intrasubband events ($i=f$ and $j=g$) in which the initial electrons stay within their original subband after scattering and their relative momentum transfer is small resulting in a small value of the energy transfer. The main investigations of these papers [94,101] are directed to e-e intersubband scattering ($i\neq f$ or $j\neq g$). In this case the energy of final states of electrons lies in a narrow region. Their resulting calculations show that the intersubband e-e scattering events, which involve a change of subband at least for one of the electrons, vanish at small values of in-plane wave vector $k<k_{\min}$; where $k_{\min}$ is the minimum value of k that permits the intersubband transitions occur. For electrons at large values of in-plane wave vector $k>k_{\min}$, where the e-e intersubband transitions is possible, e-e intersubband scattering processes are typically less important when compared to e-e intrasubband transitions. In addition, they have also pointed out that for the sufficient large values of the energy separation between subband e-e intersubband transitions become much weaker when compared to the e-e intrasubband scattering processes. These relevant results enable us to neglect the e-e intersubband scattering processes and take into account only the e-e intrasubband transitions. For the kinetic

energies $\varepsilon_i >> T_e$ the dynamic friction coefficient $A_{ee}(\varepsilon_i)$ is independent of kinetic energy [99]

$$A_{ee}(\varepsilon_i) \equiv A_{ee} = \left(\frac{e^4}{32\hbar\varepsilon_0^2\kappa_\infty^2}\right)n_s = \frac{\hbar\omega_0}{\tau_{ee}}, \tag{4.32}$$

where $n_s = n_1 + n_2$ is the electron concentration in the QW1 and τ_{ee} is responsible for the e-e relaxation time at LO-phonon threshold. This relaxation time τ_{ee} is important for describing the competition between e-e scattering and the LO phonon emission near the LO phonon threshold, represented by the dimensionless parameter

$$\eta = \frac{\tau_0}{\tau_{ee}} = \left(\frac{\tau_0 e^4}{32\hbar^2\omega_0\,\varepsilon_0^2\kappa_\infty^2}\right)n_s = \frac{n_s}{3.84\times10^{11}\,\mathrm{cm}^{-2}}, \tag{4.33}$$

(for the GaAs QW). At high electron concentration; *i.e.* $\eta >> 1$, e-e scattering is dominant. The e-e scattering rate in our approach defined by Eq.(4.32) differs from the maximum e-e scattering rate introduced by Goodnick and Lugli [88],

$$\Gamma_{\max} = \left(\frac{m_w^* e^4}{4\hbar^3 q_0^2\varepsilon_0^2\kappa_\infty^2}\right)n_s \qquad \text{(in SI units)}, \tag{4.34}$$

where m_w^* stands for the electron effective mass in the QWs and q_0 is the inverse screening length in two dimensions. The reason for obtaining the definition of the e-e scattering in our approach is that electron gas energy transfer rate is determined by transport cross-section which differs from the total cross-section of the screened Coulomb potential that has been used in the Monte Carlo simulations [88]. If screening parameter $q_0 << \sqrt{\frac{2m_w^*\omega_0}{\hbar}}$, τ_{ee} appears to be kinetic-energy independent that makes the problem more simplistic.

Electron escape from the subband: The term $R_i(\varepsilon_i)$, in Eq.(4.18), describes electron escape from subband E_i. For the lower subband E_1 in QW1 (see Figure 4.5) the electron escape rate is

$$R_1(\varepsilon_1) = -\frac{f_1(\varepsilon_1)}{\tau_{1out}}, \tag{4.35}$$

where τ_{1out} is the electron escape time from the subband due to various types of scattering mechanisms. In this present work we take into account only LO-phonon assisted tunneling which is typically the most prominent scattering process, so that

$$R_1(\varepsilon_1) = -(2N_0+1)\frac{f_1(\varepsilon_1)}{\tau_1}, \tag{4.36}$$

here τ_1 is the interwell scattering time due to a spontaneous LO-phonon emission. The nonradiative time τ_1 can be tuned by changing the design parameters of the QWs and barriers. To achieve the efficient removal of electrons from subband E_1 the designed structure must be such that the subband energy difference $E_1 - E_1^*$ is close to the LO-phonon energy. For a GaAs/$Al_xGa_{1-x}As$ DQW structure utilizing LO-phonon tunneling, the calculated time constant τ_1 is in the range 0.4 - 1.0 ps depending upon the coupling strength between the electronic states of the two subbands E_1 and E_1^* [62,63]. However, in the present work it is regarded as a tunable parameter to determine the global population ratio between E_2 and E_1 subbands.

For subband E_2 the electron escape rate $R_2(\varepsilon_i)$ can be determined by intersubband LO-phonon assisted scattering from the subband E_2 down to subband E_1, neglecting any other scattering mechanisms including the tunneling through out the subband. Therefore, the electron escape rate is

$$R_2(\varepsilon_2) = -(2N_0+1)\frac{f_2(\varepsilon_2)}{\tau_{12}}, \tag{4.37}$$

where τ_{12} is the intrawell scattering time due to a spontaneous LO-phonon emission from subband E_2 down to subband E_1. The typical nonradiative time $\tau_{12} \approx 1\,\text{ps}$ (in GaAs QW) for mid-infrared regime of operation [13,14,106].

Electron generation processes: The term $G_i(\varepsilon_i)$, in Eq.(4.18), describes the electron generation in subband E_i. For the lower subband the electron generation $G_1(\varepsilon_1)$ can be obtained from the intersubband scattering rates of electron from the upper subband

$$G_1(\varepsilon_1) = \frac{1}{\tau_{12}}\frac{m_2^*}{m_1^*}[(N_0+1)f_2(\varepsilon_1-\hbar\Omega_0+\hbar\omega_0) + N_0 f_2(\varepsilon_1-\hbar\Omega_0-\hbar\omega_0)], \quad (4.38)$$

where $\hbar\Omega_0 = E_2(0)-E_1(0)$ is the energy separation between the two subbands. The first term is responsible for the emission of LO phonons, while the latter term stands for the absorption of LO phonons.

Electron generation $G_2(\varepsilon_2)$ in the upper subband is assumed to be monoenergetic for the following reasons:

(i) For a strong nonparabolic material the 2D electron gas (2DEG) in the emitter is permitted to tunnel through the upper subband E_2 in QW1; see also Figure 4.5(a), only for a definite wave vector k; *i.e.* the definite kinetic energy ε_2.

(ii) Similarly, for the case of optical pumping only the photoelectrons with a definite wave vector k are allowed to be pumped into the E_2 subband. This is equivalent to requiring the definite kinetic energy ε_2 to be pumped into the subband.

(iii) The third main reason is that the model kinetic equation in our approach is linear. This implies that if one can find its solution with a $\delta-$function pumping, one will be able to build up the convolution of general problems with arbitrary generation functions.

Consequently, the electron generation in the upper subband is therefore

$$G_2(\varepsilon_2) = -\frac{G_0}{\rho_2}\delta(\varepsilon_2-\varepsilon_0), \quad (4.39)$$

where G_0 is the number of electrons with kinetic energy ε_0 and $\rho_2(\varepsilon_2)=\frac{m_2^*}{\pi\hbar^2}$ is the 2D density of states in the subband E_2.

By substituting all of the relevant scattering terms, S_{LO}, C_{ee}, R_i and G_i into the kinetic equation Eq.(4.18) under steady state conditions, one can obtain

$$\frac{\hbar\omega_0}{\tau_{ee}}\left[\frac{d}{d\varepsilon_i}+k_B T_e\frac{d^2}{d\varepsilon_i^2}\right]f_i(\varepsilon_i)-\gamma(\varepsilon_i)f_i(\varepsilon_i)+B_i(\varepsilon_i)+R_i(\varepsilon_i) = -G_i(\varepsilon_i), \quad (4.40)$$

here $T_e = \dfrac{D_{ee}(\varepsilon_i)}{k_B A_{ee}(\varepsilon_i)}$ is the electron temperature of the 2D electrons below the LO-phonon threshold. It follows from the principle of detailed balance that a 2DEG below the LO-phonon threshold represents a thermal bath with temperature T_e.

In addition to the dimensionless parameter $\eta = \dfrac{\tau_0}{\tau_{ee}}$, we introduce $\xi_1 = \dfrac{\tau_0}{\tau_1}$, $\xi_2 = \dfrac{\tau_0}{\tau_{12}}$, $\Lambda_{ee} = \dfrac{k_B T_e}{\hbar\omega_0}$ and $y_i = \dfrac{\varepsilon_i}{\hbar\omega_0}$. The ratio $\dfrac{\xi_1}{\xi_2}$ characterizes the global population ratio between the two subbands involved. The dimensionless parameter Λ_{ee} determines the ratio of electron temperature to LO-phonon energy. In our approach it is always assumed to be small. As a result of substituting these dimensionless parameters into the kinetic equation Eq.(4.40), one can obtain a four dimensionless kinetic equation system to eliminate the step function Θ, that takes into account the LO phonon threshold, as follows:

(i) *For the upper subband* E_2*:*

(a) $0 < y_2 < 1$;

$$\eta\Lambda_{ee}\frac{d^2 f_2(y_2)}{dy_2^2} + \eta\frac{df_2(y_2)}{dy_2} + (N_0+1)f_2(y_2+1) - \alpha_2 f_2(y_2) = -P_0\delta(y_2 - y_0), \tag{4.41}$$

(b) $y_2 > 1$;

$$\eta\Lambda_{ee}\frac{d^2 f_2(y_2)}{dy_2^2} + \eta\frac{df_2(y_2)}{dy_2} + (N_0+1)f_2(y_2+1) + N_0 f_2(y_2-1) - \beta_2 f_2(y_2) = 0, \tag{4.42}$$

(ii) *For the lower subband* E_1*:*

(a) $0 < y_1 < 1$;

$$\eta\Lambda_{ee}\frac{d^2 f_1(y_1)}{dy_1^2} + \eta\frac{df_1(y_1)}{dy_1} + (N_0+1)f_1(y_1+1) - \alpha_1 f_1(y_1) = 0, \tag{4.43}$$

(b) $y_1 > 1$;

$$\eta\Lambda_{ee}\frac{d^2 f_1(y_1)}{dy_1^2}+\eta\frac{df_1(y_1)}{dy_1}+(N_0+1)f_1(y_1+1)+N_0 f_1(y_1-1)-\beta_1 f_1(y_1) = P_1(y_1),$$

(4.44)

where $\alpha_{1,2} = N_0 + \xi_{1,2}(2N_0+1)$, $\beta_{1,2} = (2N_0+1)(1+\xi_{1,2})$, $P_0 = \frac{\tau_0 G_0}{\rho_2 \hbar\omega_0}$, and

$$P_1 = \xi_2\left(\frac{m_2^*}{m_1^*}\right)\left[(N_0+1)f_2\left(y_1+1-\frac{\hbar\Omega_0}{\hbar\omega_0}\right)+N_0 f_2\left(y_1-1-\frac{\hbar\Omega_0}{\hbar\omega_0}\right)\right].$$

The details of mathematical solution of Eqs.(4.41)-(4.44) are presented in Appendix A, where boundary conditions for these equations are also presented. In the following section the resulting solutions of the kinetic equation system for various values of the relevant parameters η, ξ_1, ξ_2 and Λ_{ee} are presented.

4.3 Subband distribution functions

Nonequilibrium electrons in a GaAs/$Al_xGa_{1-x}As$ DQW heterostructure shown in Figure 4.5 are investigated. A universal dimensionless energy variable $y = \frac{\varepsilon_2}{\hbar\omega_0}$ for subband distribution functions $f_1(y_1)$ and $f_2(y)$ are introduced; here $y_1 = \frac{m_2^*}{m_1^*}y$. The calculated subband distribution functions for different values of η are shown in Figure 4.6. With increasing values of η; *i.e.* increasing the concentrations of electrons, the subband distribution functions below the LO-phonon threshold ($y<1$) in both sub-bands become close to Maxwellian distributions. In the region above LO-phonon threshold ($y>1$), the shape of the upper subband distributions $f_2(y)$ are still close to Maxwellian while for the lower subband the distributions $f_1(y)$ are always strongly nonequilibrium and deviate far from Maxwellian.

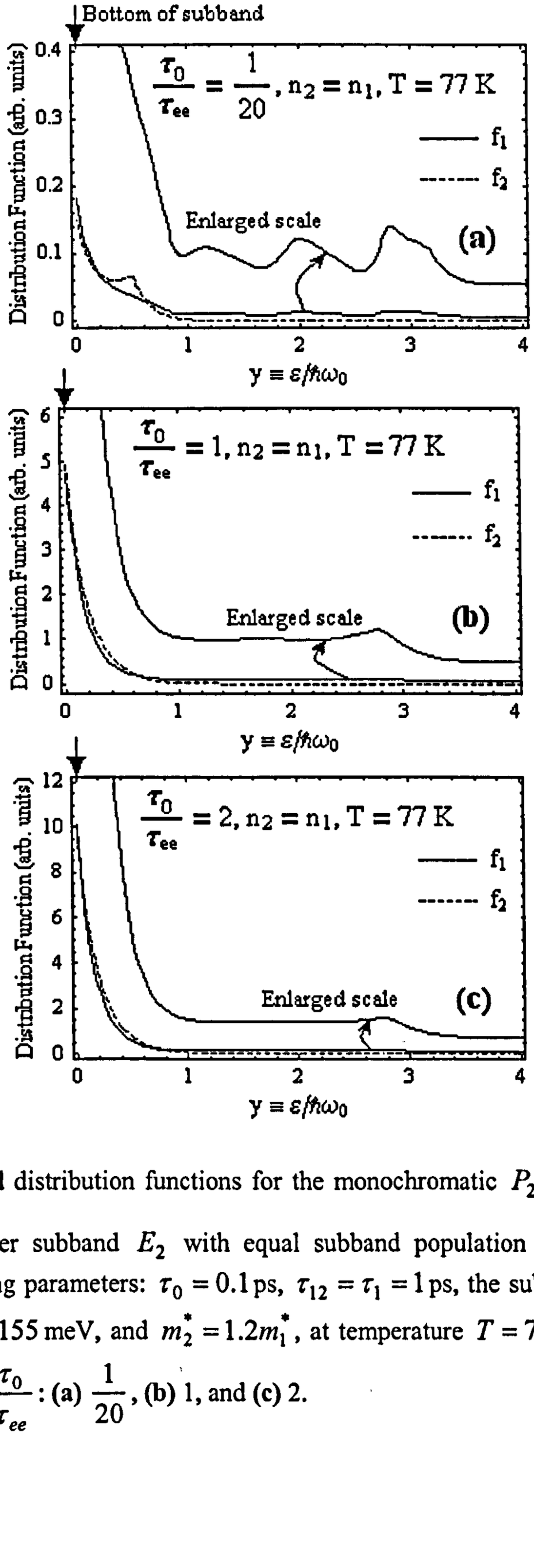

Figure 4.6 Subband distribution functions for the monochromatic $P_2(y) = P_0\delta\left(y - \frac{1}{2}\right)$ into the upper subband E_2 with equal subband population $n_2 = n_1$; assuming the following parameters: $\tau_0 = 0.1\,\text{ps}$, $\tau_{12} = \tau_1 = 1\,\text{ps}$, the subband separation energy $\hbar\Omega_0 = 155\,\text{meV}$, and $m_2^* = 1.2m_1^*$, at temperature $T = 77\,\text{K}$ for different values of $\eta \equiv \frac{\tau_0}{\tau_{ee}}$: (a) $\frac{1}{20}$, (b) 1, and (c) 2.

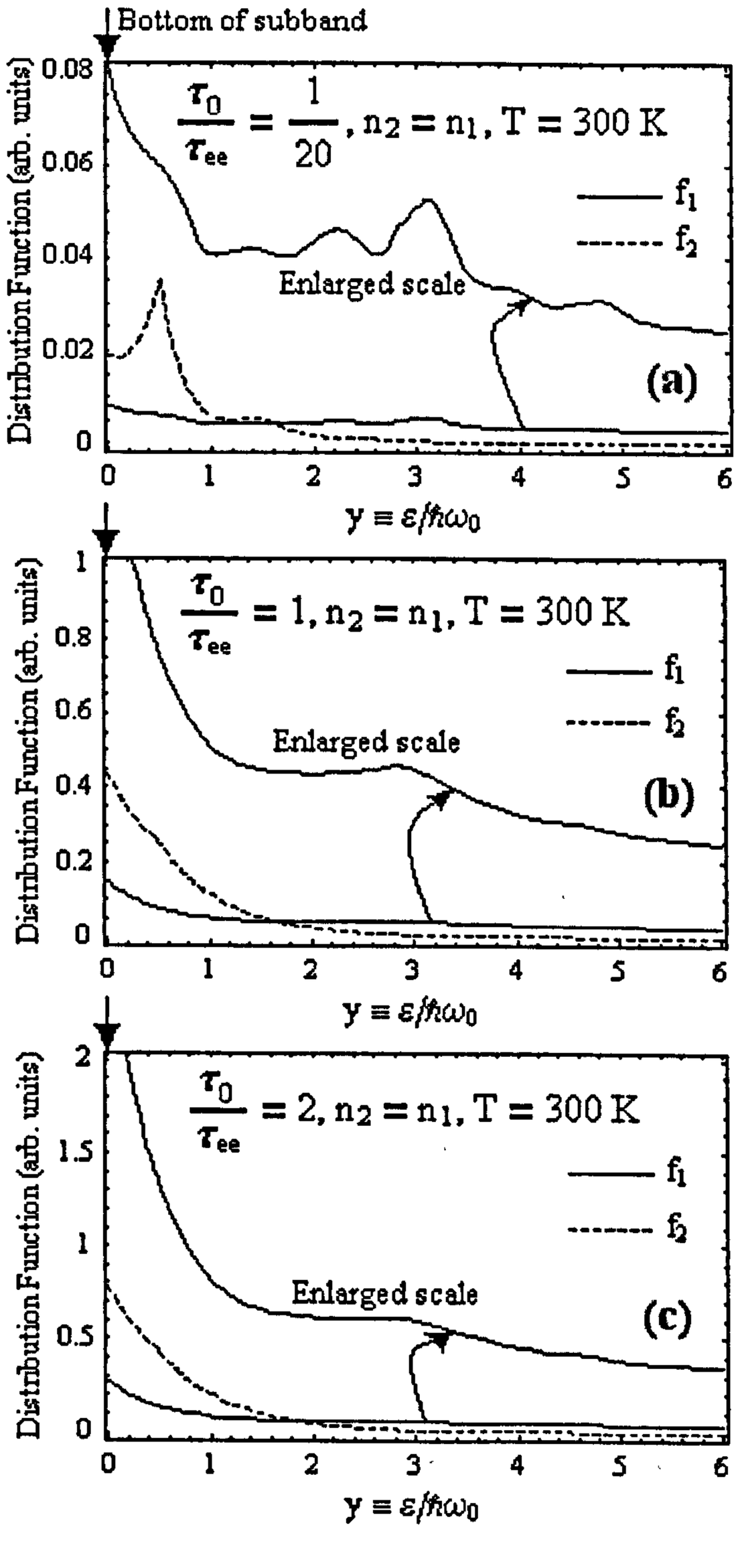

Figure 4.7 Subband distribution functions for the monochromatic $P_2(y) = P_0\delta\left(y - \frac{1}{2}\right)$ into the upper subband E_2 with equal subband population $n_2 = n_1$; assuming the following parameters: $\tau_0 = 0.1\,\text{ps}$, $\tau_{12} = \tau_1 = 1\,\text{ps}$, the subband separation energy $\hbar\Omega_0 = 155\,\text{meV}$, and $m_2^* = 1.2m_1^*$, at room-temperature $T = 300\,\text{K}$ for different values of $\eta \equiv \frac{\tau_0}{\tau_{ee}}$: **(a)** $\frac{1}{20}$, **(b)** 1, and **(c)** 2.

At a very low electron concentration limit, $n_s << 1\times10^{11}\,\mathrm{cm}^{-2}$; *i.e.* $\eta << 1$, the dominant scattering process is due to LO phonon transitions within the subband. The distribution functions for $\eta = \frac{1}{20}$; *i.e.* $n_s = 1.92\times10^{10}\,\mathrm{cm}^{-2}$ at different operating temperature $T = 77\,\mathrm{K}$ and 300 K are shown in Figures 4.6(a) and 4.7(a), respectively. Following calculations have been done for a chosen situation $\tau_{12} = \tau_1$ that results in the equal subband population. Our purpose is to investigate the possibility to achieve positive gain without global population inversion.

The results show that the shape of the distribution functions in both subbands deviates far from Maxwellian. In the upper subband they have a pronounced peak at the pumping energy affected by the monochromatic electron generation process that plays an essential role in this regime of operation. Immediately after nonradiative intersubband transitions from the upper subband E_2 down to the lower subband E_1, the lower subband electrons are in a state of high kinetic energy $\varepsilon_1 = \hbar\Omega_0 + \varepsilon_2 \pm \hbar\omega_0$. Consequently, they cascade down to the subband bottom by emitting LO phonons with the result that the distribution functions $f_1(y)$ at steady state are strongly nonequilibrium. For $\eta = \frac{1}{20}$ at temperature $T = 77\,\mathrm{K}$, one can observe four pronounced peaks in the lower subband distribution function $f_1(y)$. However, its shape deviates far from the shape of $f_2(y)$ at low kinetic energies. At $\eta = 1$ all peaks are completely smeared out, but the large shoulder below the main peak always remains.

In Figure 4.7 electron distributions calculated for the system with the same parameters as in Figure 4.6, but operating at room temperature $T = 300\,\mathrm{K}$ are presented. The investigation focuses on the distribution functions affected by the thermal phonon population N_0, which governs the lattice temperature T_L. By comparing the resulting calculations for a specific value of η at different operating temperatures $T = 77\,\mathrm{K}$ and 300 K, it is clear that the nonequilibrium electron behaviour is strongly dependent on the lattice temperature. The main interest of these resulting calculations as shown in Figures 4.6 and 4.7 are addressed to the case $\frac{\xi_1}{\xi_2} = 1$, which corresponds to equal subband population $n_2 = n_1$.

The results show that it is possible to achieve positive values of the spectral gain $g(\Omega)$ due to the existence of local population inversions at some definite kinetic energies ε_2; *i.e.* at some particular electron wave vectors k, in the region below the LO-phonon threshold that provides an essential contribution to the spectral gain density. This implies that it is possible to achieve laser action even in low electron concentration regimes of high temperature operation; see also Figure 4.7(a). In addition, it is also found that the width and position of the peak gain depends strongly on the pumping energy into the E_2 subband.

4.4 Spectral density of gain

In the limit that the transverse phase relaxation rate $\gamma(\varepsilon)$ is much smaller than the optical frequency Ω, optical gain spectra $g(\Omega)$ can be expressed as a function of the subband distribution function $f_1(\varepsilon_1)$ and $f_2(\varepsilon \equiv \varepsilon_2)$ [90,91]

$$g(\Omega) = \frac{4e^2|z_{12}|^2 m_2^* \Omega}{\hbar^3 L_1 c\sqrt{\varepsilon_0 \kappa_\infty}} \int_0^\infty d\varepsilon \frac{\gamma(\varepsilon)[f_2(\varepsilon) - f_1(\varepsilon_1)]}{[\Omega - \Omega_k(\varepsilon)]^2 + [\gamma(\varepsilon)]^2}, \tag{4.45}$$

where z_{12} is the dipole matrix element, κ_∞ the dielectric constant at high frequency, ε_0 the permittivity of vacuum, L_1 the QW1 width and c the speed of light. The vertical transitions with particular $\hbar\Omega_k(\varepsilon)$; see also Figure 4.5, are given by

$$\hbar\Omega_k(\varepsilon) = \hbar\Omega_0 + \varepsilon - \varepsilon_1 = \hbar\Omega_0 - \varepsilon\left(\frac{m_2^*}{m_1^*} - 1\right), \tag{4.46}$$

According to the threshold nature of $\gamma(\varepsilon)$ that has been discussed in Section 4.2 the optical gain becomes strongly influenced by the nonequilibrium distributions in the two subbands. Gain spectra calculated for different values of the competition parameter η between e-e scattering and electron-LO-phonon scattering for different values of the electron concentrations are shown in Figure 4.8.

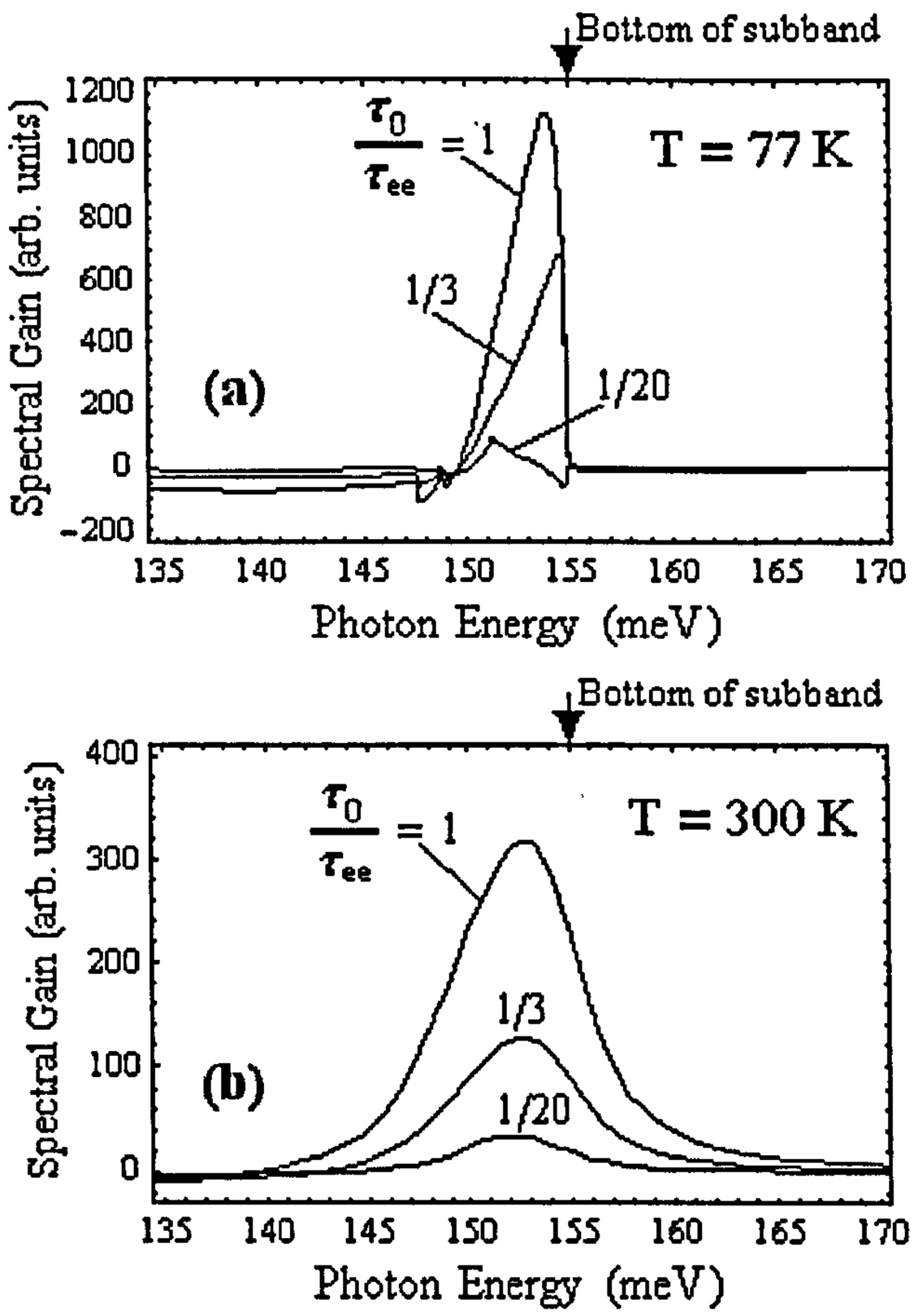

Figure 4.8 Variations of gain spectra under the monochromatic pumping $P_2(y) = P_0\delta\left(y - \frac{1}{2}\right)$ into the upper subband E_2 with equal subband population $n_2 = n_1$; assuming the following parameters: $\tau_0 = 0.1\,\text{ps}$, $\tau_{12} = \tau_1 = 1\,\text{ps}$, the subband separation energy $\hbar\Omega_0 = 155\,\text{meV}$, and $m_2^* = 1.2m_1^*$, for different values of $\eta = \frac{1}{20}$, $\frac{1}{3}$ and 1 at different temperatures : **(a)** 77 K, and **(b)** 300 K.

The calculations have been done for an equal global population case ($n_1 = n_2$) that corresponds to $\tau_{12} = \tau_1$; *i.e.* $\frac{\xi_1}{\xi_2} = 1$. The results show that a strong positive gain for particular photon energies can be achieved. Small values of η which correspond to low electron concentrations gives proportionally smaller gain amplitudes. In addition, the shapes of the particular distribution functions involved affect the shapes of the spectral curves. At $\eta > \frac{1}{3}$ corresponding to $n_s > 1.28\times10^{11}\,\text{cm}^{-2}$, the main reason for positive gain is the leverage of f_2 above f_1 below LO phonon energy. The radiative photon energies

are from $\hbar\Omega_0 - \hbar\omega_0\left(\frac{m_2^*}{m_1^*} - 1\right)$ to $\hbar\Omega_0$. Smaller photon energies correspond to large kinetic energies in both subbands, and the optical gain becomes negative in this region. At room temperature $T = 300\,\mathrm{K}$ the maximum values of gain strongly decrease because the amplitude of the peak near the pumping energy decreases when temperature increases. At the E_1 subband, more electrons are above LO threshold than electrons below the LO threshold. Furthermore, the transverse phase relaxation rate $\gamma(\varepsilon)$ becomes substantially larger thus smearing out the fine structure of the spectral gain function at smaller η.

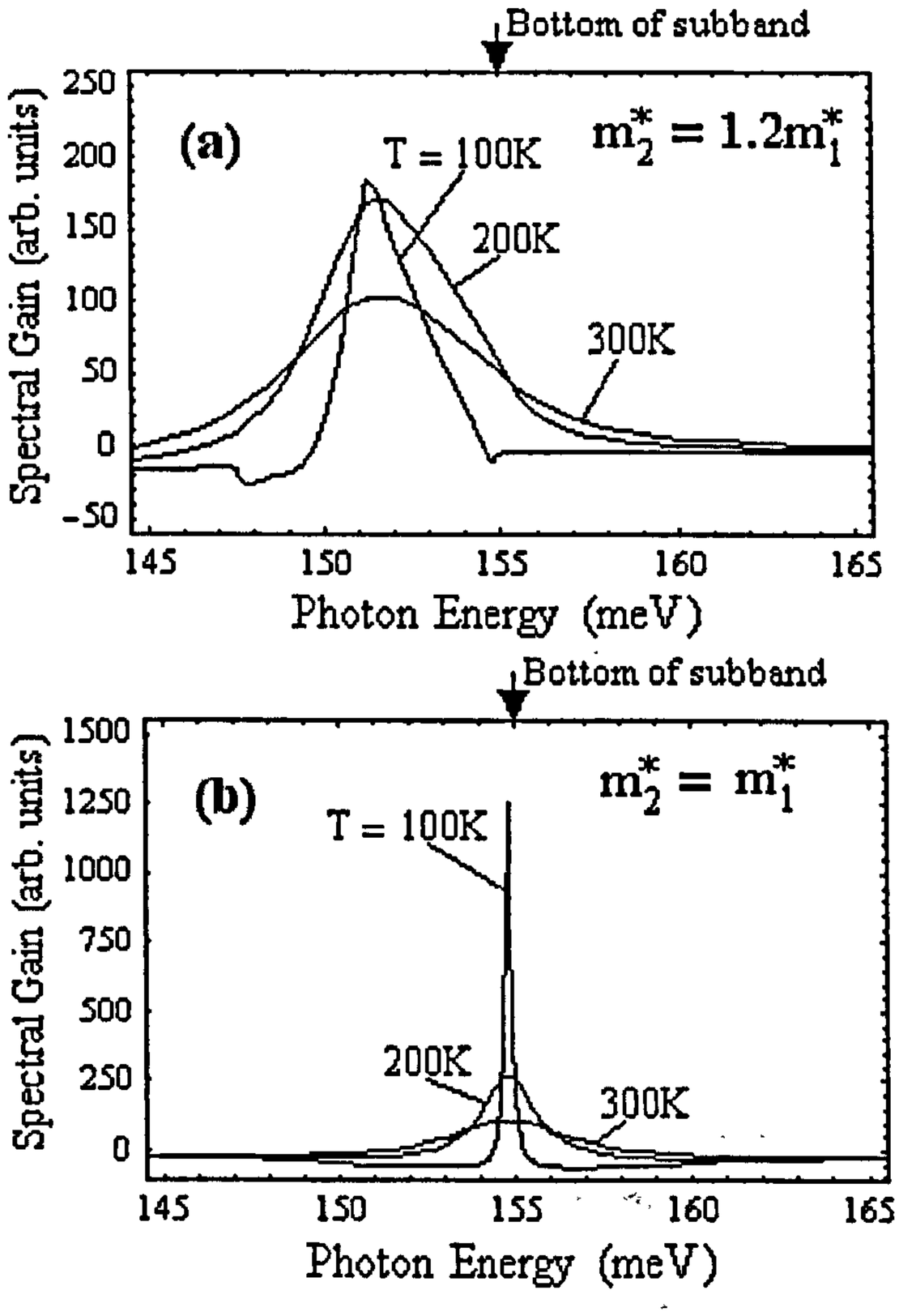

Figure 4.9 Gain spectra in low electron concentration limits at different operating temperatures under the pumping $P_2(y) = P_0\delta\left(y - \frac{1}{2}\right)$ into the upper subband E_2 with equal subband population $n_2 = n_1$. **(a)** Assuming the following parameters: $\tau_0 = 0.1\,\mathrm{ps}$, $\tau_{12} = \tau_1 = 1\,\mathrm{ps}$, $\tau_{ee} = 2\,\mathrm{ps}$, the subband separation energy $\hbar\Omega_0 = 155\,\mathrm{meV}$, and $m_2^* = 1.2m_1^*$. **(b)** Same spectra calculated in the parabolic model, $m_2^* = m_1^*$.

Figure 4.9 presents gain spectra calculated in the low electron concentration limit, $\eta = \frac{1}{20}$; *i.e.* $n_s = 1.92\times10^{10}\,\mathrm{cm}^{-2}$ at different temperatures T: 100 K, 200 K and 300 K. The results show that the peak gain is not strongly dependent upon temperature in the nonparabolic model while in the parabolic model it has strong temperature dependence, especially when the system is operated at low temperature. A reason for this is that the nonparabolicity effect smears out the peak gain. As a result, the peak gain is not strongly dependent upon temperature in the nonparabolic model

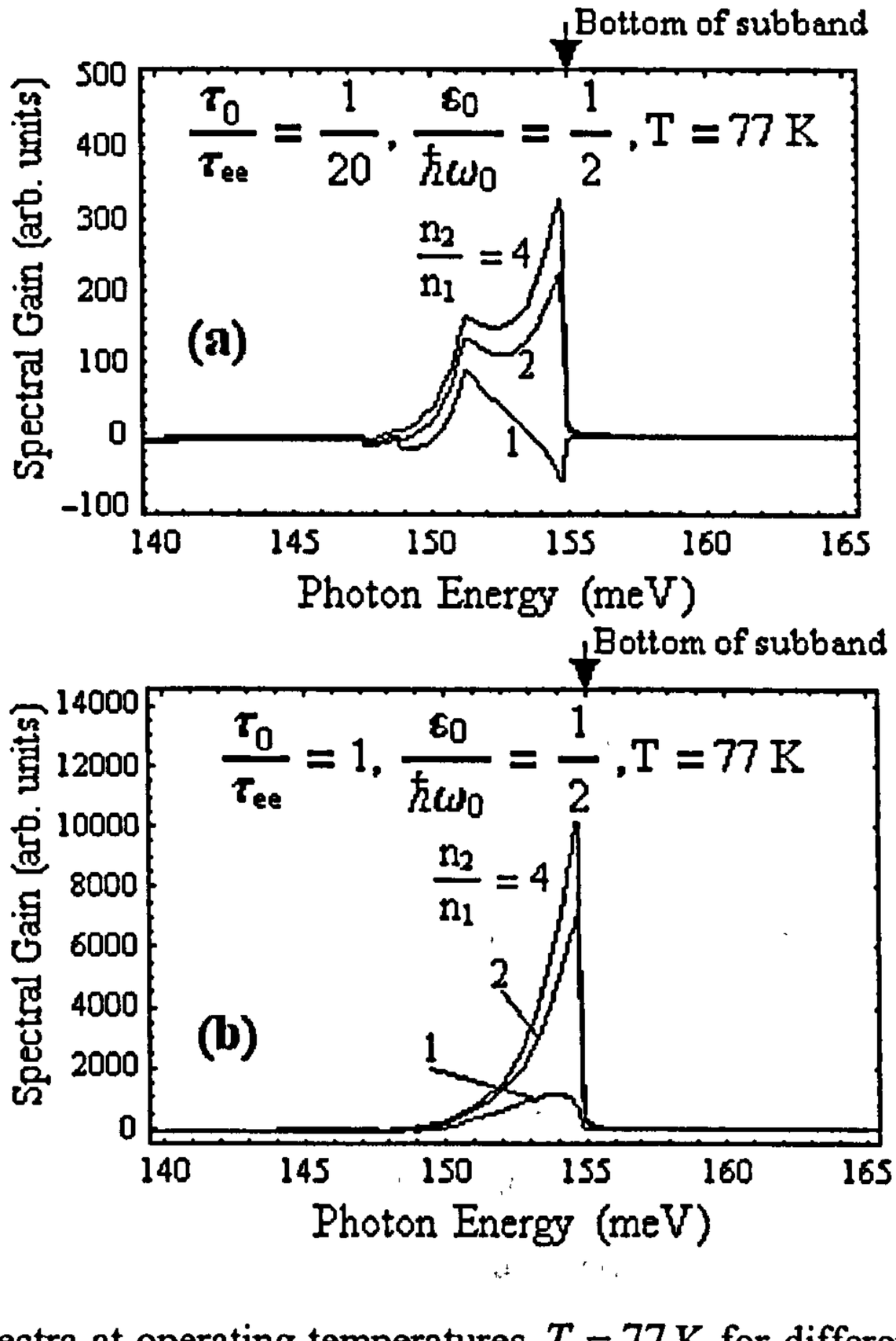

Figure 4.10 Gain spectra at operating temperatures $T = 77\,\mathrm{K}$ for different subband population ratios $\frac{n_2}{n_1} = 1,\ 2$ and 4 under the pumping $P_2(y) = P_0\delta\left(y - \frac{1}{2}\right)$ into the upper subband E_2 with equal subband population $n_2 = n_1$; assuming the following parameters: $\tau_0 = 0.1\,\mathrm{ps}$, the subband separation energy $\hbar\Omega_0 = 155\,\mathrm{meV}$, and $m_2^* = 1.2m_1^*$ at low and high electron-concentration regimes of operation which correspond to **(a)** $\eta = \frac{1}{20}$ and **(b)** $\eta = 1$, respectively.

In Figure 4.10, the gain spectra calculated for different values of $\frac{\xi_1}{\xi_2}=1,\ 2$ and 4 that correspond to global inversion population $\frac{n_2}{n_1}=1,\ 2$ and 4, respectively, are also investigated at low and high electron concentration regimes of operation. Our results show that the spectral density of gain is mainly sensitive to the upper subband distribution function $f_2(\varepsilon)$. For $n_2 > n_1$ at the low electron concentration regime, $\eta=\frac{1}{20}$ for instance (see Figure 4.10(a)), two peaks are observed. The first peak corresponds to the photon emission from the bottom of the E_2 subband, and second peak from the optical transitions near the initial pumping energy. At the high electron concentration regime, $\eta=1$ for instance (see Figure 4.10(b)), the second peak completely vanishes due to the dominant of e-e scattering.

4.5 Conclusions

The kinetic equations, Eqs.(4.41)-(4.44), has been solved analytically for subband distribution functions for various values of η ranging from 0.05 to 2, corresponding to electron concentrations n_s between $1.92\times10^{10}\,\mathrm{cm}^{-2}$ and $7.68\times10^{11}\,\mathrm{cm}^{-2}$. At small η the shapes of the distribution functions in both subbands deviate strongly from a Maxwellian. In the upper subband they have a pronounced peak at the pumping energy affected by the monochromatic electron generation process that plays an essential role in this regime of operation. Immediately after nonradiative intersubband transitions from the upper subband E_2 down to the lower subband E_1, the lower subband electrons are at high kinetic energy states $\varepsilon_1=\hbar\Omega_0+\varepsilon_2\pm\hbar\omega_0$. Consequently, they cascade down to the subband bottom by emitting LO phonons resulting in a strongly nonequilibrium distribu-tion function $f_1(\varepsilon_1)$ under steady-state conditions. At larger η all peaks are completely smeared out, and these distribution functions become close to a Maxwellian. Detailed shapes of these distribution functions are essential for the derivation of energy balance equation and calculation of gain in the intersubband lasers.

Our approach has an advantage of that it is more convenient to build up a model to investigate the kinetics of electron scattering in other similar systems by changing the relevant controlled parameters. However, in fact, there are some limitations of this model. For real device modeling one should take into account the following effects:

(i) All temperatures T_e, T_L and LO-phonon temperature T_{ph} are assumed to be the same for all cases considered in this present work. However, in real devices they might be different in some particular regimes of operation. For accurate calculations one has to evaluate T_e from the energy balance equation. The incoming energy depends on the electron generation G_0 while the energy losses depend on both distribution functions f_1 and f_2. The resulting equation gives Λ_{ee} as a function of η, ξ_1 and ξ_2. Also, at high electron concentrations LO phonon distribution function differs from N_0. Nevertheless, in our equations it requires only $N(\hbar\omega_0)$, and this can be described by using the effective LO-phonon temperature T_{ph} which differs from T_L. The effective temperature T_{ph} depends on the generation rates G_0 and the dissipation rates of phonons from the QW region.

(ii) In our approach A_{ee} is a constant over the whole energy range. In fact, this assumption works well only for $\varepsilon >> k_B T_e$ while at $\varepsilon \approx k_B T_e$, A_{ee} becomes smaller, and has the kinetic energy dependence. However, if electron distributions are Maxwellian or Fermi the particular value of A_{ee} is not important because there is no of LO phonon involvement in this region. Also at high kinetic energies e-e screening reduces A_{ee} down to several times of the value at low kinetic energies and high electron concentrations.

(iii) At very high electron concentrations corresponding to $\eta >> 1$, A_{ee} becomes sensitive to the exact distribution functions. As a result, it reduces the accuracy of our calculations if the assumption that A_{ee} is constant in these regimes of operation is used. However, our main interest is directed to investigate the system at

$\eta \leq 1$ where A_{ee} is not very sensitive to the exact shapes of these distribution functions.

(iv) The assumption that the dominant e-e scattering processes of the minority of high-kinetic energy electrons is only due to the scattering on the majority of quasi-thermalized electrons, in general, is not valid if the distribution function differs from a Maxwellian. However, in reality $k_B T_e << \hbar\omega_0$. As a result, $\exp\left(-\frac{\hbar\omega_0}{k_B T_e}\right) << 1$, thus fulfilling our approach which takes A_{ee} as a kinetic energy independent parameter.

(v) At the very low electron concentration regimes corresponding $\eta << 1$, the ratio $\frac{D_{ee}}{A_{ee}} = k_B T_e$ is not valid due to the difficulty of electrons to form a thermalized bath. In this case one has to calculate D_{ee} independently and use the resulting $T_e = \frac{D_{ee}}{k_B A_{ee}}$ as the definition of electron temperature.

(vi) The Fökker-Planck-Landau (FPL) approximation does not work well in the regions $|\varepsilon - \varepsilon_0| << k_B T_e$. The reason is that for 2DEG all scattering angles are equally important for energy transfer. To take all of these events into account one has to consider the integral equation, Eq.(4.26) instead of Eqs.(4.41)-(4.44). However, the resulting gain is not very sensitive to the exact shapes of the distribution functions near pumping point. In reality, the pumping is not an exact δ – function shape due to nonhomogeneous broadening.

Chapter 5

Charge accumulation in a triple barrier resonant tunneling structure

5.1 Introduction

Recently, there has been experimental interest in the effects of magnetic field on resonant tunneling in a triple barrier resonant tunneling structure (TBRTS) (shown schematically in Figure 5.1). Detailed measurements of the tunneling current in the TBRTS incorporating asymmetric coupled wells in the presence of a magnetic field applied perpendicular to the direction of current flow has been presented [107]. Experimental data shows that the current-voltage (I-V) characteristic has a sharp local minimum in its second derivative when the ground state levels in the wells (E_1 and E_1^*) are in resonant alignment. The depth of this minimum decreases with the application of an in-plane magnetic field. To explain these phenomena the concept of sequential tunneling thought the structure is introduced. The model presented here is based on a two-level rate equation system that takes into account realistic scattering and tunneling times. The investigation focuses on the in-plane magnetic field dependence of electrons at the E_1 level in QW1 tunneling resonantly thoughout the second well (QW2). The theoretically calculated results are compared with experimental results reported by Vdovin *et al.* [107].

5.2 Effect of magnetic field on resonant tunneling in a triple barrier resonant tunneling structure

5.2.1 Effect of magnetic field on the energy of bound states in the quantum wells

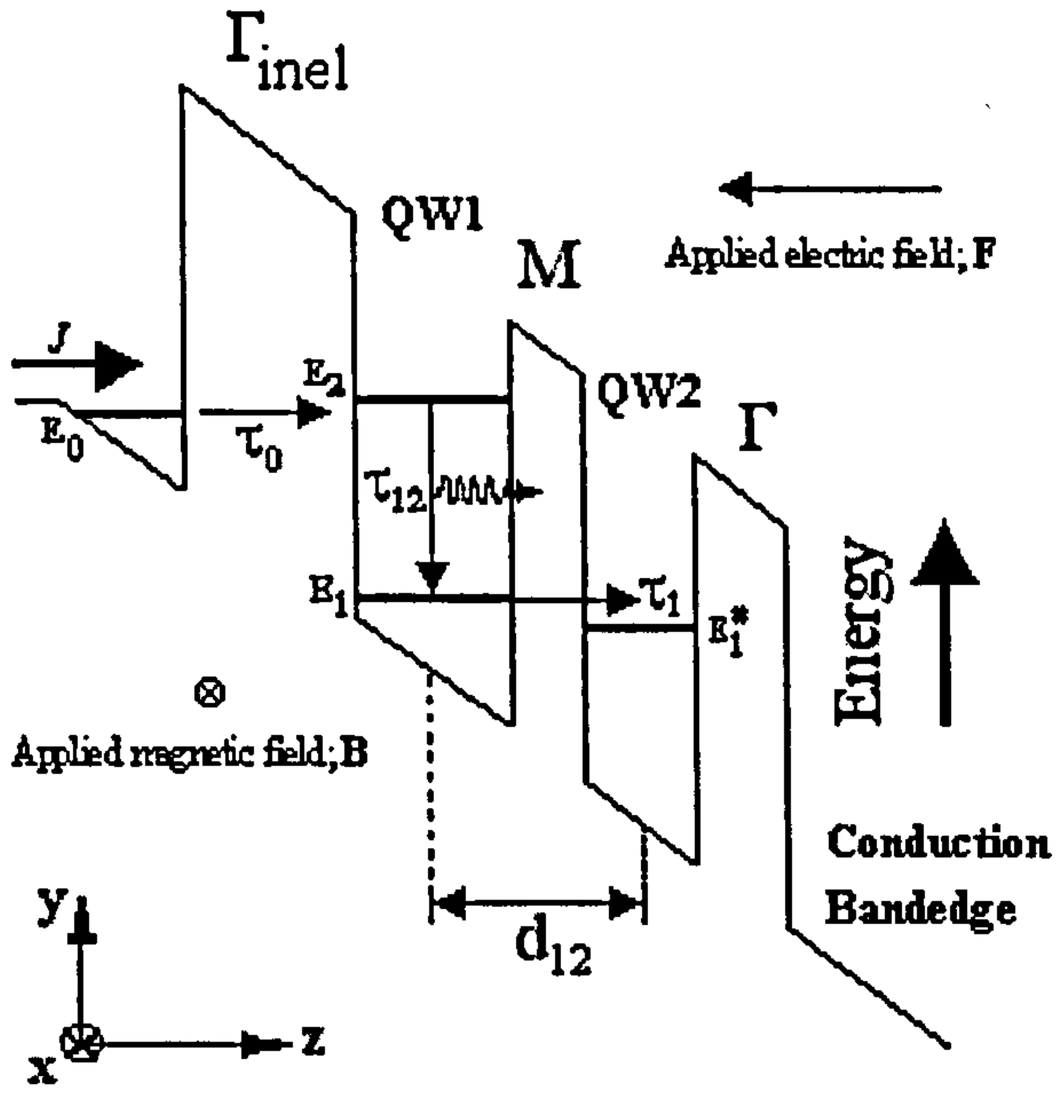

Figure 5.1 Schematic diagram of the conduction bandedge of a TBRTS in the presence of an applied electric Field, $\vec{F} = -F\hat{e}_z$ and a magnetic field, $\vec{B} = B\hat{e}_x$, and also shown are the kinetics of electron transport through the structure.

In the presence of a magnetic field $\vec{B} = B\hat{e}_x$ the electrons states in each of the wells when isolated from each other can be described by a single-particle Hamiltonian,

$$\hat{H}_0 = \frac{\left(\vec{p} - e\vec{A}\right)^2}{2m^*} + U(z) , \qquad (5.1)$$

where $\vec{p}$ is the linear momentum of the electron, and $\vec{A}$ the vector potential for a uniform magnetic field $\vec{B} = B\hat{e}_x$, namely, $\vec{A} = -Bz\,\hat{e}_y$. m^* is the electron effective mass. The potential energy $U(z)$ includes the electrostatic potential and conduction bandedge discontinuity. Thus, $U(z) = E_c(z) - eFz$; where $E_c(z)$ is the conduction bandedge discontinuity, and F is the magnitude of applied electric field.

Consequently, the time-independent Schrödinger-like equations for the bound states can be obtained

$$\left[\frac{\left(\vec{p}-e\vec{A}\right)^2}{2m^*} + U(z)\right]\Psi(\vec{r}) = E\Psi(\vec{r}) \ , \tag{5.2}$$

where $\Psi_{n,k_{xy}}(\vec{r})$ is the electron wavefunction that can be written in the form

$$\Psi_{n,k_{xy}}(\vec{r}) = \frac{1}{\sqrt{S}}\exp\left(i\vec{k}_{xy}\cdot\vec{r}\right)\varphi_n(z) \ , \tag{5.3}$$

and the total energy

$$E_n\left(k_{xy}\right) = \frac{\hbar^2 k_{xy}^2}{2m^*} + \varepsilon_n \ , \tag{5.4}$$

where $\vec{k}_{xy} = k_x\hat{e}_x + k_y\hat{e}_y$ is the in-plane electron wave vector, S the normalization area of the QW plane, and $\varphi_n(z)$ are the envelope functions of the isolated well centred at $-\frac{L_1}{2}-\frac{b}{2}$ for QW1 ($\frac{L_2}{2}+\frac{b}{2}$ for QW2), that satisfies the Schrödinger-like equation

$$\left[\left(-\frac{\hbar^2}{2m^*}\frac{d^2}{dz^2} + U(z)\right) + \omega_c p_y z + \frac{m^*}{2}\omega_c^2 z^2\right]\varphi_n(z) = \varepsilon_n\varphi_n(z) \ , \tag{5.5}$$

where $p_y = \hbar k_y \equiv$ the momentum of electrons in y direction, and $\omega_c = \frac{eB}{m^*} \equiv$ the cyclotron frequency. The term $\frac{m^*}{2}\omega_c^2 z^2$ for magnetic fields: $B \le 4\,\mathrm{T}$, thoughout the experimental measurement [107] is much smaller than other terms, and is neglected in the following calculations.

The finite barrier thickness in the TBRTS permits electron tunneling; *i.e.* electrons have the possibility to tunnel through the barriers. As a result, the states E_1, E_2 (in QW1) and E_1^* (in QW2) are no longer stable. For instance, electrons in E_1 in QW1 can tunnel throughout the second well and subsequently decay to the continuum states.

The behaviour of such a system is well described by a time-dependent Schrödinger-. type equation [85, 86],

$$i\hbar\frac{d}{dt}\begin{pmatrix}\psi_1(t)\\ \psi_2(t)\end{pmatrix} = \begin{pmatrix}E_1 & -M\\ -M & E_1^* + \omega_c d_{12} p_y + i\Gamma\end{pmatrix}\times\begin{pmatrix}\psi_1(t)\\ \psi_2(t)\end{pmatrix} = E'\begin{pmatrix}\psi_1(t)\\ \psi_2(t)\end{pmatrix}, \quad (5.6)$$

where $|\psi_1(t)|^2$ is the probability of finding the electron at the E_1 level in QW1, and $|\psi_1(t)|^2$ - at the E_1^* level in the second well (QW2). M is the magnitude of the matrix element of the transition due to the tunneling between QW1 and QW2, Γ the half width of the E_1^* level, and d_{12} is the distance between the centres of QW1 and QW2. The quasi-stationary levels E' are obtained from the secular equation [15, 86],

$$\det\begin{pmatrix}E'-E_1 & M\\ M & E'-E_1^*-\omega_c d_{12} p_y - i\Gamma\end{pmatrix} = 0, \quad (5.7)$$

Thus,

$$E' = E^{(\pm)} = \left(\frac{E_1 - \tilde{E}_1^* - i\Gamma}{2}\right) \pm \sqrt{\left(\frac{E_1 - \tilde{E}_1^* + i\Gamma}{2}\right)^2 + M^2}, \quad (5.8)$$

where $\tilde{E}_1^* = E_1^* + \omega_c d_{12} p_y$. The levels $E^{(+)}$ and $E^{(-)}$ correspond to the antisymmetric and symmetric wave functions, respectively. Notice that the notations E_1, E_2 and E_1^* throughout our approach stand for the bound states in each of the wells in the absence of applied magnetic field, when isolated from each other.

For the degenerate case ($E_1 = \tilde{E}_1^*$), one has a peculiar physical behaviour resulting from an interplay of the coherent tunneling between two wells, and a tunneling from QW2 to the continuum. It is found that if $2M > \Gamma$ then

$$E^{(\pm)} = \left(E_1 \pm \frac{1}{2}\sqrt{4M^2 - \Gamma^2}\right) - i\frac{\Gamma}{2}. \quad (5.9)$$

This implies that the system has two different levels with the same width, $\frac{\Gamma}{2}$. In the opposite case, $2M < \Gamma$, and therefore,

$$E^{(\pm)} = E_1 - \frac{i}{2}\left(\Gamma \pm \sqrt{\Gamma^2 - 4M^2}\right), \tag{5.10}$$

the system has the same energy level with two different widths.

However, in our system the condition $2M > \Gamma$ is always fulfilled. As a result, the considered system always has two split energy levels with the same width for the degenerate case ($E_1 = \widetilde{E}_1^*$). The escape rate $\frac{1}{\tau_1}$ from QW1 has the magnetic field and in-plane momentum dependence,

$$\frac{1}{\tau_1} = -\frac{1}{\hbar}\begin{cases}\mathrm{Im}\,E^{(-)} & ; \; E_1 < E_1^* \\ \mathrm{Im}\,E^{(+)} & ; \; E_1 > E_1^*\end{cases} \cong \frac{\Gamma}{2\hbar}\left(1 - \frac{1}{\sqrt{1+\dfrac{4M^2-\Gamma^2}{\left(E_1 - E_1^* - \omega_c d_{12} p_y\right)^2}}}\right), \tag{5.11}$$

In order to calculate the average escape rate $\left\langle \frac{1}{\tau_1} \right\rangle$, using Eq.(5.11) knowledge of the distribution function of electrons in the E_1 level is required. Thus, the average rate $\left\langle \frac{1}{\tau_1} \right\rangle$ of electrons tunneling resonantly throughout the second well (QW2) is given by

$$\left\langle \frac{1}{\tau_1} \right\rangle = \int_{-\infty}^{+\infty}\int_{-\infty}^{+\infty} f_1(p_x, p_y)\frac{\Gamma}{2\hbar}\left(1 - \frac{1}{\sqrt{1+\dfrac{4M^2-\Gamma^2}{\left(E_1 - E_1^* - \omega_c d_{12} p_y\right)^2}}}\right) dp_x dp_y, \tag{5.12}$$

where $f_1(p_x, p_y)$ is a normalized distribution function of electrons in the E_1 level. Physically, this means that the magnetic fields applied parallel to the QW layers destroy the resonance condition, and result in resonance broadening $\Delta E_{res} = \omega_c d_{12} p_y$.

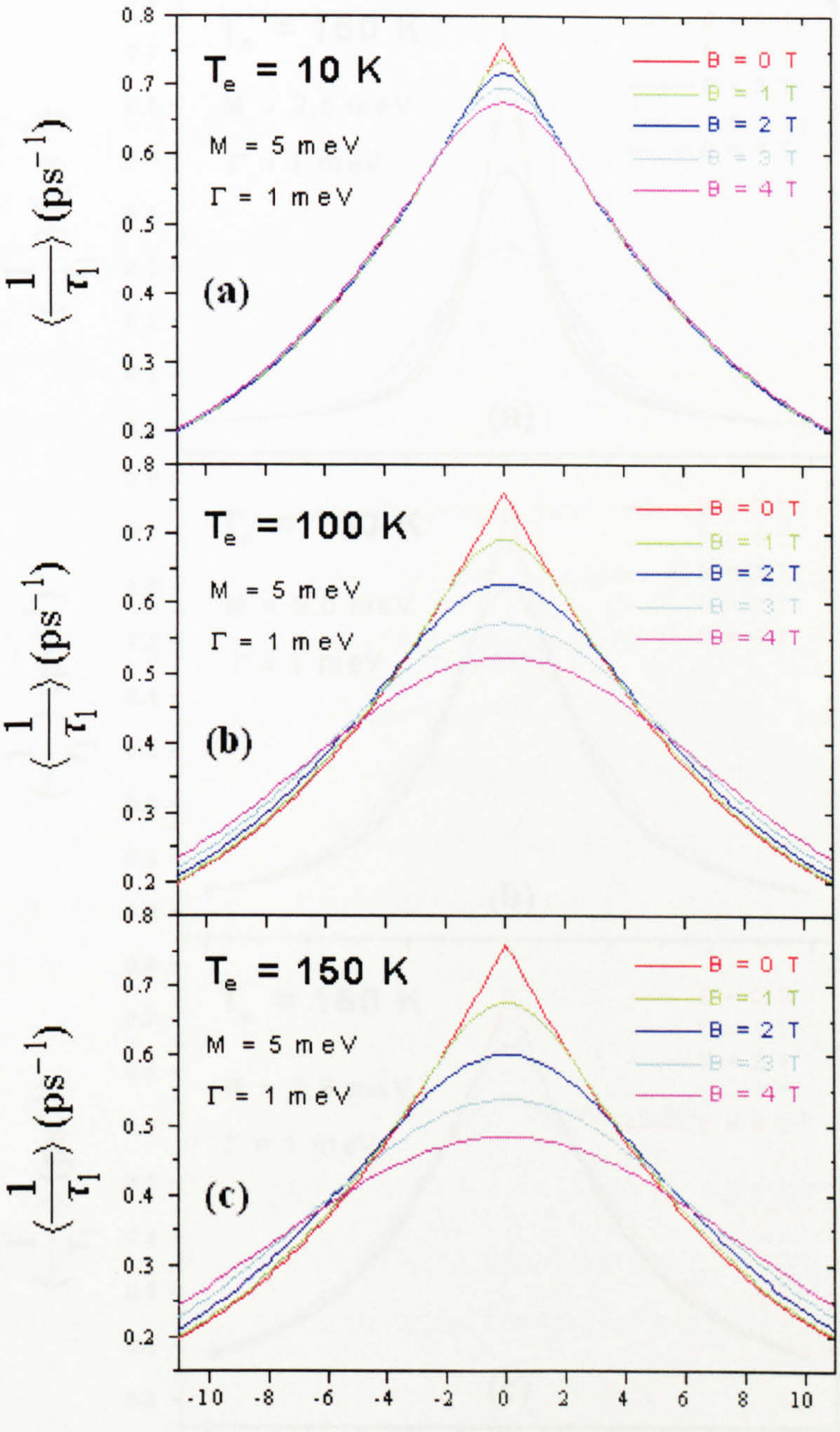

Figure 5.2 Average escape rates of electron tunneling resonantly throughout the second well (QW2) as a function of energy difference $E_1 - E_1^*$ at different in-plane applied magnetic fields : 0 T, 1 T, 2 T, 3 T and 4 T, for $M = 5\,\text{meV}$ and $\Gamma = 1\,\text{meV}$; assuming electron temperature T_e : **(a)** 10 K, **(b)** 100 K, and **(c)** 150 K.

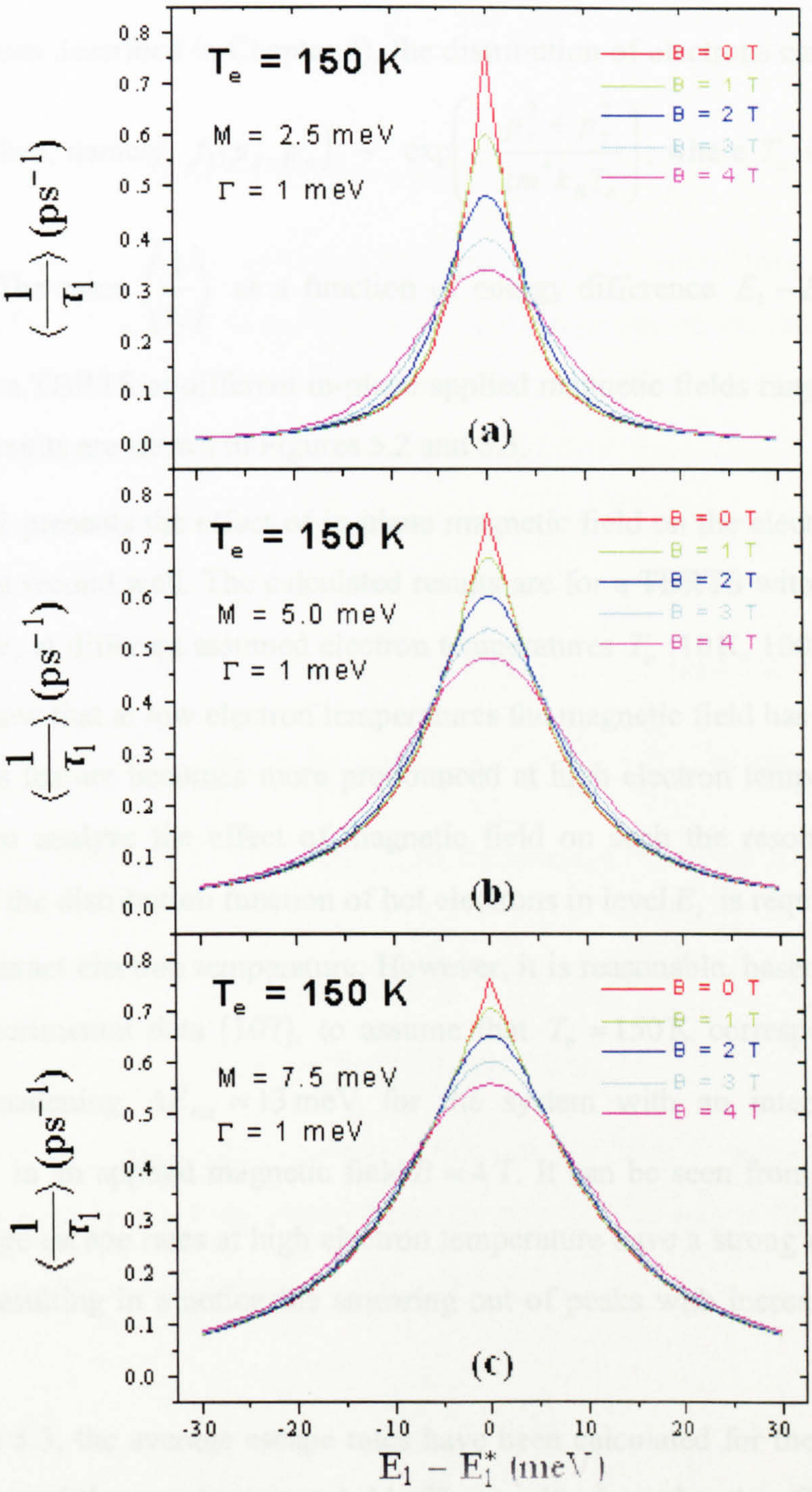

Figure 5.3 Average escape rates of electron tunneling resonantly throughout the second well (QW2) as a function of the energy difference $E_1 - E_1^*$ at different in-plane applied magnetic fields: 0 T, 1 T, 2 T, 3 T and 4 T, for $\Gamma = 1$ meV and different values of M : (**a**) 2.5 meV, (**b**) 5.0 meV, and (**c**) 7.5 meV; assuming electron temperature $T_e = 150$ K.

In general, for a system at electron concentrations $n_s \approx 1.0\times10^{11}$ cm^{-2} (more details have been described in Chapter 4), the distribution of electrons can be assumed to be Maxwellian, namely, $f_1(p_x, p_y) \sim \exp\left(-\frac{p_x^2 + p_y^2}{2m^* k_B T_e}\right)$; where T_e is the electron temperature. The rates $\left\langle \frac{1}{\tau_1} \right\rangle$ as a function of energy difference $E_1 - E_1^*$ have been calculated for a TBRTS at different in-plane applied magnetic fields ranging from 0 T to 4 T . The results are shown in Figures 5.2 and 5.3.

Figure 5.2 presents the effect of in-plane magnetic field on the electron tunneling throughout the second well. The calculated results are for a TBRTS with $M = 5$ meV and $\Gamma = 1$ meV, at different assumed electron temperatures T_e : 10 K, 100 K and 150 K. The results show that at low electron temperatures the magnetic field has less effect on the rates. This feature becomes more pronounced at high electron temperatures. This implies that to analyze the effect of magnetic field on such the resonant tunneling knowledge of the distribution function of hot electrons in level E_1 is required, allowing us to find an exact electron temperature. However, it is reasonable, based on a comparison wit experimental data [107], to assume that $T_e = 150$ K corresponding to the resonance broadening $\Delta E_{res} \approx 13$ meV for the system with an interwell distance $d_{12} = 75.5$ Å in an applied magnetic field $B = 4$ T. It can be seen from Figure 5.2(c) that the average escape rates at high electron temperature have a strong magnetic field dependence resulting in a noticeable smearing out of peaks with increasing magnetic field.

In Figure 5.3, the average escape rates have been calculated for the TBRTS with differing values of the transfer integral M . The results show that the effect of applied magnetic fields on the resonant tunneling is strongly dependent on M . Smearing of the peaks becomes noticeable when M decreases. In other words, the resonance condition of electrons tunneling throughout the second well is easily destroyed by an applied magnetic field in a weakly coupled well system. For the structure described in Ref.107

with well widths QW1 66 Å/QW2 33 Å and the middle barrier thickness 26 Å, the calculated M and Γ are approximately 5 meV and 1 meV, respectively.

5.2.2 Current-voltage characteristic and its derivatives

To investigate the current-voltage (I-V) characteristic obtained from the struc-ture shown in Figure 5.1, and its derivatives we use the concept of sequential tunneling, when electrons first accumulate at emitter level E_0 and tunnel to E_2, then after LO phonon emission drop to level E_1, and finally leave QW1. The design of the structure is chosen in such a way that tunneling from level E_1 to the collector is always faster than tunneling from E_0 to QW1. Moreover, the tunneling from QW1 is sufficiently fast when levels E_1 and E_1^* approximately coincide. The total current density J through the heterostructure obeys the equations $J = \frac{Q_0}{\tau_0} = \frac{Q_1}{\bar{\tau}_1}$, where τ_0 is the tunneling time from level E_0 to QW1 and $\bar{\tau}_1$ is the average of escape times from QW1 throughout QW2, namely, $\bar{\tau}_1 = \left\langle \frac{1}{\tau_1} \right\rangle^{-1}$, Q_0 the sheet charge density at level E_0, and Q_1 the sheet charge density in the wells (QW1 and QW2).

To simplify the model one can assume that the total bias V across the device is mainly determined by the total sheet charge density $Q = Q_0 + Q_1 \equiv Q(V)$. Therefore, the I-V characteristics can be obtained in the form [107]

$$J = \frac{Q}{\tau_0 + \bar{\tau}_1} \quad . \tag{5.13}$$

This leads us to obtain the differential conductivity $\frac{\partial J}{\partial V}$ and its derivative

$$\frac{\partial J}{\partial V} = \frac{1}{\tau_0 + \bar{\tau}_1}\frac{dQ}{dV} - \frac{Q}{(\tau_0 + \bar{\tau}_1)^2}\left[\frac{d\tau_0}{dV} + \frac{d\bar{\tau}_1}{dV}\right] \quad , \tag{5.14}$$

$$\frac{\partial^2 J}{\partial V^2} = \frac{2Q\left(\frac{d\tau_0}{dV}+\frac{d\bar{\tau}_1}{dV}\right)}{\left(\tau_0+\bar{\tau}_1\right)^2}\left[\frac{\left(\frac{d\tau_0}{dV}+\frac{d\bar{\tau}_1}{dV}\right)}{\tau_0+\bar{\tau}_1} - \frac{1}{2}\frac{\left(\frac{d^2\tau_0}{dV^2}+\frac{d^2\bar{\tau}_1}{dV^2}\right)}{\frac{d\tau_0}{dV}+\frac{d\bar{\tau}_1}{dV}} - \frac{1}{Q}\frac{dQ}{dV}\right], \quad (5.15)$$

5.3 Calculations of the current-voltage characteristic and its derivatives

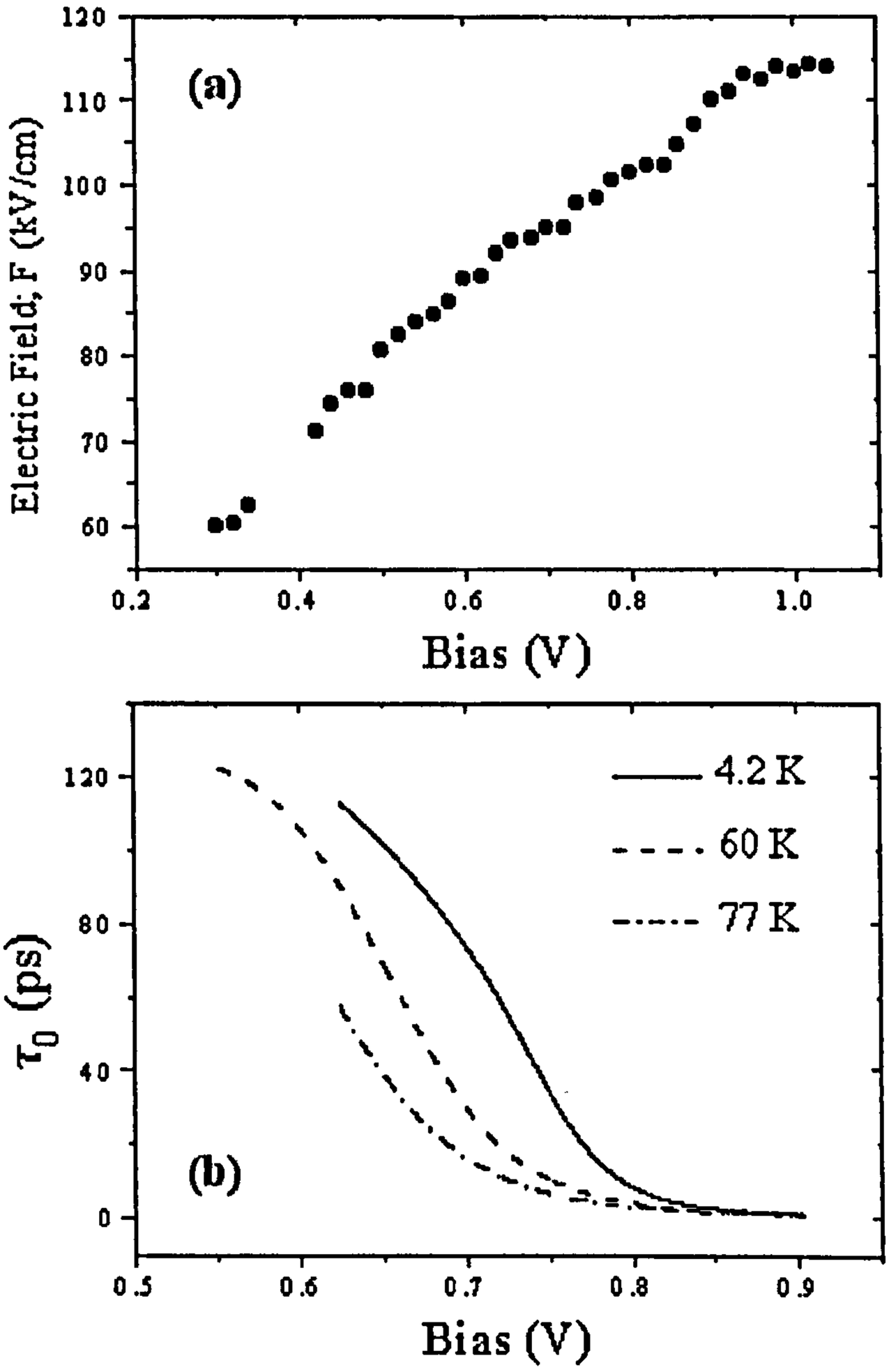

Figure 5.4 **(a)** Calibration of electric field against device bias [15]. **(b)** Experimental data of τ_0 against device bias at different operating temperatures T: 4.2 K, 60 K and 77 K [107].

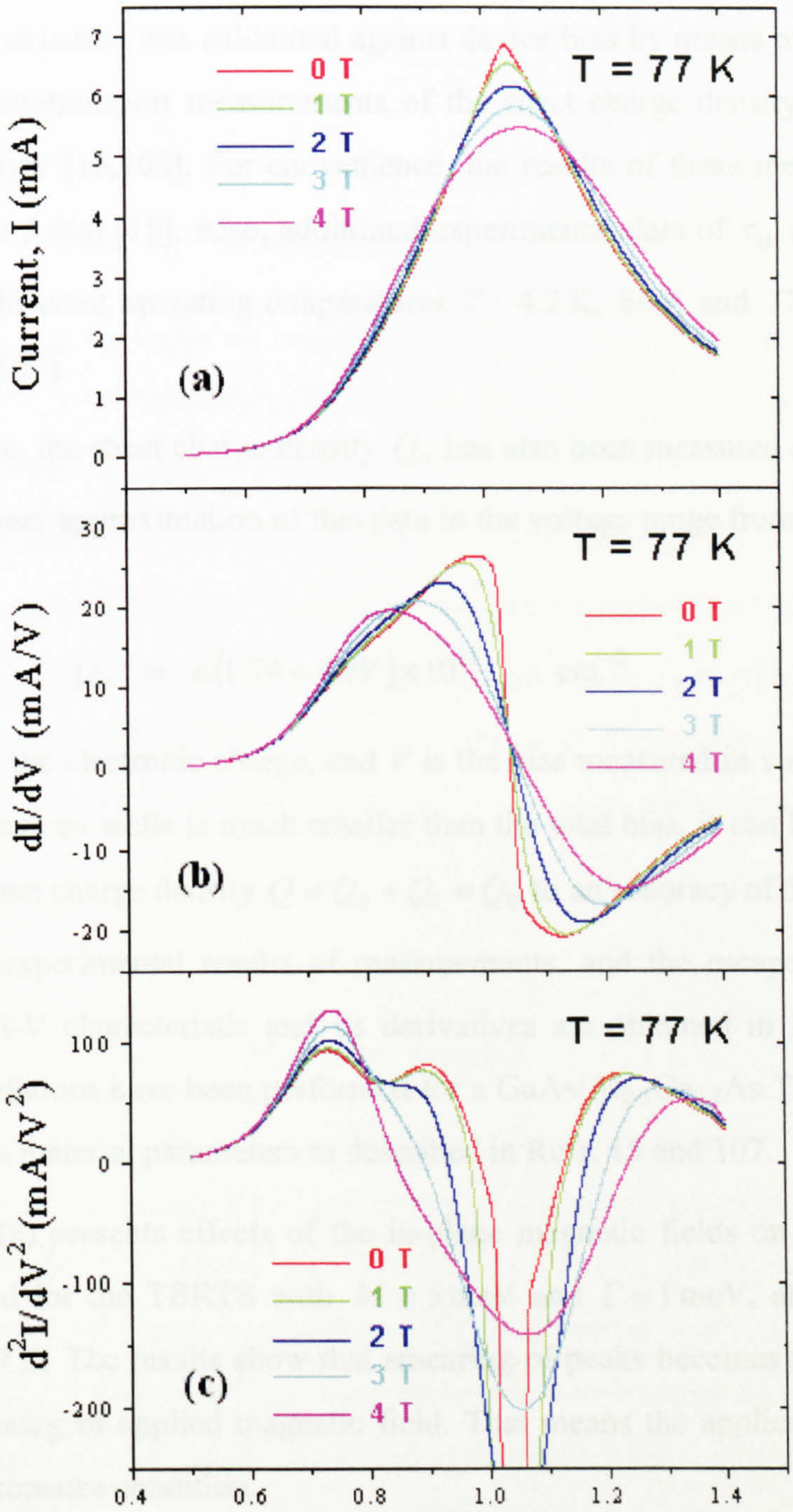

Figure 5.5 **(a)** Typical I-V characteristics, **(b)** the differential conductance ($\frac{dI}{dV}$), and **(c)** the second derivatives ($\frac{d^2I}{dV^2}$) of the I-V characteristics at different in-plane magnetic fields: 0 T, 1T, 2 T, 3 T and 4 T, at operating temperature $T = 77\,\mathrm{K}$; assuming $M = 5\,\mathrm{meV}$, $\Gamma = 1\,\mathrm{meV}$ and electron temperature $T_e = 150\,\mathrm{K}$.

In order to facilitate the device modelling given in Eqs.(5.12)-(5.15), the electric field within the structure was calibrated against device bias by means of Shubnikov-de Haas-like magnetotransport measurements of the sheet charge density in the emitter accumulation layer [15,108]. For convenience, the results of these measurements are shown in Figure 5.4(a) [15]. Also, additional experimental data of τ_0 as a function of device bias at different operating temperatures T: 4.2 K, 60 K and 77 K is shown in Figure 5.4 (b) [107].

Furthermore, the sheet charge density Q_0 has also been measured as a function of device bias. Linear approximation of this data in the voltage range from 0.6 V to 0.9 V gives [107]

$$Q_0 = e.(1.74 + 4.8V) \times 10^{11} \quad \text{cm}^{-2} \quad , \tag{5.16}$$

where e is the electronic charge, and V is the bias measured in volts. Because the voltage drop between wells is much smaller than the total bias, it can be assumed that that the total sheet charge density $Q = Q_0 + Q_1 \approx Q_0$ to an accuracy of 5% [107]. Using these relevant experimental results of measurements, and the escape rates given in Eq.(5.12), the I-V characteristic and its derivatives are obtained in Figure 5.5. The following calculations have been performed for a GaAs/$Al_{0.3}Ga_{0.7}As$ TBRTS shown in Figure 5.1, with material parameters as described in Refs. 15 and 107.

Figure 5.5(a) presents effects of the in-plane magnetic fields on the I-V characteristic obtained for the TBRTS with $M = 5$ meV and $\Gamma = 1$ meV, at operating temperature $T = 77$ K. The results show that smearing of peaks becomes more significant with the increasing of applied magnetic field. That means the applied magnetic field destroys the resonance condition.

Figure 5.5(b) shows the differential conductance $\frac{dI}{dV}$ as a function of bias-voltage at different applied magnetic fields. At the low-bias range (≤ 0.60 V), the differential conductance is extremely small. It rises at the onset of electron tunneling, and then drops sharply after exceeding a maximum; particularly for the system in the absence of the applied magnetic field ($B = 0$ T). This feature corresponds to a roughly triangular I-V curve. With increasing magnetic field the triangle I-V curve is smeared out that

results in a smooth drop of $\frac{dI}{dV}$ after reaches its maximum. As the bias is increased further, an instability of the device can be observed at the high bias (≥ 1.05 V); *i.e.* the negative differential conductance occurs.

Figure 5.5(c) shows the calculated curves of the second derivative $\frac{d^2I}{dV^2}$ versus bias voltage for different applied magnetic fields at operating temperature $T = 77$ K. The peak in the second derivative in the absence of applied magnetic field corresponds to alignment of the E_0 level of the emitter accumulation layer with the E_2 level of QW1. The local minimum can be described in terms of the rapid removal of electrons from the E_1 level of QW1 throughout the resonantly aligned level E_1^* in the QW2. This local minimum is located at bias-voltage around 0.83 V. The result agrees closely with the experimental data that gives bias-voltage at which maximum population inversion is observed [15]. In addition, it can be seen that magnetic field flattens the local minimum.

5.4 Comparison with experimental results

To compare theoretically calculated results with experiments, the TBRTS using in Ref. 107 has been considered. The most interesting structure having been investigated throughout this work has well widths QW1 66 Å/QW2 33 Å, and thickness of the first, second and third barriers are 66 Å, 26 Å and 26 Å, respectively. Experimental and theoretical results of typical I-V characteristics and their second derivatives obtained from this structure in the absence of an applied magnetic field at different temperatures T: 4.2 K and 77 K are presented in Figures 5.6 and 5.7.

In Figure 5.6 it can be seen that the theoretically calculated I-V curves agree well with experiments at the onset of tunneling in the bias-range 0.7 V- 0.9 V. At high bias (> 0.9 V) the current calculated by using our considered model is much smaller than that from experiments. This disagreement is probably from effective LO phonon emission taking place at the high-bias range, not taken into account in our calculations. In order to investigate the behaviour of electron tunneling through the heterostructure in

the high-bias regime, a good understanding of electron scattering processes occurring in this region is required.

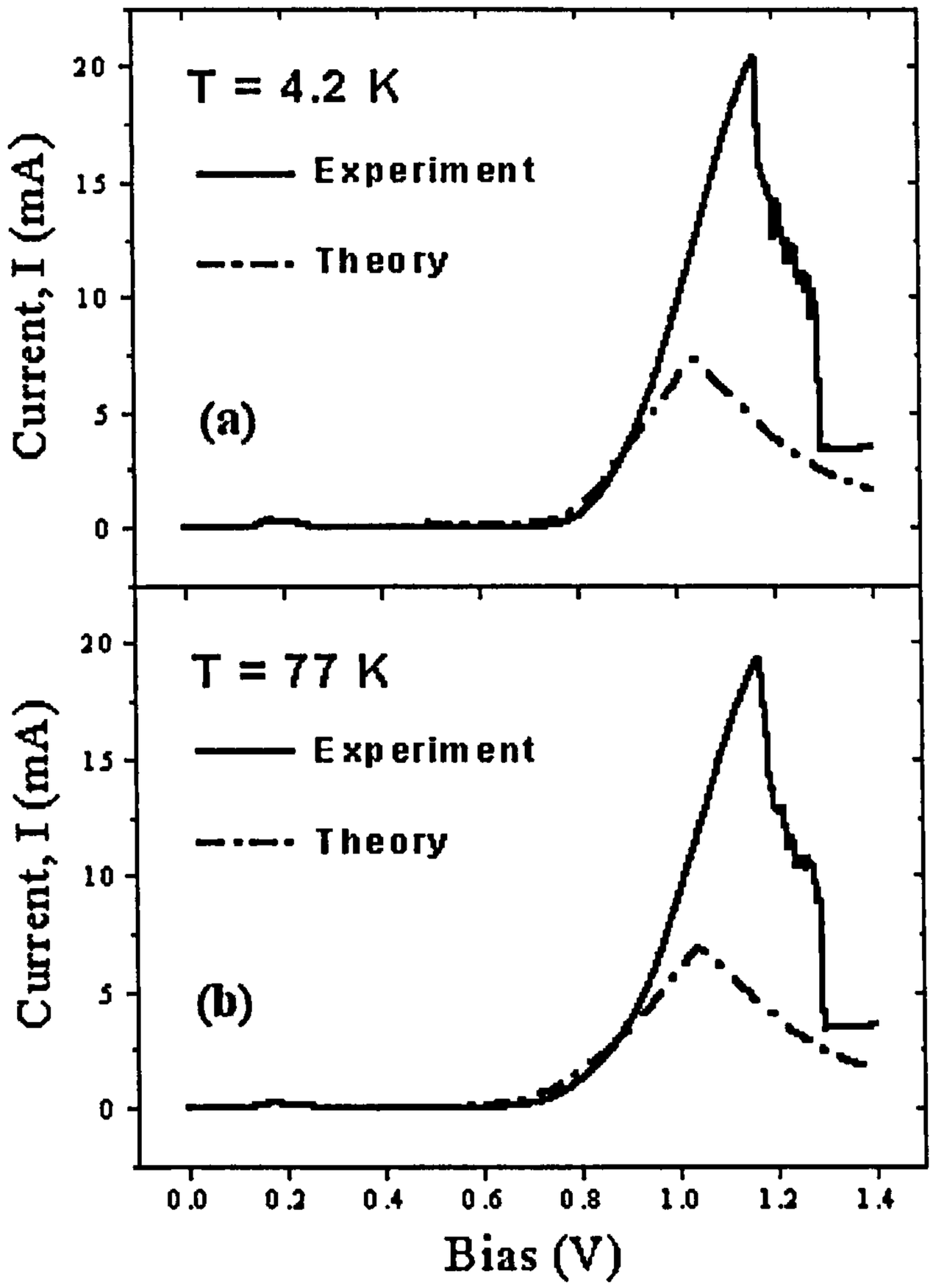

Figure 5.6 Typical I-V characteristics obtained from the TBRTS shown in Figure 5.1 in the absence of applied magnetic field at different operating temperature: **(a)** 4.2 K, and **(b)** 77 K. The solid lines (——) are experimental I-V characteristics of the device in forward bias [107]. The dash-dot lines (—·—·) are theoretically calculated results for a TBRTS with $M = 5\,\text{meV}$, $\Gamma = 1\,\text{meV}$; assuming electron temperature $T_e = 150\,\text{K}$.

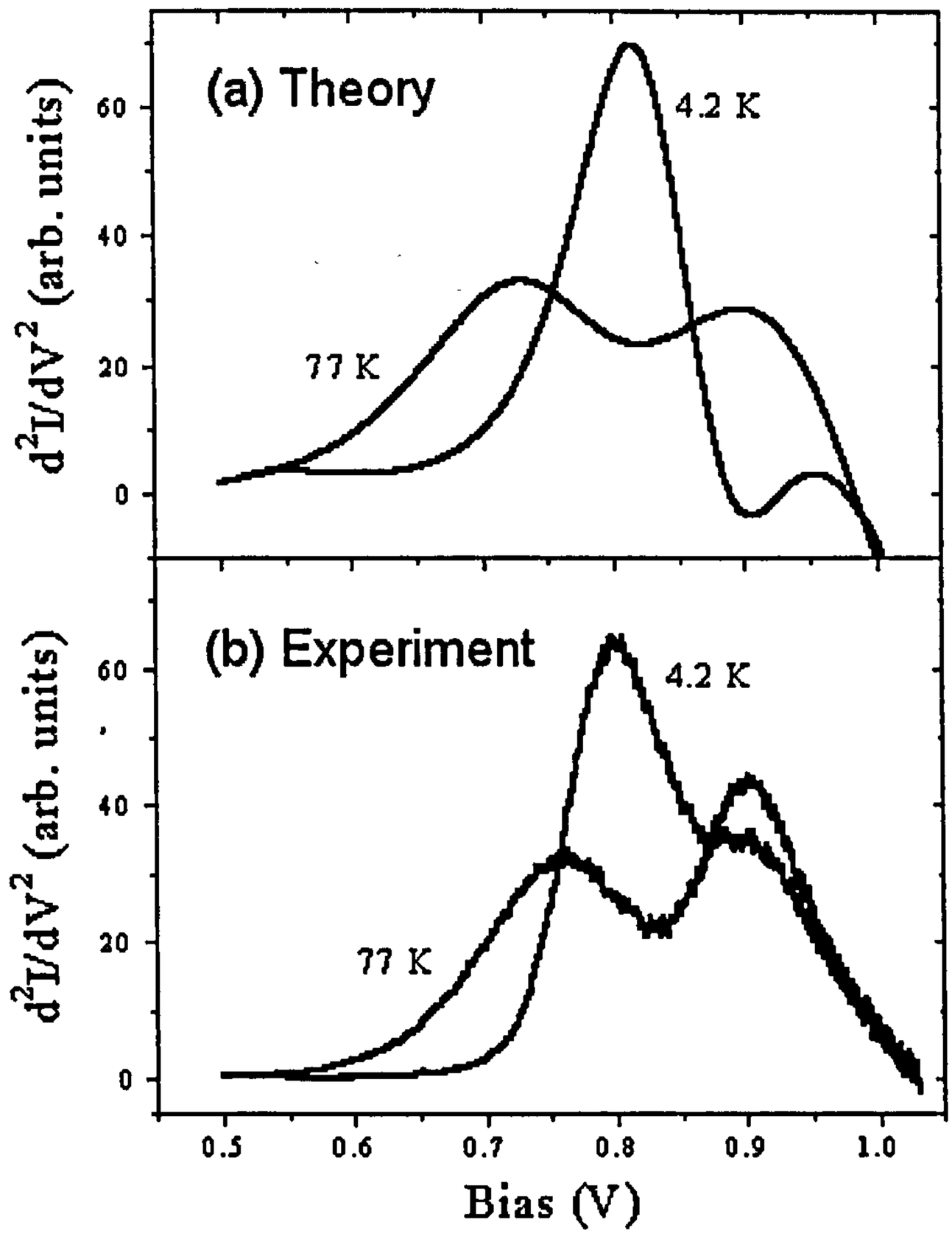

Figure 5.7 The second derivatives $\frac{d^2I}{dV^2}$ against bias in the absence of applied magnetic field at different operating temperatures T: 4.2 K and 77 K. **(a)** Theoretical results calculated for a TBRTS with $M = 5\,\text{meV}$, $\Gamma = 1\,\text{meV}$; assuming electron temperature $T_e = 150\,\text{K}$. **(b)** Experimental results reported by Vdovin, *et al.* [107].

Figure 5.7(a) shows the theoretically calculated curves of the second derivatives $\frac{d^2I}{dV^2}$ against bias in the absence of applied magnetic field at different temperatures T: 4.2 K and 77 K. At $T = 4.2\,\text{K}$ the second peak in the second derivative displays a clear splitting. This feature becomes more pronounced at $T = 77\,\text{K}$ and exhibits a sharp local minimum at 0.83 V. The results agree very well with the experimental data as shown in Figure 5.7(b).

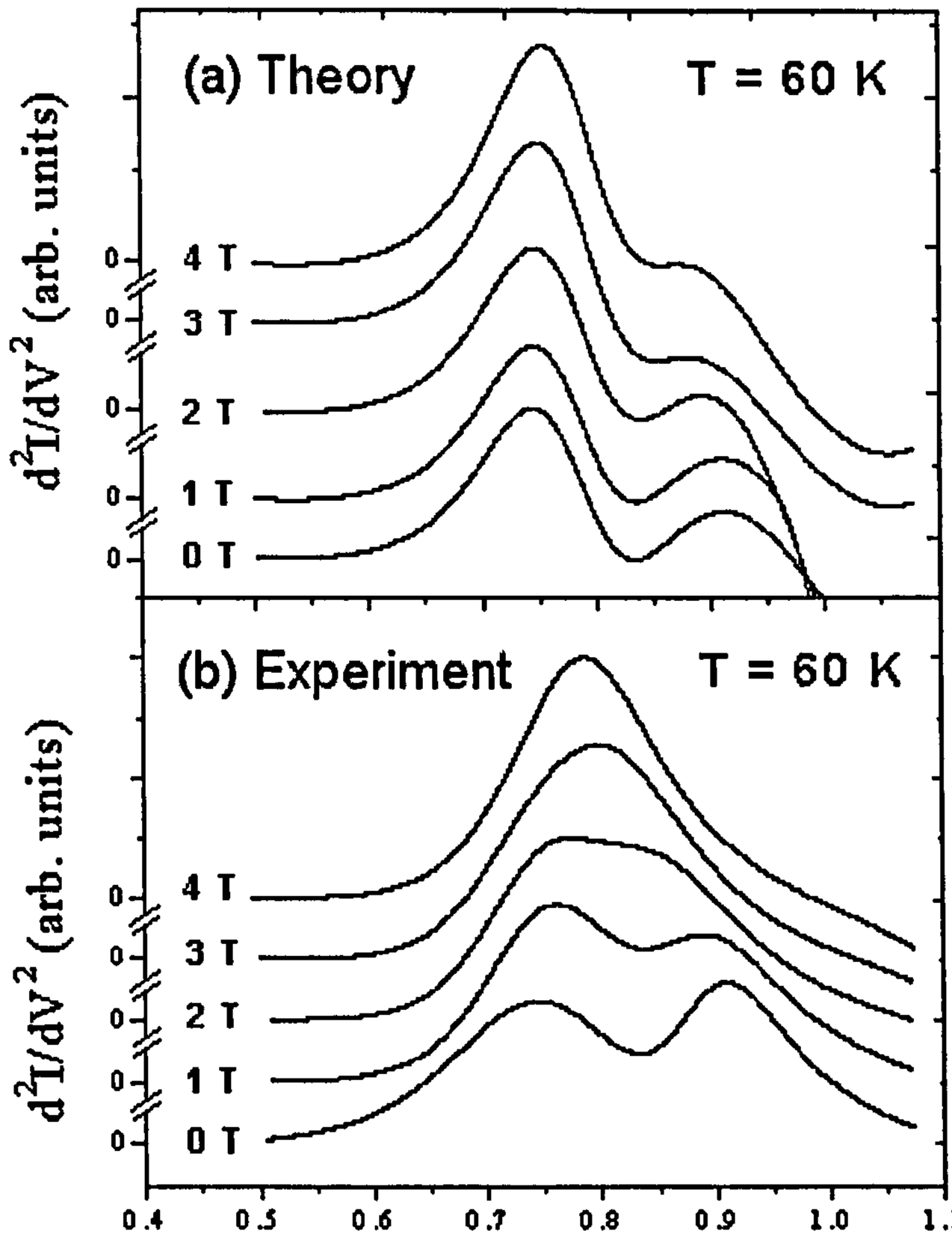

Figure 5.8 The second derivative $\frac{d^2I}{dV^2}$ against bias at different applied magnetic field: 0 T, 1T, 2 T, 3 T and 4 T, at operating temperature $T = 60\,\mathrm{K}$. **(a)** Theoretical results calculated for a TBRTS with $M = 5\,\mathrm{meV}$, $\Gamma = 1\,\mathrm{meV}$; assuming electron temperature $T_e = 150\,\mathrm{K}$. **(b)** Experimental results reported by Vdovin, *et al.* [107].

In Figure 5.8(a), the theoretical calculations of the second derivative $\frac{d^2I}{dV^2}$ as a function of bias are presented. The results are obtained from the TBRTS with $M = 5$ meV, $\Gamma = 1\,\mathrm{meV}$ in different applied magnetic field: 0 T, 1T, 2 T, 3 T and 4 T, at operating temperature $T = 60\,\mathrm{K}$. The results show that magnetic field flattens the local minimum. As the magnetic field is increased further, this local minimum is calculated to disappear for $B > 4\,\mathrm{T}$, while this was observed at $B \geq 3\,\mathrm{T}$ from the experimental data shown in Figure 5.8(b). However, it can be seen qualitatively that variations of the

theoretical curves of the second derivative agree quite well with the experimental results.

5.5 Conclusions

The concept of sequential tunneling has been introduced to explain the in-plane magnetic field dependence of the resonant tunneling in a triple barrier resonant tunneling structure. Typical I-V characteristics and their derivatives for a structure with particular design parameters have been calculated. The resulting calculations are investigated as a function of bias-voltage. It is found in the second derivative of the current that the resonance between E_1 and E_1^* exhibits itself as a visible feature in the background of a wide E_2 resonance. This feature has a sharp local maximum in the absence of applied magnetic field, and becomes flattened with increasing magnetic field. The magnetic field dependence of this feature can be explained by considering the rate equation for tunneling electrons based on the concept of sequential tunneling. Theoretical results agree well with the experimental data reported by Vdovin, *et al.* [107].

Chapter 6

Concluding remarks and future work

In this thesis intersubband relaxation of electrons in quantum wells has been theoretically investigated. Firstly, the in-plane kinetic energy, and also well width dependences of electron intra- or intersubband scattering rates (or times), associated by LO phonon emission in a semiconductor SQW structure were presented. Semi-analytic calculations, carried out for a GaAs/$Al_{0.3}Ga_{0.7}As$ SQW structure, show that the scattering rates (both for intra- and intersubband scattering) weakly depend on in-plane kinetic energy of the electron. Furthermore, the resulting calculations of well width dependence show that intrasubband scattering times gradually increase with well width contrasting with the intersubband scattering times which display a monotonic decrease. Secondly, a theoretical study of the condition to achieve inverted population in a semiconductor DQW structure was presented. The LO-phonon assisted tunneling rates, based on the Fröhlich interaction and Fermi's golden rule, has been performed for a GaAs/$Al_{0.3}Ga_{0.7}As$ DQW structure. The calculated results show that the tunneling rates monotonically decrease with the energy difference $E_1 - E_1^*$, and strongly depend on the magnitude of the transfer integral M.

Furthermore, electron transport and its kinetic, due to various types of scattering and tunneling mechanisms in a triple barrier resonant tunneling structure (TBRTS) were investigated. A system of coupled kinetic equations that describe the nonequilibrium electrons in the structure has been solved analytically to obtain subband distribution functions and gain spectra. Finally, the concept of sequential tunneling has been introduced to explain an in-plane magnetic field dependence of resonant tunneling in a TBRTS. Typical I-V characteristics and derivatives for the TBRTS with particular design parameters have been calculated. It is found in the second derivative of the

current that the resonance between E_1 and E_1^* exhibits itself as a visible feature in the background of a wide E_2 resonance. This feature has a sharp local maximum in the absence of applied magnetic field, and becomes flattened with increasing magnetic field in agreement with experiments.

The results from these calculations are relevant to real world devices such as quantum cascade lasers (QCLs). These structures contain active regions (often double quantum wells), linked by multiple quantum well bridging regions. Whilst the work presented here provides a valuable insight of electron transport and scattering in DQW structures (QCL active regions). A more realistic device would also include electron kinetics in the bridging regions.

Our future work will extend the calculations presented here, focussing on theoretical studies of the QCL operation, and also on the application of the relaxation kinetic model described in Chapter 4 to study the relaxation of electrons in real QCL structures. We will also numerically calculate distribution functions and gain spectra of a three-subband $GaAs/Al_xGa_{1-x}As$ DQW active region as a function of temperature and injected current.

References

[1] L. L. Chang, L. Esaki and R. Tsu, Appl. Phys. Lett. **24**, 593 (1974).

[2] F. Capasso, K. Mohammed, and A. Y. Cho, IEEE J. Quantum Electron. **QE-22**, 1853 (1986).

[3] L. Esaki and R. Tsu, IBM J. Res. Dev. **14**, 61 (1970).

[4] R. Tsu and L. Esaki, Appl. Phys. Lett. **22**, 562 (1973).

[5] L. Esaki and L. L. Chang, Phys. Rev. Lett. **33**, 495 (1974)

[6] L. Esaki, Rev. Mod. Phys. **46**, 237 (1974).

[7] R. F. Kazarinov and R. A. Suris, Sov. Phys. Semicond. **6**, 120 (1972).

[8] J. Faist, F. Capasso, D. L. Sivco, C. Sirtori, A. L. Hutchinson, and A. Y. Cho, Science **264**, 553 (1994).

[9] R. Q. Yang, Superlatt. Microstruct. **17**, 77 (1995).

[10] S. J. Allen, G. Brozak, E. Colas, F. De Rosa, P. England, J. Harbison, M. Helm, L. Florez, and M. Leadbeater, Semicond. Sci. Technol. **7**, B1 (1992).

[11] N. K. Dutta, in *Heterojuntion Band Discontinuities : Physics and Devivice Aplications*, edited by F. Capasso and G. Margaritondo (Elsevier Science Publisher B.V., Amsterdam, 1987).

[12] R. Ferreira and G. Bastard, Phys. Rev. B **40**, 1074 (1989).

[13] M. C. Tatham, J. F. Ryan and C. T. Foxon, Phys. Rev. Lett. **63**, 1637 (1989).

[14] F. H. Julien, Z. Moussa, P. Boucaud, Y. Lavon, A. Saar, J. Wang, J. P. Leburton, V. Berger, J. Nagle and R. Planel, Superlatt. Microstruct. **19**, 69 (1996).

[15] Y. B. Li, J. W. Cockburn, I. A. Larkin, J. P. Duck, M. J. Birkett, M. S. Skolnick, M. Hopkinson, R. Grey and G. Hill, Solid-State Electron. **42**, 1533 (1998).

[16] A. A. Andronov, Semicond. Sci. Technol. **7**, B629 (1992).

[17] M. Helm and S. J. Allen, Jr., Appl. Phys. Lett. **56**, 1368 (1990).

[18] K. Huang and B. Zhu, Phys. Rev. B **38**, 2183 (1988).

[19] H. Fröhlich, Adv. Phys. **3**, 325 (1954).

[20] S. M. Rytov, Sov. Phys. JETP **2**, 466 (1956).

[21] R. E. Camley and D. L. Mills, Phys. Rev. B **29**, 1695 (1984).

[22] C. Colvard, T. A. Gant, M. V. Klein, R. Merlin, R. Fischer, H Morkoc and A. C. Gossard, Phys. Rev. B **31**, 2080 (1985).

[23] M. V. Klein, IEEE J. Quantum Electron.**QE-22**, 1760 (1986).

[24] J. Shi and S. Pan, Phys. Rev. B **51**, 17681 (1995).

[25] K. Huang and B. Zhu, Phys. Rev. B **38**, 13377 (1988).

[26] S. Rudin and T. L. Reinecke, Phys. Rev. B **41**, 7713 (1990).

[27] G. Weber, A. M. Paula and J. F. Ryan, Semicond. Sci. Technol. **6**, 397 (1991).

[28] E. Molinari, C. Bungaro, M.Gulia, P. Lugli and H. Rücker, Semicond. Sci. Technol. **7**, B67 (1992).

[29] H. Rücker, E. Molinari and P. Lugli, Phys. Rev. B **45**, 6747 (1992).

[30] A. R. Bhatt, K. W. Kim, M. A. Stroscio and J. M. Higman, Phys. Rev. B **48**, 14671 (1993).

[31] G. Weber and A. M. Paula, Appl. Phys. Lett. **63**, 3026 (1993).

[32] A. M. Paula and G. Weber, Appl. Phys. Lett. **65**, 1281 (1994).

[33] K. L. Schumacher, D. Collings, R. T. Phillips, D. A. Ritchie, G. Weber,, J. N. Shulman and K. Ploog, Semicond. Sci. Technol. **11**, 1173 (1996).

[34] K. Kunc and R. M. Martin, Phys. Rev. Lett. **48**, 406 (1982).

[35] S. Baroni, P. Giannozzi and E. Molinari, Phys. Rev. B. **41**, 3870 (1990).

[36] S. F Ren, H. Chu and Y. C Chang, Phys. Rev. Lett. **59**, 1841 (1987).

[37] S. Yip and Y. C. Chang, Phys. Rev. B **30**, 7037 (1984).

[38] S. Datta, *Quantum Phenomena* (Addison-Wesley Publishing Company, New York, 1989).

[39] G. Bastard, Phys. Rev. B **24**, 5693 (1981).

[40] G. Bastard, Phys. Rev. B **25**, 7584 (1982).

[41] G. Bastard and J. A. Brum, IEEE J. Quantum Electron. **QE-22**, 1625 (1986).

[42] D. J. Ben Daniel and C. B. Duke, Phys. Rev. **152**, 683 (1966).

[43] E. O. Kane, J. Phys. Chem. Solids **1**, 249 (1957).

[44] S. R. White and L. J. Sham, Phys. Rev. Lett. **47**, 879 (1981).

[45] R. Dingle, W. Wiegmann and C. H. Henry, Phys. Rev. Lett. **33**, 827 (1974).

[46] W. A. Harrison, Phys. Rev. **123**, 85 (1961).

[47] Q.-G Zhu and H. Kroemer, Phys. Rev. B **27**, 3519 (1983).

[48] O. von Roos, Phys. Rev. B **27**, 7547 (1983).

[49] R. A. Morrow and K. R. Brownstein, Phys. Rev. B **30**, 678 (1984).

[50] R. A. Morrow, Phys. Rev. B **35**, 8074 (1987).

[51] I. Galbraith and G. Duggan, Phys. Rev. B **38**, 10057 (1988).

[52] A. V. Kolesnikov and A. P. Silin, Phys. Rev. B **59**, 7596 (1999).

[53] L. D. Landau and E. M. Lifshitz, *Quantum Mechanics: Non-relativistic Theory*, 3rd Edition (Butterwort-Heinemann, Oxford, 1998).

[54] H. Kroemer, Wu-Yi Chien, J. S. Harris, Jr., and D. D. Edwall, Appl. Phys. Lett. **36**, 295 (1980).

[55] S. Adachi, J. Appl. Phys. **58**, 1985.

[56] S. A. Lyon and C. L. Petersen, Semicond. Sci. Technol. **7**, B21 (1992).

[57] R. Lake, G. Klimeck and S. Datta, Phys. Rev. B **47**, 6427 (1993).

[58] B. K. Ridley, J. Phys. C: Solid State Phys. **15**, 5899 (1982).

[59] F. A. Riddoch and B. K. Ridley, J. Phys. C: Solid State Phys. **16**, 6971 (1983).

[60] P. J. Price, Ann. Phys. NY **133**, 217 (1981).

[61] S. Das Sarma and B. A. Mason, Ann. Phys. NY **163**, 78 (1985).

[62] Y. B. Li, J. W. Cockburn, J. P. Duck, M. J. Birkett, M. S. Skolnick, I. A. Larkin, M. Hopkinson, R. Grey and G. Hill, Phys. Rev. B **57**, 6290 (1998).

[63] S. Khan-ngern and I. A. Larkin, Phys. Lett. A **266**, 209 (2000).

[64] S. S. Allen and S. L. Richardson , Phys. Rev. B **50**, 11693 (1994).

[65] T. B. Boykin, J. Appl. Phys. **78**, 6818 (1995).

[66] X. D. Zhao, H. Yamamoto, Y. Nakano and K. Taniguchi, Superlatt. Microstruct. **23**, 1273 (1998).

[67] C. Wirner, Y. Awano, T. Mori, N. Yokoyama, T. Nakagawa, H. Bando and S. Muto, Appl. Phys. Lett. **69**, 1596 (1996).

[68] L. D. Macks, S. A. Brown, R. G. Clark, R. P. Starrett, M. A. Reed, M. R. Deshpande, C. J. L. Fernando and W.R. Frensley, Phys. Rev. B **54**, 4857 (1996).

[69] Y. Ji, Y. Chen, K. Luo, H. Zheng, Y. Li, C. Li, W. Cheng and F. Yang, Appl. Phys. Lett. **72**, 3309 (1998).

[70] N. Zou and K. A. Chao, Phys. Rev. Lett. **69**, 3224 (1992).

[71] C. H. Grein, E. Runge and H. Ehrenreich, Phys. Rev. B **47**, 12590 (1993).

[72] P. Roblin and W. R. Liou, Phys. Rev. B **47**, 2146 (1993).

[73] M. Jonson, Phys. Rev. B **39**, 5924 (1989).

[74] W. Cai, T. F. Zheng, P. Hu, B. Yudanin and M. Lax, Phys. Rev. Lett. **63**, 418 (1989).

[75] N. S. Wingreen, K. W. Jacobsen and J. W. Wilkins, Phys. Rev. Lett. **61**, 1396 (1988).

[76] V. J. Goldman, D. C. Tsui and J. E. Cunningham, Phys. Rev. B **36**, 7635 (1987).

[77] B. Ricco and M. Ya. Azbel, Phys. Rev. B **29**, 1970 (1984).

[78] R. Tsu and G. Döhler, Phys. Rev. B **12**, 680 (1975).

[79] D. Calecki, J. F. Palmier and A. Chomette, J. Phys. C **17**, 5017 (1984).

[80] T. Weil and B. Vinter, J. Appl. Phys. **60**, 3227 (1986).

[81] P. Harrison, Semicond. Sci. Technol. **12**, 1487 (1997).

[82] D. de Cogan, *Solid State Devices: A Quantum Physics Approach* (Macmillan Education Ltd., London, 1987).

[83] J. H. Davies, *The Physics of Low-Dimensional Semiconductors: An Introduction* (Cambridge University Press, New York, 1998).

[84] C. Weisbuch and B. Vinter, *Quantum Semiconductor Structures: Fundamentals and Applications* (Academic Press, Inc., San Diego, 1991).

[85] A. B. Migdal, *Qualitative Methods in Quantum Theory* (W. A. Benjamin, Inc., Massachusetts, 1977).

[86] (a) S. A. Gurvitz, Phys. Rev. A **38**, 1747 (1988).

(b) S. A. Gurvitz and M. S. Marinov, Phys. Rev. A **40**, 2166 (1989).

(c) S. A. Gurvitz, I. Bar-Joseph, and B. Deveaud, Phys. Rev. B **43**, 14703 (1991).

(d) I. Bar-Joseph and S. A. Gurvitz, Phys. Rev. B **44**, 3332 (1991).

[87] A. A. Grinberg and S. Luryi, Phys. Rev. Lett. **65**, 1251 (1990).

[88] S. M. Goodnick and P. Lugli, Phys.Rev. B **37**, 2578 (1988).

[89] C. H. Yang, J. M. Carlson-Swindle and S. A. Lyon, Phys. Rev. Lett. **55**, 2359 (1985).

[90] B. Gelmont, V. B. Gorfinkel and S. Luryi, Appl. Phys. Lett. **68**, 2171 (1996).

[91] V. B. Gorfinkel, S. Luryi and B. Gelmont, IEEE J. Quantum Electron. **32**, 1995 (1996).

[92] J. Faist, F. Capasso, C. Sirtori, D. L. Sivco, A. L. Hutchinson, M. S. Hybertsen and A. Y. Cho, Phys. Rev. Lett **76**, 411 (1996).

[93] V. F. Elesin and A. V. Krasheninnikov, Physica A **241**, 386 (1997).

[94] P. Kinsler, P. Harrison and R. W. Kelsall, Phys. Rev. B **58**, 4771 (1998).

[95] P. Lugli and S. M. Goodnick, Phys. Rev. Lett. **59**, 716 (1987).

[96] P. Lugli, P. Bordone, L. Reggiani, M. Rieger, P. Kocevar and S. M. Goodnick, Phys. Rev. B **39**, 7852 (1989).

[97] E. Fermi, *Notes on Quantum Mechanics* (The University of Chicaco Press, Chicago, 1962).

[98] B. G. Streetman, *Solid State Electronic Devices* (Prentice-Hall International, Inc., 4th Edition, New Jersey, 1995).

[99] S. E. Esipov and Y. B. Levinson, Sov. Phys. JETP **63**, 191 (1986).

[100] S. E. Esipov and Y. B. Levinson, Adv. Phys. **36**, 331 (1987).

[101] J. H. Smet, C. G. Fonstad and Q. Hu, J. Appl. Phys. **79**, 9305 (1996).

[102] P. J. Price, Phys. Rev. B **30**, 2234 (1984).

[103] V. F. Elesin and Yu. V. Kopaev, JETP **81**, 1192 (1995).

[104] I. A. Larkin, Sov. Phys. Semicond. **23**, 1028 (1989).

[105] E. M. Liftshitz and L. P. Pitaevskii, *Physical Kinetics Vol. 10* (Butterworth-Heinemann, Oxford, 1997).

[106] Y. Lavon, A. Saar, Z. Moussa, F. H. Julien, and R. Planel, Superlattices and Microstructures **19**, 1 (1996).

[107] E. E. Vdovin, I. A. Larkin, Yu. N. Khanin, J. P. Duck, J. W. Cockburn, and Yu. V. Dubrovskii, Phys. Low-Dim. Struct. **7/8**, 113 (2000).

[108] L. Eaves, G. A. Toombs, F. W. Sheard, C. A. Payling, M. L. Leadbeater, A. S. Alves, T. J. Foster, P. E. Simmonds, M. Henini, O. H. Hughes, J. C. Portal, G. Hill, and M. A. Pate, Appl. Phys. Lett. **52**, 212 (1988).

Appendix A

Solutions of the model kinetic equations

To solve the model equation given in Eq. (4.40) we first introduce dimensionless parameters; $\eta = \frac{\tau_0}{\tau_{ee}}$, $\xi_1 = \frac{\tau_0}{\tau_1}$, $\xi_2 = \frac{\tau_0}{\tau_{12}}$, $\Lambda_{ee} = \frac{k_B T_e}{\hbar\omega_0}$ and $y_i = \frac{\varepsilon_i}{\hbar\omega_0}$, and Eq.(4.40) is then transformed to the dimensionless kinetic equation as follows:

I. For the upper subband E_2:

(a) $0 < y < 1$;

$$\eta\Lambda_{ee}\frac{d^2 f_2(y)}{dy^2} + \eta\frac{df_2(y)}{dy} + (N_0+1)f_2(y+1) - \alpha_2 f_2(y) = -P_0\delta(y-y_0), \quad \text{(A-1)}$$

(b) $y > 1$;

$$\eta\Lambda_{ee}\frac{d^2 f_2(y)}{dy^2} + \eta\frac{df_2(y)}{dy} + (N_0+1)f_2(y+1) + N_0 f_2(y-1) - \beta_2 f_2(y) = 0, \quad \text{(A-2)}$$

where $y \equiv y_2$, $\alpha_2 = N_0 + \xi_2(2N_0+1)$, $\beta_2 = (2N_0+1)(1+\xi_2)$, $P_0 = \frac{\tau_0 G_0}{\rho_2\hbar\omega_0}$.

The kinetic equations given in Eqs.(A-1) and (A-2) can be solved by assuming the general solution $f_2(y)$ in the form

$$f_2(y) = f_2^{(0)}(y) + \frac{1}{\sqrt{2\pi}}\int_{-\infty}^{+\infty} dk e^{-iky} D_2(k)\varphi_2^{(0)}(k), \quad \text{(A-3)}$$

$$D_2(k) = \frac{1}{-\eta\Lambda_{ee}k^2 - \eta k + (N_0+1)e^{-ik} + N_0 e^{ik} - \beta_2}, \quad \text{(A-4)}$$

$$\varphi_2(k) = -\frac{1}{\sqrt{2\pi}}\int_{-\infty}^{+\infty} dy e^{-iky} D_2(k) f_2^{(0)}(y-1), \quad \text{(A-5)}$$

where $f_2^{(0)}(y)$ is the zeroth order solution given as follows:

$$f_2^{(0)}(y) = \begin{cases} A_1 e^{\mu_2^- y} + A_2 e^{\mu_2^+ y} & ;\ 0 < y < y_0 \\ A_3 e^{\mu_2^- y} + A_4 e^{\mu_2^+ y} & ;\ y_0 < y < 1 \\ A_5 e^{\lambda_2 y} & ;\ y > 1 \end{cases} \qquad \text{(A-6)}$$

where $\mu_2^{\mp} = \dfrac{-\eta \mp \sqrt{\eta^2 + 4\eta\Lambda_{ee}\alpha_2}}{2\eta\Lambda_{ee}}$, and $\lambda_2 = \dfrac{-\eta - \sqrt{\eta^2 + 4\eta\Lambda_{ee}\beta_2}}{2\eta\Lambda_{ee}}$. The arbitary constants $A_1 - A_5$ are obtained from the following boundary conditions:

(i)at $y = 0$;

$$J_{ee}(y)\big|_{y=0} = 0 \quad \rightarrow \quad \left[\Lambda_{ee}\frac{df_2(y)}{dy} + f_2(y)\right]_{y=0} = 0$$

(ii)at $y = y_0$;

$$f_2(y)\big|_{y=y_0^+} = f_2(y)\big|_{y=y_0^-} \text{ , and } \eta\Lambda_{ee}\left[\left.\frac{df_2(y)}{dy}\right|_{y=y_0^+} - \left.\frac{df_2(y)}{dy}\right|_{y=y_0^-}\right] = P_0$$

(iii)at $y = 1$;

$$f_2(y)\big|_{y=1^+} = f_2(y)\big|_{y=1^-} \text{ , and } \left.\frac{df_2(y)}{dy}\right|_{y=1^+} = \left.\frac{df_2(y)}{dy}\right|_{y=1^-}$$

II. For the lower subband E_1

(a) $0 < y_1 < 1$;

$$\eta\Lambda_{ee}\frac{d^2 f_1(y_1)}{dy_1^2} + \eta\frac{df_1(y_1)}{dy_1} + (N_0+1)f_1(y_1+1) - \alpha_1 f_1(y_1) = 0\ , \qquad \text{(A-7)}$$

(b) $y_1 > 1$;

$$\eta\Lambda_{ee}\frac{d^2 f_1(y_1)}{dy_1^2} + \eta\frac{df_1(y_1)}{dy_1} + (N_0+1)f_1(y_1+1) + N_0 f_1(y_1-1) - \beta_1 f_1(y_1) = P_1(y_1)\ ,$$

(A-8)

where $\alpha_1 = N_0 + \xi_1(2N_0+1)$, $\beta_1 = (2N_0+1)(1+\xi_1)$,

and $P_1 = \xi_2\left(\frac{m_2^*}{m_1^*}\right)\left[(N_0+1)f_2\left(y_1+1-\frac{\hbar\Omega_0}{\hbar\omega_0}\right)+N_0 f_2\left(y_1-1-\frac{\hbar\Omega_0}{\hbar\omega_0}\right)\right]$.

General solutions of the kinetic equations given in Eqs.(A-7) and (A-8) can be written in the form

$$f_1(y_1) = \begin{cases} B_1 e^{\mu_1^- y_1} + B_2 e^{\mu_1^+ y_1} + F_1(y_1) & ;\ 0 < y_1 < 1 \\ B_3 e^{\lambda_1 y_1} + F_1(y_1) & ;\ y_1 > 1 \end{cases} \tag{A-9}$$

$$F_1(y_1) = \frac{1}{\sqrt{2\pi}} \int_{-\infty}^{+\infty} dk e^{-iky_1} D_1(k)\varphi_1^{(0)}(k)\,, \tag{A-10}$$

$$D_1(k) = \frac{1}{-\eta\Lambda_{ee}k^2 - \eta k + (N_0+1)e^{-ik} + N_0 e^{ik} - \beta_1}\,, \tag{A-11}$$

$$\varphi_1(k) = -\frac{1}{\sqrt{2\pi}} \int_{-\infty}^{+\infty} dy_1 e^{-iky_1} D_1(k)P_1(y_1)\,, \tag{A-12}$$

where $\mu_1^{\mp} = \frac{-\eta \mp \sqrt{\eta^2 + 4\eta\Lambda_{ee}\alpha_1}}{2\eta\Lambda_{ee}}$, and $\lambda_1 = \frac{-\eta - \sqrt{\eta^2 + 4\eta\Lambda_{ee}\beta_1}}{2\eta\Lambda_{ee}}$. The arbitary constants $B_1 - B_3$ are obtained from the following boundary conditions:

(i) at $y_1 = 0$;

$$J_{ee}(y_1)\big|_{y_1=0} = 0 \quad \rightarrow \quad \left[\Lambda_{ee}\frac{df_1(y_1)}{dy_1} + f_1(y_1)\right]_{y_1=0} = 0$$

(ii) at $y_1 = 1$;

$$f_1(y_1)\big|_{y_1=1^+} = f_1(y_1)\big|_{y_1=1^-}\,, \text{ and } \left.\frac{df_1(y_1)}{dy_1}\right|_{y_1=1^+} = \left.\frac{df_1(y_1)}{dy_1}\right|_{y_1=1^-}$$

Appendix B

Our Publications

PHYSICAL REVIEW B, VOLUME 64, 115313

Nonequilibrium electrons in double quantum well structures: A Boltzmann equation approach

S. Khan-ngern and I. A. Larkin
Department of Physics and Astronomy, University of Sheffield, Sheffield S3 7RH, United Kingdom
(Received 24 January 2001; published 29 August 2001)

A theoretical study of hot electrons in double quantum well is presented. We consider a system of coupled kinetic equations that describe nonequilibrium population in two lowest subbands, and find an analytical solution of these equations. All previous treatments of the electron distribution functions are based on the two extreme limits $\tau_0/\tau_{ee} \ll 1$ or $\tau_0/\tau_{ee} \gg 1$, where τ_0 and τ_{ee} refer to electron-LO-phonon (e-LO) and electron-electron (e-e) scattering times, respectively. In our approach, the distribution functions are investigated for the whole range of τ_0/τ_{ee} ratios. The outcome of kinetic equation for subband distribution functions provides a comprehensive description of the lasing process in the intersubband lasers. Our calculations show that the lower subband distribution function above LO-phonon threshold is always strongly nonequilibrium and deviates far from thermal distributions while in the region below the LO-phonon threshold it could be close to a Maxwellian. Using these distribution functions we calculate spectral density of gain at various temperatures.

DOI: 10.1103/PhysRevB.64.115313 PACS number(s): 42.55.Px, 72.10.−d, 85.30.−z

I. INTRODUCTION

Studies of mid- and long-wavelength infrared lasers based on electronic intersubband transitions within the quatum wells (QW's) in semiconductor low-dimentional heterostructures have attracted a great amount of interest since the first demonstration of a so-called quantum cascade laser (QCL) was reported by Faist *et al.*[1] Continued delvelopment of the QCL operation, improving the threshold current and the maximum temperature of operation, requires a sound understanding of the effects of changing design parameters on the intersubband population kinetics. To create lasing efficiency, in general, it requires specially designed structures providing sufficient global population inversion between the two subbands involved.

In our earlier works[2,3] it has been shown that to achieve inverted population in a modified GaAs/$Al_xGa_{1-x}As$ double QW structure schematically shown in Fig. 1, which is occasionally used as an intersubband lasing structure that consists of a wider well (QW1) as a lasing unit and a narrower well (QW2) as an electronic energy filter by various types of tunneling mechanisms, we should ensure efficient drain of carriers from E_1 subband. This happens when the device has appropriate design parameters providing a good electron confinement at E_2 subband and short electron lifetime at the E_1 subband. Recently, it has been shown by Faist *et al.*[4] that for lasing in the intersubband lasers, global population inversion is not a necessary condition but that nonparabolicities combined with the nonthermal electron distribution in the laser unit can make lasing action possible. This idea has been studied theoretically by Gelmont *et al.*[5] and Gorfinkel *et al.*[6] The main resulting calculations of these papers were directed to investigate the spectral line shape of radiative intersubband transitions in a QW. It has been found that the line shape of radiative intersubband transitions is determined by two factors: (i) the electron intra- and intersubband scattering rates, and (ii) the effective mass differences between the two subbands involved. The interplay between these two factors leads to essential non-Lorentzian form of the spectral line. The calculations of spectral density of gain $g(\Omega)$ are described as a functional on electron distribution functions $f_1(\varepsilon_1)$ and $f_2(\varepsilon_2)$ in both subbands E_1 and E_2, where ε_1 and ε_2 are kinetic energies in the subbands E_1 and E_2, respectively. Generally, the distribution functions are nonthermal and their actual shapes affect strongly the spectral density of gain.[6] At very low concentrations the distribution function $f_1(\varepsilon_1)$ is given by a quasidiscrete ladder with the occupation probabilities decreasing toward the subband bottom.[6,7] This is very unusual distribution because electron-electron (e-e) scattering is very effective for the actual concentrations. Therefore, thermal equilibrium distribution function based on arguments of fast e-e scattering is considered in the majority of these papers.[6–8] However, there is substantial gap between the two limiting cases. The most typical shape is continuous, but the distribution function is strongly nonequilibrium. This behavior, in fact, has been studied extensively via the ensemble Monte Carlo technique (see particularly the work of Goodnick collaborators).[9–11]

In this paper we study kinetics of electrons scattering in triple-barrier double QW heterostructures shown in Fig. 1. A model kinetic equation involving terms that describe the electron-LO-phonon and e-e scattering, as well as electron-escape and electron-generation processes has been derived. Analytic solutions of the kinetic equation for distribution functions in the two subbands have been found and obtained a comprehensive description of the lasing process in the intersubband lasers.

The paper is organised as follows: formulation of the problem is described in Sec. II, where expressions for the model kinetic equation is derived. In Sec. III and Sec. IV we present and discuss our calculations of subband distribution functions and the spectral density of gain. Finally, conclusions are addressed in Sec. V, and useful mathematical details are presented in the Appendix.

II. FORMULATION OF THE PROBLEM

Main purpose of this present work is to investigate nonequilibrium behavior of electrons in the two subbands E_1 and E_2 (see also Fig. 1). The kinetics of electron scattering in

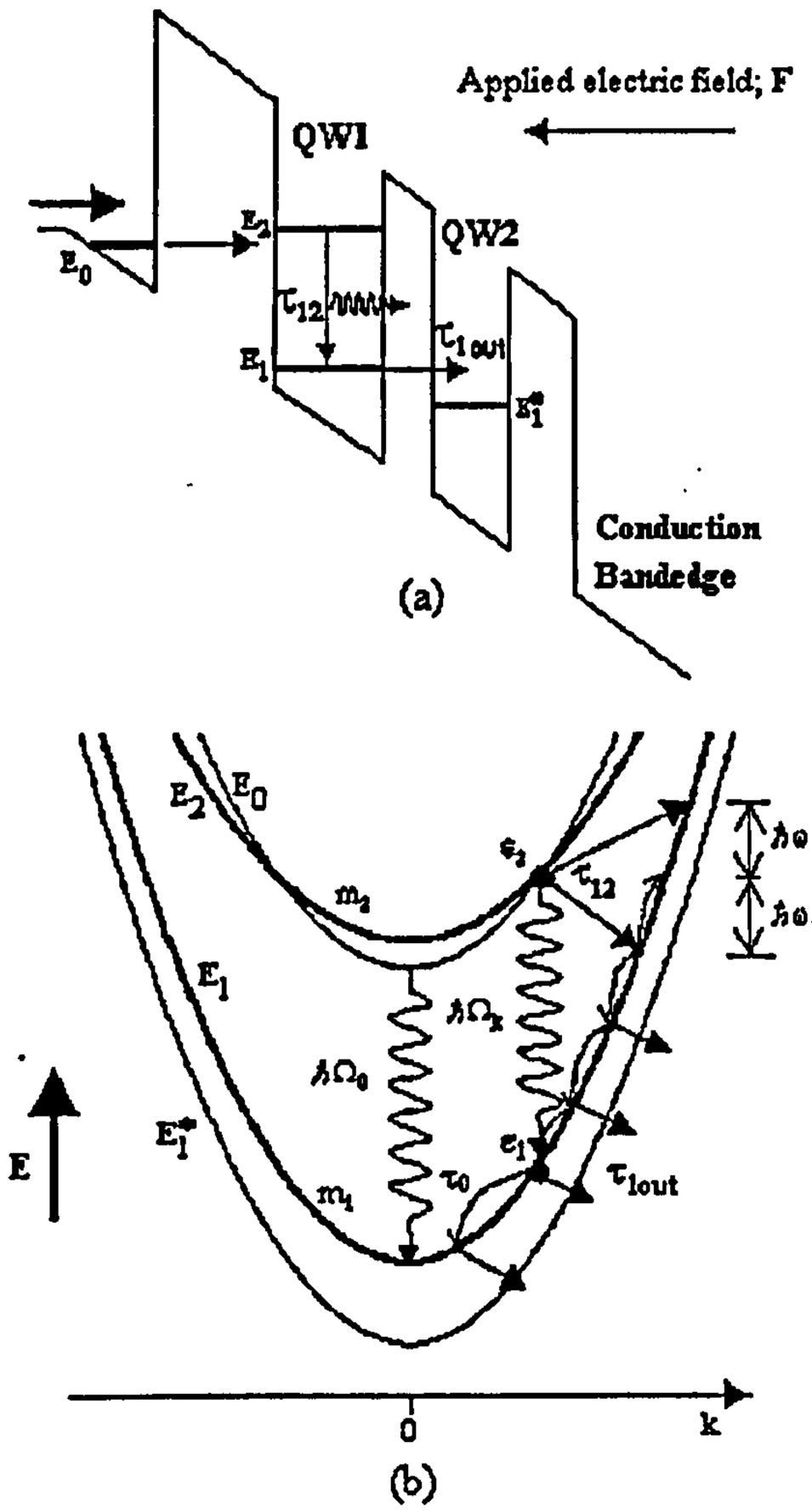

FIG. 1. (a) Schematic diagram of the conduction band of a double QW structure and kinetics of electrons scattering. (b) The subband diagram presenting the radiative intersubband transitions in the QW1, and also shown are the nonradiative inter- and intrasubband transitions by emission or absorption of LO phonons.

our physical system can be described by a model kinetic equation[12–14]

$$\frac{\partial f_i(\varepsilon_i)}{\partial \varepsilon_i} = S_{LO}(\varepsilon_i) + C_{ee}(\varepsilon_i) + R_i(\varepsilon_i) + G_i(\varepsilon_i); \quad i = 1,2 \tag{2.1}$$

where $f_i(\varepsilon_i)$ is the electron energy distribution function, corresponding to the occupation probability of kinetic-energy states ε_i in subband E_i; here E_i denotes the total energy of electrons. We consider the dispersion relations $\varepsilon_{1,2}(k)$ in both subbands are different and nonparabolic. However, all the effects of interest here are simplified by regarding the subbands themselves as parabolic, but characterized by different effective mass m_1 and m_2[6]

$$\varepsilon_{1,2}(k) = E_{1,2}(k) - E_{1,2}(0) = \frac{\hbar^2 k^2}{2m_{1,2}}, \tag{2.2}$$

where k is the magnitude of in-plane wave vector of the electron.

Electron-LO-phonon scattering. The term $S_{LO}(\varepsilon_i)$ is responsible for electron scattering by LO phonons in subband E_i, so that

$$S_{LO}(\varepsilon_i) = -\gamma(\varepsilon_i) f_i(\varepsilon_i) + B_i(\varepsilon_i), \tag{2.3}$$

$$\gamma(\varepsilon_i) = \frac{1}{\tau_0} \times [N_0 + (N_0+1)\Theta(\varepsilon_i - \hbar\omega_0)], \tag{2.4}$$

$$B_i(\varepsilon_i) = \frac{1}{\tau_0} \times [(N_0+1) f_i(\varepsilon_i + \hbar\omega_0) + N_0 \Theta(\varepsilon_i - \hbar\omega_0) f_i(\varepsilon_i - \hbar\omega_0)], \tag{2.5}$$

where Θ is a step function, and τ_0 the intrasubband relaxation time due to a spontaneous LO-phonon emission. For a sufficient narrow QW of any shape, the time constant $\tau_0 \sim 0.1$ ps (for GaAs).[5,6,15] N_0 is the phonon Planck function. If LO phonons are strongly nonequilibrium, one can use the appropriate function instead of N_0.[16] In our case it will lead to effective LO phonon temperature that differs from the lattice temperature T_L. The function $\gamma(\varepsilon_i)$ describes the transverse-phase relaxation rate due to the intrasubband scattering, which is dominated by the interaction with LO phonons. The latter term $B_i(\varepsilon_i)$ is responsible for the incoming electron scattering by emission and absorption of LO phonons.

Electron-electron scattering. To calculate the term $C_{ee}(\varepsilon_i)$ that describes e-e scattering processes, we have to consider e-e scattering probability $W_{ee}(\varepsilon_i \to \varepsilon_f')$ of interacting electrons from initial states ε_i in subband E_i to the final states ε_f' in subband E_f. In a system with isotropic or nearly isotropic electron distributions, the probability $W_{ee}(\varepsilon_i \to \varepsilon_f')$ is given by[12]

$$W_{ee}(\varepsilon_i \to \varepsilon_f') = \frac{1}{\pi}\int_0^{\pi} d\phi\, W_{ee}(\vec{k}_i \to \vec{k}_f') \tag{2.6}$$

$$W_{ee}(\vec{k}_i \to \vec{k}_f') = \sum_{\vec{k}_j, \vec{k}_g'} f_j(\varepsilon_j) \frac{2\pi}{\hbar} |M_{\vec{k}_f', \vec{k}_g'; \vec{k}_i, \vec{k}_j}|^2 \times \delta(\varepsilon_i + \varepsilon_j - \varepsilon_f' - \varepsilon_g') \tag{2.7}$$

here $M_{\vec{k}_f', \vec{k}_g'; \vec{k}_i, \vec{k}_j}$ is the matrix element for the e-e scattering process of an electron with wave vector $\vec{k}_i$ in subband E_i and a second electron with wave vector $\vec{k}_j$ in subband E_j into the final states with wave vector $\vec{k}_f'$ and $\vec{k}_g'$ in subbands E_f and E_g, respectively. For the problem with isotropic electron distributions, the average of the probability $W_{ee}(\vec{k}_i \to \vec{k}_f')$ over the angle ϕ between $\vec{k}_i$ and $\vec{k}_f'$ enters into the calculations as given in Eq. (2.9).

For reasons of simplifications we neglect any mismatch in the properties of the narrow- and wide-gap semiconductor lattices and also disparities in the dielectric permittivity. We then use an e-e interaction operator of the form $U_{ee} = e^2/(4\pi\kappa r)$; where e is the electronic charge, κ the

dielectric permittivity of the QW and r the distance between two interacting electrons. The matrix element $M_{\vec{k}_f',\vec{k}_g';\vec{k}_i,\vec{k}_j}$ is consequently obtained[12]

$$M_{\vec{k}_f',\vec{k}_g';\vec{k}_i,\vec{k}_j}=\left\langle \vec{k}_f',\vec{k}_g'\left|\frac{e^2}{4\pi\kappa r}\right|\vec{k}_i,\vec{k}_j\right\rangle=\frac{1}{S}\left(\frac{e^2}{2\kappa Q}\right)\delta_{\vec{k}_f',\vec{k}_g',\vec{k}_i,\vec{k}_j}, \tag{2.8}$$

where $Q=|\vec{k}_f'-\vec{k}_g'|=|\vec{k}_i-\vec{k}_j|$ is the relative in-plane wave vector of the interacting electrons, which determines the in-plane momentum transfer of the electrons, and S the surface area of the QW.

Finally, one can obtain the e-e scattering $C_{ee}(\varepsilon_i)$ in the collision integral form[12,13]

$$C_{ee}(\varepsilon_i)=\int_0^\infty d\varepsilon_j'\rho_j(\varepsilon_j')[W_{ee}(\varepsilon_j'\rightarrow\varepsilon_i)f_j(\varepsilon_j') - W_{ee}(\varepsilon_i\rightarrow\varepsilon_j')f_i(\varepsilon_i)] \tag{2.9}$$

where $\rho_i(\varepsilon_i)=m_i/(\pi\hbar^2)$ is the two-dimensional (2D) density of states in subband E_i.

The general expression for $C_{ee}(\varepsilon_i)$ given by Eq. (2.9) associated with Eqs. (2.6)–(2.8) is very complicated, on the contrary to the other terms S_{LO}, R_i, and G_i, as it is a bilinear functional on the electron distribution function. To reduce it to a linear integral equation form one can put in Eq. (2.7) the Maxwellian distribution

$$f_i(\varepsilon_i)=n_i\left(\frac{\pi\hbar^2}{m_iT_e}\right)\exp\left(-\frac{\varepsilon_i}{T_e}\right),$$

where n_i is the number of electrons per unit area in subband E_i, and T_e the electron temperature in energy units. Physically it means that scattering of the minority of high kinetic-energy electrons is affected only by the experience on the majority of quasithermalized electrons. In general, it is meaningful to define the electron temperature T_e different from the lattice temperature T_L when the energy relaxation due to e-e scattering is faster than the energy relaxation due to LO-phonon scattering, i.e., $\tau_{ee}<\tau_0\exp(\hbar\omega_0/T_e)$.[13] At this condition the temperature T_e can be found using the energy-balance equation. Even with this simplification the e-e scattering probability $W_{ee}(\varepsilon_i\rightarrow\varepsilon_f')$ is still complicated and could be solved analytically only in some special cases.[12,17] To handle the problem analytically we will use a consequence of the Coulomb singularity of the matrix element $M_{\vec{k}_f',\vec{k}_g';\vec{k}_i,\vec{k}_j}$ at small momentum transfer. This singularity implies that scattering events with low-energy transfer are dominant. As a result, one can use the Fõkker-Planck-Landau (FPL) approximation to transform the collision integral Eq. (2.9) into a differential form[18]

$$C_{ee}(\varepsilon_i)=-\frac{1}{\rho_i(\varepsilon_i)}\frac{\partial}{\partial\varepsilon_i}[\rho_i(\varepsilon_i)J_{ee}(\varepsilon_i)]=-\frac{\partial}{\partial\varepsilon_i}J_{ee}(\varepsilon_i), \tag{2.10}$$

where the flux on the energy axis $J_{ee}(\varepsilon_i)$ is

$$J_{ee}(\varepsilon_i)=-\left[A_{ee}(\varepsilon_i)+D_{ee}(\varepsilon_i)\frac{\partial}{\partial\varepsilon_i}\right]f_i(\varepsilon_i), \tag{2.11}$$

$$A_{ee}(\varepsilon_i)=\int_0^\infty d\varepsilon_i'\rho_i(\varepsilon_i')(\varepsilon_i-\varepsilon_i')W_{ee}(\varepsilon_i\rightarrow\varepsilon_i'), \tag{2.12}$$

$$D_{ee}(\varepsilon_i)=\frac{1}{2}\int_0^\infty d\varepsilon_i'\rho_i(\varepsilon_i')(\varepsilon_i-\varepsilon_i')^2W_{ee}(\varepsilon_i\rightarrow\varepsilon_i') \tag{2.13}$$

where $A_{ee}(\varepsilon_i)$ is the dynamic friction, and $D_{ee}(\varepsilon_i)$ the energy-diffusion coefficients.

Recently, it has been numerically shown by Kinsler *et al.*[8] and Smet *et al.*[14] that e-e scattering is dominated by small-angle intrasubband events ($i=f$ and $j=g$) in which the initial electrons stay within their original subband after scattering and their relative momentum transfer is small resulting in a small value of the energy transfer. The main investigations of these papers[8,14] are directed to e-e intersubband scattering ($i\neq f$ or $j\neq g$). In this case the energy of final states of electrons lies in a narrow region. Their resulting calculations show that the intersubband e-e scattering events, which do involve a change of subband at least for one of the electrons, vanish at small values of in-plane wave vector $k<k_{min}$; where k_{min} is the minimum value of k that permits the intersubband transitions occur. For electrons at large values of in-plane wave vector $k>k_{min}$, where the e-e intersubband transitions is possible, e-e intersubband scattering processes are typically less important when compared to e-e intrasubband transitions. In addition, they have also pointed out that for sufficient large values of energy separation between subbands, e-e intersubband transitions become much weaker when compared to the e-e intrasubband scattering processes. These relevant results enable us to necglect e-e intersubband scattering processes and take into account only e-e subband transitions. For the kinetic energies $\varepsilon_i\gg T_e$ the dynamic friction coefficient $A_{ee}(\varepsilon_i)$ is independent of kinetic energy[12]

$$A_{ee}(\varepsilon_i)\equiv A_{ee}=\left(\frac{e^4}{32\hbar\kappa^2}\right)n_s=\frac{\hbar\omega_0}{\tau_{ee}}, \tag{2.14}$$

where $n_s=n_1+n_2$ is the electron concentration in the QW1 and τ_{ee} is responsible for the e-e relaxation time at LO-phonon threshold. This relaxation time τ_{ee} is important for describing the competition between e-e scattering and the LO phonon emission near the the threshold regarded as a dimensionless parameter

$$\eta=\frac{\tau_0}{\tau_{ee}}=\left[\frac{\tau_0e^4}{32\kappa^2\hbar^2\omega_0}\right]n_s=\frac{n_s}{3.84\times10^{11}\ \text{cm}^{-2}} \tag{2.15}$$

(for the GaAs QW). At high electron concentration where η is large that characterizes the dominant of e-e scattering. The e-e scattering rate we defined in Eq. (2.14) differs from the e-e scattering rate introduced in Ref. 10, $\Gamma_{max}=e^4m^*n_s/(4\hbar^3\kappa^2q_0^2)$ in SI units. Here m^* stands for the electron effective mass in the QW and q_0 is the inverse

screening length in two dimensions. The reason for this is that electron-gas-energy transfer rate is determined by transport cross section that differs from total cross section on the screened Coulomb potential that has been used in the Monte Carlo simulations.[10] To compare the efficiency between e-e and e-LO scattering we calculate the time τ_{ee} that the electron requires to lose the energy $\hbar\omega_0$ by e-e collisions. If screening parameter $q_0 \ll \sqrt{2m^*\omega_0/\hbar}$, τ_{ee} appears to be energy independent that makes the problem more simplistic.

Electron escape from the subband. The term $R_i(\varepsilon_i)$ describes electron escape from subband E_i. For the lower subband E_1 in QW1 (see also Fig. 1) the electron-escape rate is

$$R_1(\varepsilon_1) = -\frac{f_1(\varepsilon_1)}{\tau_{1out}} \tag{2.16}$$

where τ_{1out} is the electron-escape time from the subband due to various types of scattering mechanisms. In these present work we take into account only LO-phonon assistant tunneling that is typically the most prominent scattering process, so that

$$R_1(\varepsilon_1) = -(2N_0+1)\frac{f_1(\varepsilon_1)}{\tau_1} \tag{2.17}$$

here τ_1 is the interwell scattering time due to a spontaneous LO-phonon emission. The nonradiative time τ_1 can be tuned by changing the design parameters of the QW's and barriers. To achieve the efficient drain of electrons from subband E_1 the designed structure must be such that the subband energy difference $E_1 - E_1^*$ is close to LO-phonon energy. For the particularly designed structure of the LO-phonon tunneling, the calculated time constant τ_1 in GaAs/$Al_xGa_{1-x}As$ DQW heterostructure[3] is in a range of 0.4–1.0 ps depending upon the coupling strength between the electronic states of the two subbands E_1 and E_2. However, in our present paper it is regarded as a tuneable parameter to determine the global population ratio between E_1 and E_2 subbands.

For subband E_2 the electron $R_2(\varepsilon_i)$ can be determined by intersubband LO-phonon-assistant scattering from the subband E_2 down to subband E_1, neglecting any other scattering mechanisms from the subband. Therefore, the electron escape is

$$R_2(\varepsilon_2) = -(2N_0+1)\frac{f_2(\varepsilon_2)}{\tau_{12}}, \tag{2.18}$$

where τ_{12} is the intrawell scattering time due to a spontaneous LO-phonon emission from subband E_2 down to subband E_1. The typical nonradiative time τ_{12} in GaAs QW $\sim$ 1 ps for midinfrared regime of operation.[19,20]

Electron generation processes. The term $G_i(\varepsilon_i)$ describes the electron generation in subband E_i For the lower subband the electron generation $G_1(\varepsilon_1)$ can be obtained from the intersubband scattering rates of electron from the upper subband

$$G_1(\varepsilon_1) = \frac{1}{\tau_{12}}\frac{m_2}{m_1}[(N_0+1)f_2(\varepsilon_1 - \hbar\Omega_0 + \hbar\omega_0) + N_0 f_2(\varepsilon_1 - \hbar\Omega_0 - \hbar\omega_0)] \tag{2.19}$$

where $\hbar\Omega_0 = E_2(0) - E_1(0)$ is the energy separation between the two subbands. The first term is responsible for the emission of LO phonons, while the latter term stands for the absorption of LO phonons.

Electron generation $G_2(\varepsilon_2)$ in the upper subband is assumed as monochromatic pumping based on these following reasons.

(i) For a strong nonparabolic material the 2D electron gas (2DEG) in the emitter is permitted to tunnel through the upper subband E_2 in QW1; see also Fig. 1(a), only for a definite wave vector k with a definite kinetic energy ε_2.

(ii) Similarly, for the case of optical pumping only the photoelectrons with a definite wave vector **k** are allowed to be pumped into the subband E_2. This is equivalent to requiring the definite kinetic energy ε_2 to be pumped into the subband.

(iii) The third main reason is that the model kinetic equation in our approach is linear. This implies that if one can find its solution with a δ-function pumping, one will be able to build up the convolution of general problems with arbitary generation function.

Consequently, the electron generation in the upper subband is therefore

$$G_2(\varepsilon_2) = \frac{G_0}{\rho_2}\delta(\varepsilon_2 - \varepsilon_0), \tag{2.20}$$

where G_0 is the number of electrons with kinetic energy ε_0, and $\rho_2 = m_2/(\pi\hbar^2)$ is the 2D density of states in the subband E_2.

By substituting all of these relevant scattering terms given in Eqs. (2.3)–(2.20) into the kinetic equation, Eq. (2.1), under a steady state of operation, we obtain

$$\frac{\hbar\omega_0}{\tau_{ee}}\left[\frac{d}{d\varepsilon_i} + T_e\frac{d^2}{d\varepsilon_i^2}\right]f_i(\varepsilon_i) - \gamma(\varepsilon_i)f_i(\varepsilon_i) + B_i(\varepsilon_i) + R_i(\varepsilon_i) = -G_i(\varepsilon_i), \tag{2.21}$$

here $T_e = D_{ee}(\varepsilon_i)/A_{ee}(\varepsilon_i)$ is the electron temperature in a 2D electrons below LO-phonon threshold. It follows from the principle of detailed balance as 2DEG below the LO-phonon threshold represents a thermal bath with temperature T_e.

In addition to the dimensionless parameter $\eta = \tau_0/\tau_{ee}$, we introduce $\xi_1 = \tau_0/\tau_1$, $\xi_2 = \tau_0/\tau_{12}$, $\theta = T_e/(\hbar\omega_0)$ and $y_i = \varepsilon_i/(\hbar\omega_0)$. The ratio ξ_1/ξ_2 characterizes the global population ratio between the two subbands involved. The dimensionless parameter θ determines the ratio of electron temperature to LO-phonon energy. In our approach it is always assumed to be small. As a result of substituting these dimensionless parameters into the kinetic equation, Eq. (2.21), we can obtain a four dimensionless kinetic equation system to get rid of the step function Θ, that takes into account LO-phonon threshold, as follows:

For the upper subband E_2.
(a) $0<y_2<1$;

$$\eta\theta\frac{d^2f_2(y_2)}{dy_2^2}+\eta\frac{df_2(y_2)}{dy_2}+(N_0+1)f_2(y_2+1)-\alpha_2 f_2(y_2)$$
$$=-P_0\delta(y_2-y_0) \tag{2.22}$$

(b) $y_2>1$;

$$\eta\theta\frac{d^2f_2(y_2)}{dy_2^2}+\eta\frac{df_2(y_2)}{dy_2}+(N_0+1)f_2(y_2+1)$$
$$+N_0f_2(y_2-1)-\beta_2 f_2(y_2)=0 \tag{2.23}$$

For the lower subband E_1.
(a) $0<y_1<1$;

$$\eta\theta\frac{d^2f_1(y_1)}{dy_1^2}+\eta\frac{df_1(y_1)}{dy_1}+(N_0+1)f_1(y_1+1)-\alpha_1 f_1(y_1)$$
$$=0 \tag{2.24}$$

(b) $y_1>1$;

$$\eta\theta\frac{d^2f_1(y_1)}{dy_1^2}+\eta\frac{df_1(y_1)}{dy_1}+(N_0+1)f_1(y_1+1)$$
$$+N_0f_1(y_1-1)-\beta_1 f_1(y_1)=-P_1(y_1) \tag{2.25}$$

where $\alpha_{1,2}=N_0+\xi_{1,2}(2N_0+1)$, $\beta_{1,2}=(2N_0+1)(1+\xi_{1,2})$, $P_0=\tau_0 G_0/(\rho_2\hbar\omega_0)$ and

$$P_1(y_1)=\xi_2\left(\frac{m_2}{m_1}\right)\left[(N_0+1)f_2\left(y_1+1-\frac{\hbar\Omega_0}{\hbar\omega_0}\right)\right.$$
$$\left.+N_0f_2\left(y_1-1-\frac{\hbar\Omega_0}{\hbar\omega_0}\right)\right].$$

The details of mathematical solution of Eqs. (2.22)–(2.25) are presented in the Appendix where boundary conditions for these equations are also presented. In the following section we present the resulting solutions of the kinetic equation system for various values of the relevant parameters η,ξ_1,ξ_2, and θ that correspond to different regemes of the QCL operation.

III. SUBBAND DISTRIBUTION FUNCTIONS

In this section our investigations are mainly focused on the nonequilibrium behavior of electrons in the GaAs/$Al_xGa_{1-x}As$ DQW heterostructure shown in Fig. 1. We introduce a universal dimensionless energy variable $y \equiv y_2=\varepsilon_2/(\hbar\omega_0)$ for the subband distribution functions $f_1(y_1)$ and $f_2(y)$; here $y_1=\varepsilon_1/(\hbar\omega_0)=(m_2/m_1)y$. This variable conserves at optical transitions from E_2 to E_1. The calculated subband distribution functions for different values of η, which determine electron concentrations, are shown in Fig. 2. With increasing values of η; i.e., increasing the concentrations of electrons, the subband distribution functions

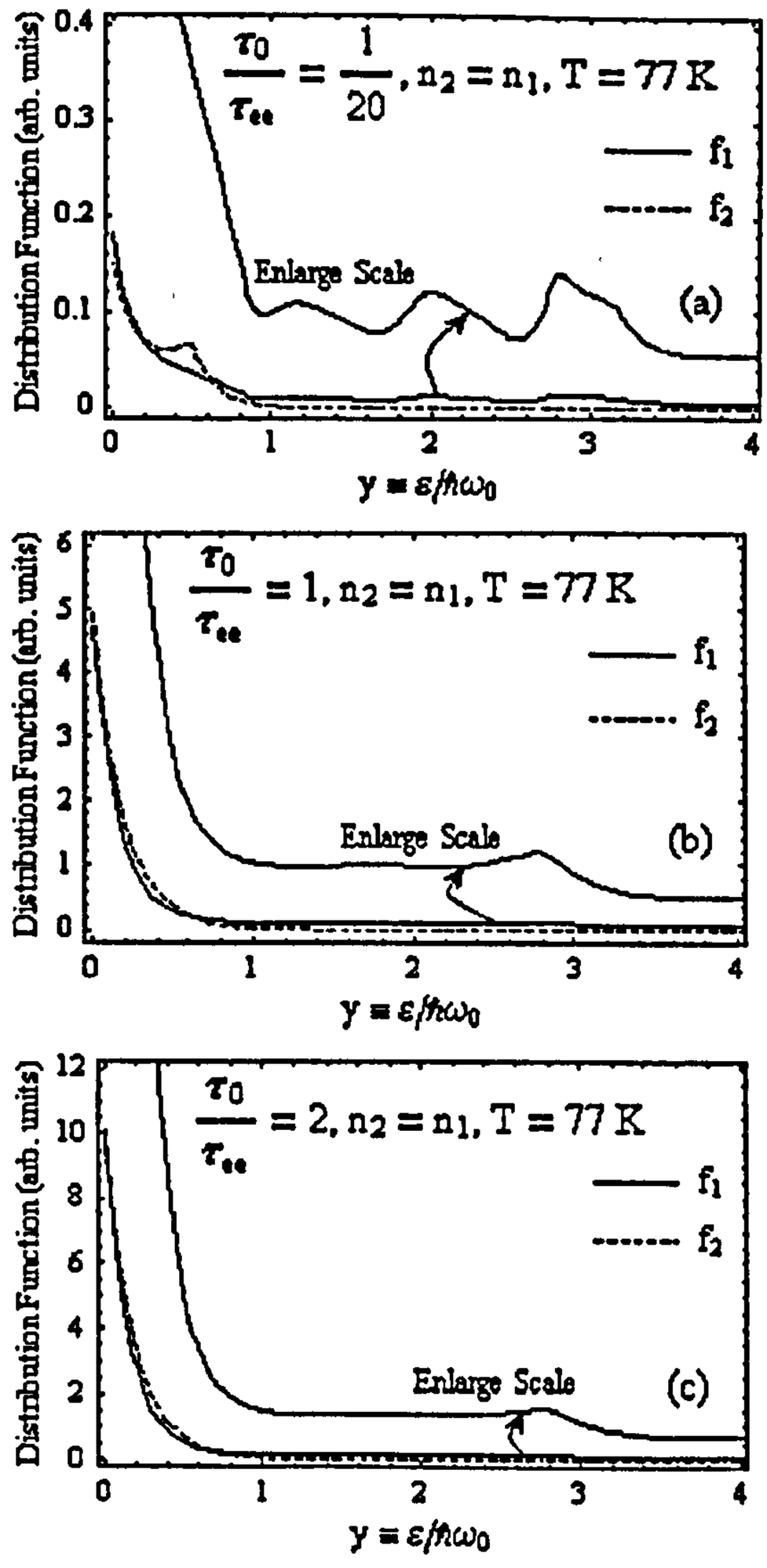

FIG. 2. Subband distribution functions for the monochromatic pumping $P(y)=P_0\delta(y-\frac{1}{2})$ into the upper subband E_2 with equal subband population $n_2=n_1$; assuming the following parameters: $\tau_0=0.1$ ps, $\tau_{12}=\tau_1=1$ ps, the subband separation energy $\hbar\Omega_0=155$ meV, and $m_2=1.2m_1$, at temperature $T=77$ K for different values of η: (a) 0.05, (b) 1 and (c) 2.

below LO-phonon threshold ($y<1$) in both subbands become close to Maxwellian distributions. In the region above LO-phonon threshold ($y>1$), the shape of the upper subband distributions $f_2(y)$ is still close to Maxwellian while for the lower subband the distributions $f_1(y)$ are always strongly nonequilibrium and deviate far from Maxwellian.

At a very low electron-concentration limit, $n_s \ll 1.0\times10^{11}$ cm^{-2}; i.e., $\eta\ll1$, where the dominant scattering process is due to LO phonons causing electronic transitions within the same subband. The calculated distributions for $\eta=0.05$ and so far $n_s=1.92\times10^{10}$ cm^{-2} at different temperature $T=77$ K and 300 K (see Figs. 2 and 3); here we assume that $T=T_e=T_L$, which shows that the shape of the distribu-

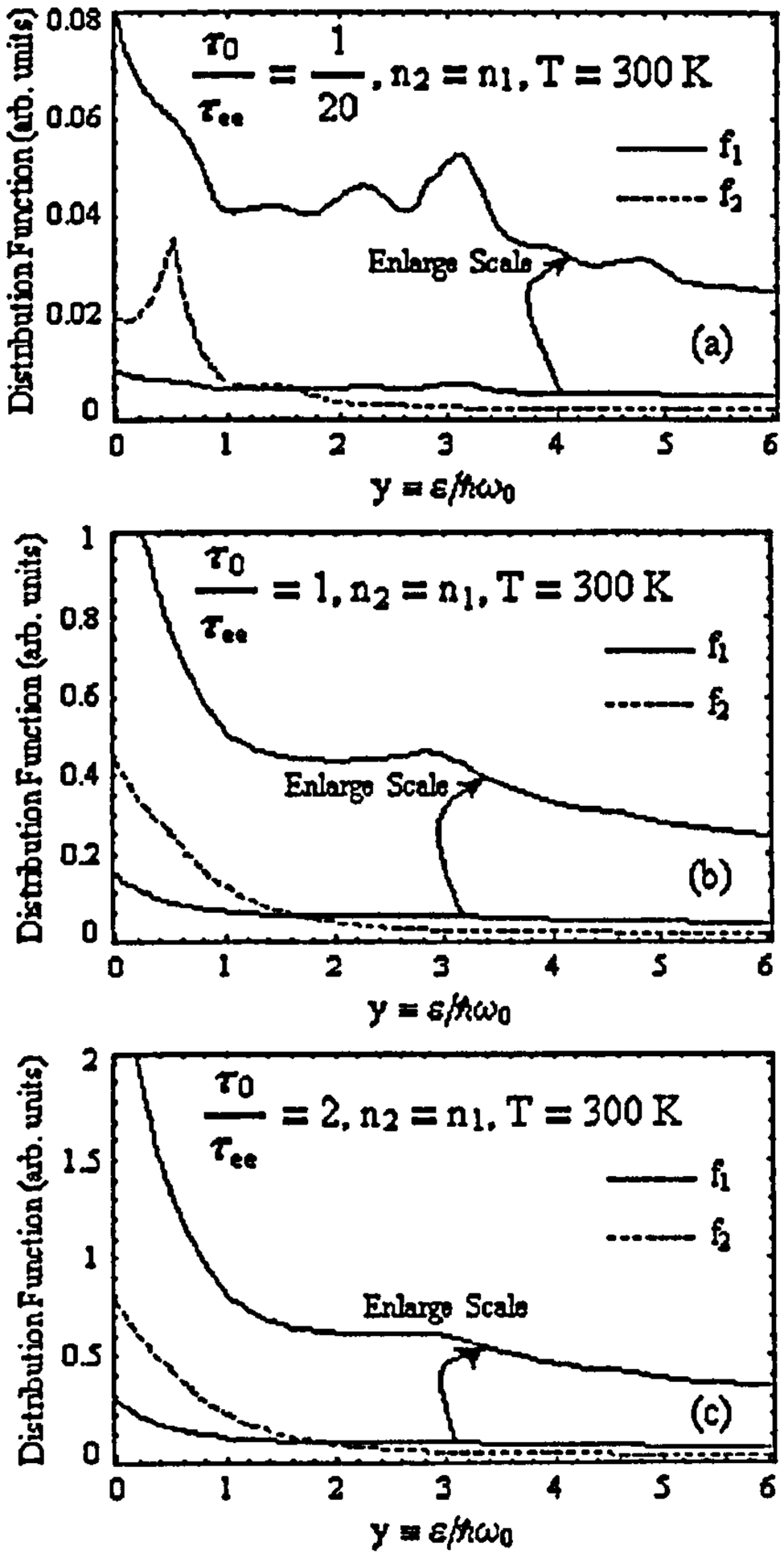

FIG. 3. Subband distribution functions for the monochromatic pumping $P(y)=P_0\delta(y-\frac{1}{2})$ into the upper subband E_2 with equal subband population $n_2=n_1$; assuming the following parameters: $\tau_0=0.1$ ps, $\tau_{12}=\tau_1=1$ ps, the subband separation energy $\hbar\Omega_0=155$ meV, and $m_2=1.2m_1$, at temperature $T=300$ K for different values of η: (a) 0.05, (b) 1 and (c) 2.

tion functions in both subbands deviates far from Maxwellian. In the upper subband they have a pronounced peak at the pumping energy affected by the monochromatic electron-generation process that plays an essential role in this regime of operation. Immediately after a nonradiative intersubband transition from the upper subband E_2 down to the lower subband E_1, the lower subband electrons are in a state of high kinetic energy $\varepsilon_1=\hbar\Omega_0+\varepsilon_2\pm\hbar\omega_0$. Consequently, they cascade down to the subband bottom by emitting LO phonons resulting in the distribution functions $f_1(y)$ at steady-state being strongly nonequilibrium. For $\eta=0.05$ at temperature $T=77$ K we can see four pronounced peaks on the lower subband distribution function $f_1(y)$. However, its shape deviates far from the shape of $f_2(y)$ at low energies. At $\eta=1$ all peaks are completely smeared out, but the massive shoulder below main peak always remains.

In Fig. 3 we present the electron distributions calculated for the system with the same parameters as in Fig. 2, but operating at room temperature $T=300$ K. Our investigations focus on the distribution functions affected by the thermal phonon population N_0, which governs the lattice temperature T_L. By comparing the resulting calculations for a specific value of η at different operating temperatures $T=77$ K and 300 K. It is cleary seen that the nonequilibrium electron behavior is strongly dependent on the lattice temperature. The main interests of these resulting calculations as shown in Fig. 2 and 3 are addressed to the case $\xi_1/\xi_2=1$. The results show that it is possible to achieve positive values of the spectral gain $g(\Omega)$ due to the existence of local population inversions at some definite kinetic energies ε_2; i.e., at some particular electron wave vectors k, in the region below the LO-phonon threshold that provide an essential contribution to the spectral gain density. This implies that it is possible to achieve laser action even in low electron-concentration regimes of high-temperature operation; see also Fig. 3(a).

IV. SPECTRAL DENSITY OF GAIN

In a natural limit that the transverse phase relaxation rate $\gamma(\varepsilon)$ is much smaller than the optical frequency Ω, optical gain spectra $g(\Omega)$ can be expressed as a functional on the subband distribution function $f_1(\varepsilon_1)$ and $f_2(\varepsilon\equiv\varepsilon_2)$ (Refs. 5 and 6)

$$g(\Omega)=\frac{4e^2|z_{12}|^2m_2\Omega}{\hbar^3ac\sqrt{\kappa_\infty}}\int_0^\infty d\varepsilon\frac{\gamma(\varepsilon)[f_2(\varepsilon)-f_1(\varepsilon_1)]}{[\Omega-\Omega_k(\varepsilon)]^2+[\gamma(\varepsilon)]^2}, \tag{4.1}$$

where z_{12} is the transition matrix element, κ_∞ the dielectric permittivity at high frequency, a the QW1 width, and c the speed of light. The vertical transitions with articular $\hbar\Omega_k(\varepsilon)$, see also Fig. 1, are given by

$$\hbar\Omega_k(\varepsilon)=\hbar\Omega_0+\varepsilon-\varepsilon_1=\hbar\Omega_0-\left(\frac{m_2}{m_1}-1\right)\varepsilon \tag{4.2}$$

According to the threshold nature of $\gamma(\varepsilon)$ that has been discussed in Sec. II the optical gain becomes strongly influenced by the nonequilibrium distributions in the two subbands. Gain spectra calculated for diferent values of the competition parameter η between e-e scattering and electron-LO-phonon scattering; in different values of the electron concentrations, are shown in Fig. 4. For this calculation we assume equal global population ratio that corresponds to $\tau_{12}=\tau_1$; i.e. $\xi_1/\xi_2=1$. The resulting calculations show that we can achieve strong positive gain for particular photon energies. Small values of η, that correspond to low overall-electron concentrations, give proportionally smaller gain amplitudes. In addition, the shapes of the spectral curves are affected by the shapes of the particular distribution functions involved. At $\eta>1/3$ the main reason for positive gain is the leverage of f_2 above f_1 below LO-phonon energy that corresponds to the photon-energy interval from $\hbar\Omega_0-\hbar\omega_0[(m_2/m_1)-1]$ to $\hbar\Omega_0$. The smaller photon energies correspond to large kinetic energies at both subbands,

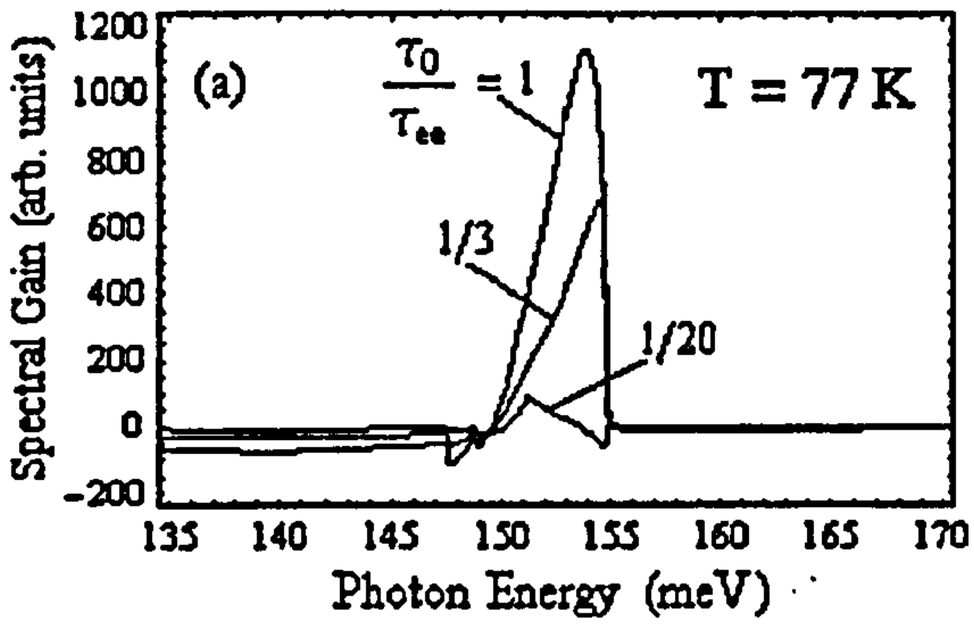

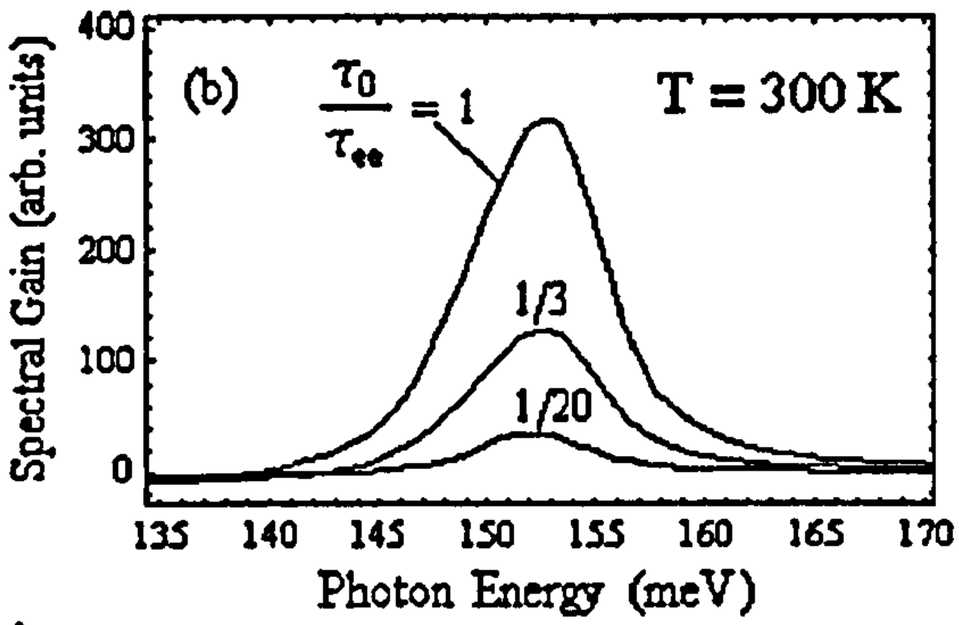

FIG. 4. Variations of gain spectra under the monochromatic pumping $P(y)=P_0\delta(y-\frac{1}{2})$ into the upper subband E_2 with equal subband population $n_2=n_1$; assuming the following parameters: $\tau_0=0.1$ ps, $\tau_{12}=\tau_1=1$ ps, the subband separation energy $\hbar\Omega_0=155$ meV, and $m_2=1.2m_1$, for different values of $\eta=0.05,1/3$, and 1 at different temperatures: (a) 77 K and (b) 300 K.

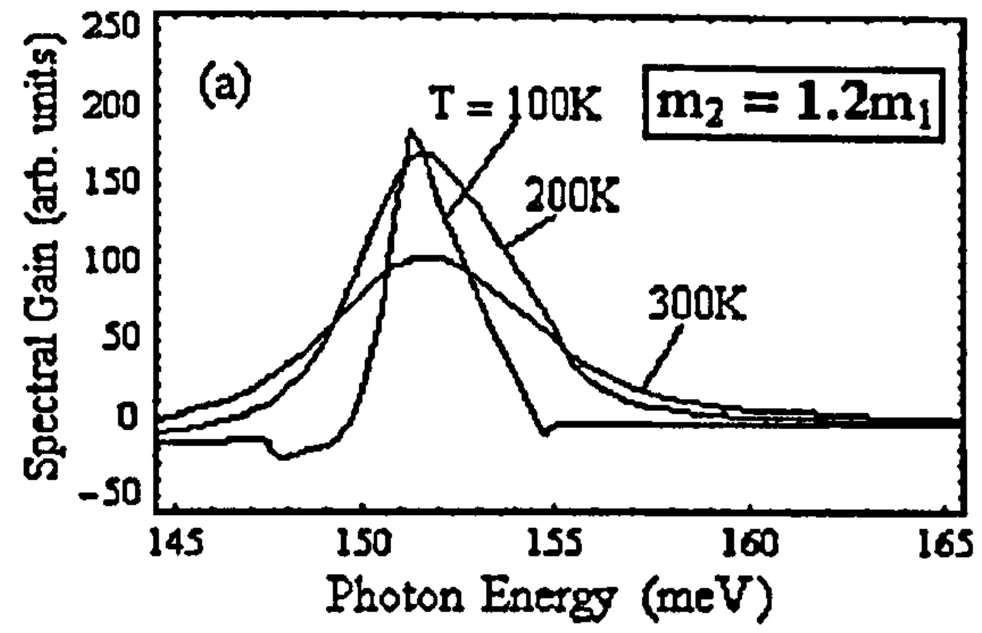

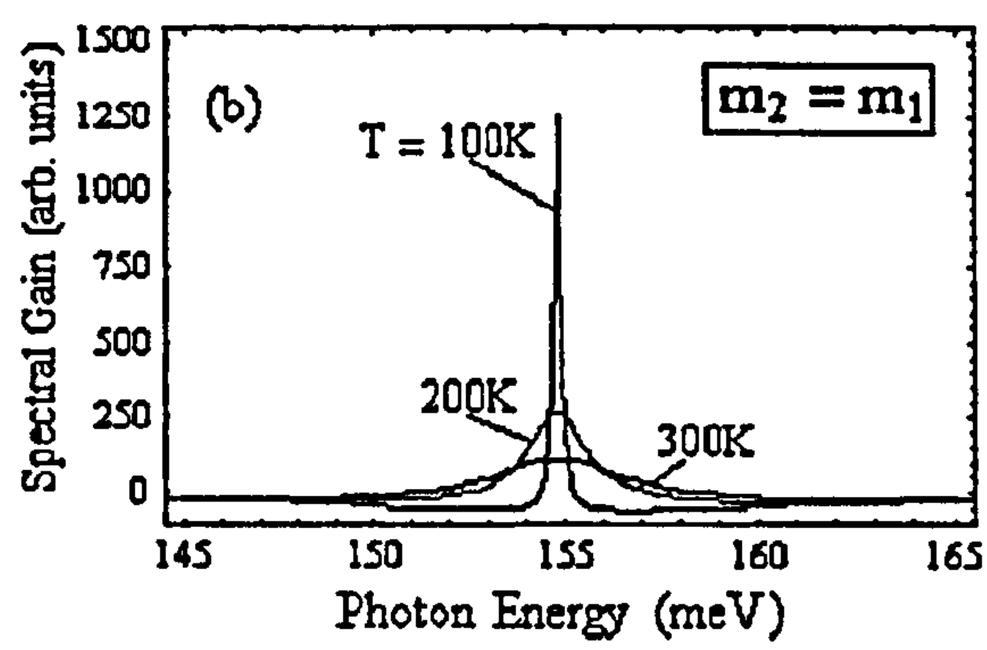

FIG. 5. Gain spectra in low-concentration limits at different operating temperatures ranging from 100 to 300 K under the monochromatic pumping $P(y)=P_0\delta(y-\frac{1}{2})$ into the upper subband E_2 with equal subband population $n_2=n_1$. (a) Assuming the following parameters: $\tau_0=0.1$ ps, $\tau_{12}=\tau_1=1$ ps, $\tau_{ee}=2$ ps, the subband separation energy $\hbar\Omega_0=155$ meV, and $m_2=1.2m_1$. (b) Same spectra calculated in the parabolic model, $m_2=m_1$.

and the optical gain becomes negative in this region. At room temperature $T=300$ K the maximum values of gain strongly decreases because the amplitude of the peak near pumping energy decreases when temperature increases. At the bottom subband E_1, more electrons are above LO threshold and so far less electrons below the LO threshold. Furthermore, the transverse phase relaxation rate $\gamma(\varepsilon)$ becomes substantially larger so that it smears out the fine structure of the spectral gain function at smaller η.

In Fig. 5 we present gain spectra calculated in a low-concentration limit, $\eta=0.05$; i.e. $n_s=1.92\times10^{10}$ cm^{-2}, at different temperatures. Resulting calculations show that the amplitude of gain is not strongly dependent upon temperature in the nonparabolic model while in the parabolic model it has a strong temperature dependence.

Gain spectra calculated for different values of $\xi_1/\xi_2=1,2$, and 4 (see Fig. 6) that correspond to global inversion population $n_2/n_1=1,2$, and 4, respectively, are also investigated at low- and high-electron-concentration regimes of operation that correspond to $\eta=0.05$ and 1. Our results show that the spectral density of gain is mainly sensitive to the upper subband distribution function $f_2(\varepsilon)$. For $n_2>n_1$ at small η that corresponds to low-electron-concentration regimes two peaks are observed. First peak corresponds to the photon emission from the bottom of E_2 subband, and second peak tp the optical transitions near the initial pumping point. At $\eta=1$ the second peak completely vanishes, we also note that even at $\eta=0.05$ first peak always has larger amplitude.

V. CONCLUSIONS

We have solved analytically the kinetic equations, Eqs. (2.22)–(2.25) for subband distribution functions at various values of η ranging from 0.05 to 2 that correspond to electron concentrations ranging from 1.92×10^{10} cm^{-2} to 7.68×10^{11} cm^{-2}. At small η, shapes of the distribution functions in both subbands deviate strongly from Maxwellian. In the upper subband they have a pronounced peak at the pumping energy affected by the monochromatic electron-generation process that plays an essential role in this regime of operation. Immediately after nonradiative intersubband transitions from the upper subband E_2 down to the lower subband E_1, the lower subband electrons are at high-kinetic-energy states $\varepsilon_1=\hbar\Omega_0+\varepsilon_2\pm\hbar\omega_0$. Consequently, they cascade down to the subband bottom by emitting LO phonons resulting in the distribution functions $f_1(\varepsilon_1)$ at steady-state being strongly nonequilibrium. At larger η all peaks are completely smeared out, and these distribution functions become close to Maxwellian. Detailed shapes of these distribution functions are essential for the derivation of energy balance equation and calculation of gain in the intersubband

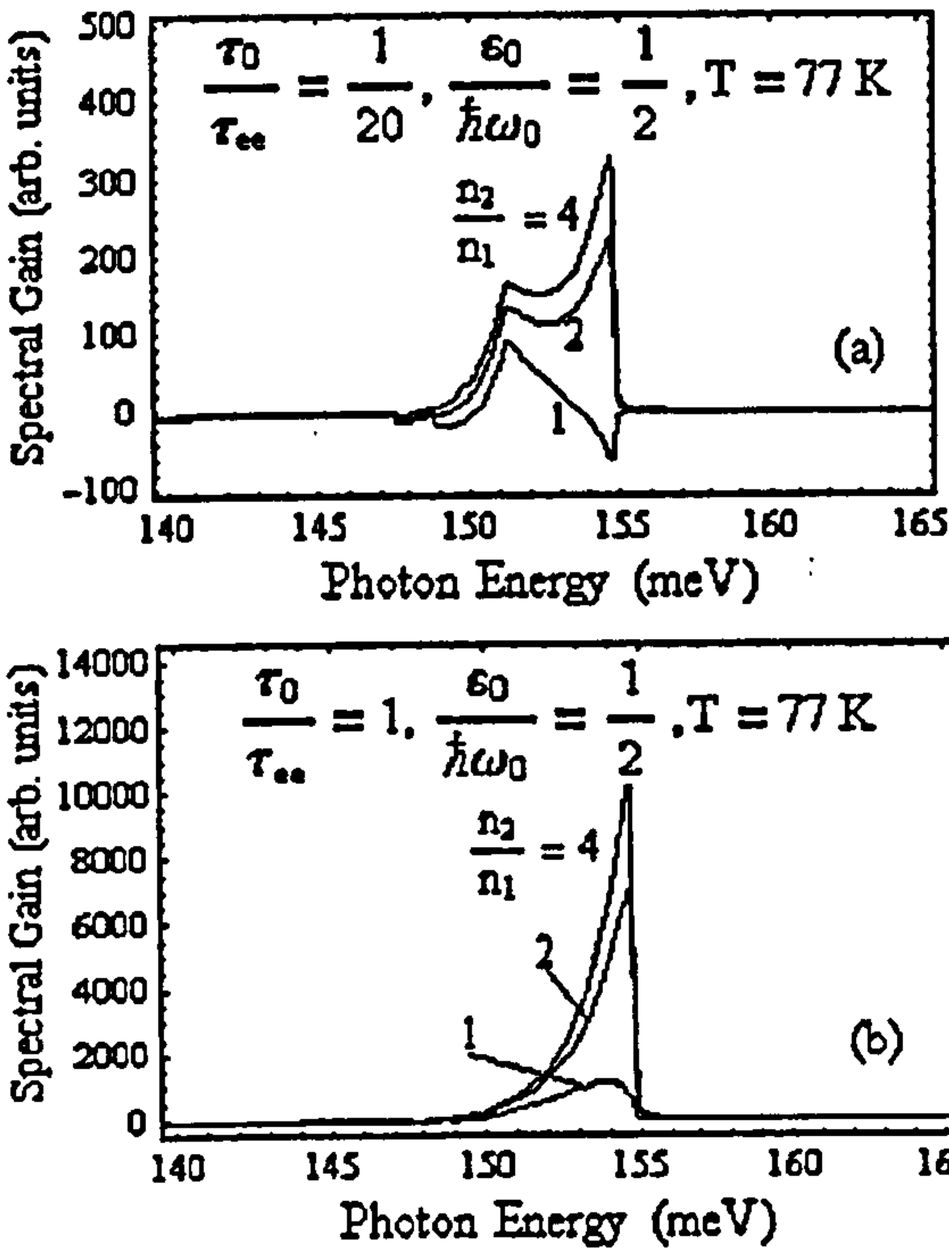

FIG. 6. Gain spectra at operating temperatures $T=77$ K for different subband population ratios $n_2/n_1=1$, 2, and 4 under the monochromatic pumping $P(y)=P_0\delta(y-\frac{1}{2})$ into the upper subband E_2; assuming the following parameters: $\tau_0=0.1$ ps, the subband separation energy $\hbar\Omega_0=155$ meV, and $m_2=1.2m_1$ at low- and high-electron-concentration regimes of operation that correspond to $\eta=0.05$ (b) and $\eta=1$ (b), respectively.

lasers. Similar results have been established in Ref. 10. Unfortunately, it is quite difficult to make a direct comparison with our calculations. However, the Monte Carlo simulations also confirm that below LO threshold the shape of the electron distributions are closely Maxwellian, and phonon replicas survive better at low electron concentration.

An advantage of our approach is that it is more convenient to build up the model to investigate kinetics of electrons scattering in other similar considerate systems by changing the relevant controlling parameters. However, there are some limitations of this model and for real device modeling that we have to take into account the following effects.

(i) All temperatures T_e, T_L and LO-phonon temperature T_{ph} are assumed to be the same for all cases considered in this paper. However, in real devices they might be different in some particular regimes of operation. For accurate calculations we have to evaluate T_e from the energy balance equation. Incoming energy depends on the electron generation G_0 while the energy losses depend on both distribution functions f_1 and f_2. The resulting equation gives θ as a function of η, ξ_1 and ξ_2. Also, at high electron concentrations LO-phonon distribution function differs from N_0. As we need only $N(\hbar\omega_0)$, in our equations this can be done by using the effective temperature T_{ph} that differs from T_L. The effective temperature T_{ph} depends on the generation rates G_0 and the running away rates of phonons from the QW region.

(ii) In our approach A_{ee} is a constant throughout the energy range. In fact, this assumption works well only for $\varepsilon \gg T_{ee}$ while at $\varepsilon \sim T_{ee}$ A_{ee} is getting smaller. However, if electron distributions are Maxwellian or Fermi, it particular value of A_{ee} is not important because there is none of LO phonon getting involved in this region.

(iii) At very high electron concentrations that correspond to $\eta \gg 1$, A_{ee} becomes sensitive to the exact-distribution functions. As a result, it reduces the accuracy of our calculations if we still use the assumption that A_{ee} is constant in these regimes of operation. However, our main interest is directed to investigate the system at $\eta \leqslant 1$ where A_{ee} is not very sensitive to the exact shapes of these distribution functions.

(iv) The assumption that the dominant e-e scattering processes of a minority of high kinetic-energy electrons is only due to the scattering on the majority of quasithermalized electrons, in general, is not valid if the distribution function differs from a Maxwellian. However, in the reality we actually have $T_e \ll \hbar\omega_0$. This is enough to have $\exp(-\hbar\omega_0/T_e) \ll 1$ to fulfill our approach.

(v) At very low electron concentrations that correspond to $\eta \ll 1$, the ratio $D_{ee}/A_{ee}=T_e$ is not valid due to the difficulty of electron to form a thermalized bath. In this case we have to calculate D_{ee} independently and use the resulting $T_e = D_{ee}/A_{ee}$ as the definition of electron temperature.

(vi) The Fokker-Planck-Landau approximation does not work well at the regions $|\varepsilon-\varepsilon_0| \ll T_e$. The reason is that for 2DEG all scattering angles are equally important for energy transfer. To take all these events into account one has to consider the integral equation, Eq. (2.9) instead of Eqs. (2.22)–(2.25). However, the resulting gain is not very sensitive to exact shapes of the distribution functions near pumping point. In reality, the pumping is not an exact δ-function shape due to nonhomogeneous broadening.

ACKNOWLEDGMENTS

The work has been supported by EPSRC(UK) Grant No. GR/M91044. S.K. would like to specially thank the Royal Thai Government for financial support. We are grateful to L. R. Wilson, J. W. Cockburn and Professor G. Rees for useful discussions. In addition, we would like to thank Professor M. S. Skolnick for his support.

APPENDIX

To solve the model equation given in Eq. (2.21) we first introduce dimensionless parameters; $\eta=\tau_0/\tau_{ee}$, $\xi_1=\tau_0/\tau_1$, $\xi_2=\tau_0/\tau_{12}$, $\theta=T_e/(\hbar\omega_0)$, and $y_i=\varepsilon_i/(\hbar\omega_0)$, and Eq. (2.21) is then transformed to the dimensionless kinetic equation as follows.

a. For the upper subband E_2

(a) $0<y<1$;

$$\eta\theta\frac{d^2f_2(y)}{dy^2}+\eta\frac{df_2(y)}{dy}+(N_0+1)f_2(y+1)-\alpha_2 f_2(y)$$
$$=-P_0\delta(y-y_0) \quad \text{(A1)}$$

(b) $y>1$;

$$\eta\theta\frac{d^2f_2(y)}{dy^2}+\eta\frac{df_2(y)}{dy}+(N_0+1)f_2(y+1)+N_0f_2(y-1)$$
$$-\beta_2 f_2(y)=0, \quad \text{(A2)}$$

where $y=y_2$, $\alpha_2=N_0+\xi_2(2N_0+1)$, $\beta_2=(2N_0+1)(1+\xi_2)$, and $P_0=\tau_0 G_0/(\rho_2\hbar\omega_0)$.

The kinetic equations given in Eqs. (A1) and (A2) can be solved by assuming the general solution $f_2(y)$ in the form

$$f_2(y)=f_2^{(0)}(y)+\frac{1}{\sqrt{2\pi}}\int_{-\infty}^{+\infty}dk e^{-iky}D_2(k)\varphi_2^{(0)}(k), \quad \text{(A3)}$$

$$D_2(k)=[-\eta\theta k^2-\eta k+(N_0+1)e^{-ik}+N_0e^{ik}-\beta_2]^{-1}, \quad \text{(A4)}$$

$$\varphi_2^{(0)}(k)=-\frac{1}{\sqrt{2\pi}}\int_{-\infty}^{+\infty}dy e^{iky}D_2(k)f_2^{(0)}(y-1), \quad \text{(A5)}$$

where $f_2^{(0)}(y)$ is the zeroth-order solution given as follows.

$$f_2^{(0)}(y)=\begin{cases}A_1e^{\mu_2^- y}+A_2e^{\mu_2^+ y}, & 0<y<y_0\\ A_3e^{\mu_2^- y}+A_4e^{\mu_2^+ y}, & y_0<y<1\\ A_5e^{\lambda_2 y}, & y>1.\end{cases} \quad \text{(A6)}$$

where

$$\mu_2^{\mp}=\frac{-\eta\mp\sqrt{\eta^2+4\eta\theta\alpha_2}}{2\eta\theta}$$

and

$$\lambda_2=\frac{-\eta-\sqrt{\eta^2+4\eta\theta\beta_2}}{2\eta\theta}.$$

The arbitary constants A_1-A_5 are obtained from the following boundary conditions.

(i) at $y=0$;

$$J_{ee}(y)|_{y=0}=0\rightarrow\left[\theta\frac{df_2(y)}{dy}+f_2(y)\right]_{y=0}$$

(ii) at $y=y_0$;

$$f_2(y)|_{y=y_0^+}=f_2(y)|_{y=y_0^-},$$

and

$$\eta\theta\left[\frac{df_2(y)}{dy}\bigg|_{y=y_0^+}-\frac{df_2(y)}{dy}\bigg|_{y=y_0^-}\right]=P_0$$

(iii) at $y=1$;

$$f_2(y)|_{y=1^+}=f_2(y)|_{y=1^-},$$

and

$$\frac{df_2(y)}{dy}\bigg|_{y=1^+}=\frac{df_2(y)}{dy}\bigg|_{y=1^-}$$

b. For the lower subband E_1

(a) $0<y_1<1$;

$$\eta\theta\frac{d^2f_1(y_1)}{dy_1^2}+\eta\frac{df_1(y_1)}{dy_1}+(N_0+1)f_1(y_1+1)-\alpha_1 f_1(y_1)$$
$$=0 \quad \text{(A7)}$$

(b) $y_1>1$;

$$\eta\theta\frac{d^2f_1(y_1)}{dy_1^2}+\eta\frac{df_1(y_1)}{dy_1}+(N_0+1)f_1(y_1+1)$$
$$+N_0f_1(y_1-1)-\beta_1 f_1(y_1)=-P_1(y_1), \quad \text{(A8)}$$

where $\alpha_1=N_0+\xi_1(2N_0+1)$, $\beta_1=(2N_0+1)(1+\xi_1)$, and

$$P_1(y_1)=\xi_2\left(\frac{m_2}{m_1}\right)\left[(N_0+1)f_2\left(y_1+1-\frac{\hbar\Omega_0}{\hbar\omega_0}\right)+N_0f_2\left(y_1-1-\frac{\hbar\Omega_0}{\hbar\omega_0}\right)\right]$$

General solution of the kinetic equations given in Eqs. (A7) and (A8) can be written in the form

$$f_1(y_1)=\begin{cases}B_1e^{\mu_2^- y}+B_2e^{\mu_2^+ y}+F_1(y_1), & 0<y_1<1\\ B_3e^{\lambda_1 y_1}+F_1(y_1), & y_1>1.\end{cases} \quad \text{(A9)}$$

$$F_1(y_1)=\frac{1}{\sqrt{2\pi}}\int_{-\infty}^{+\infty}dk e^{-iky_1}D_1(k)\varphi_1^{(0)}(k), \quad \text{(A10)}$$

$$D_1(k)=[-\eta\theta k^2-\eta k+(N_0+1)e^{-ik}+N_0e^{ik}-\beta_1]^{-1}, \quad \text{(A11)}$$

$$\varphi_1^{(0)}(k)=-\frac{1}{\sqrt{2\pi}}\int_{-\infty}^{+\infty}dy e^{iky_1}D_1(k)P_1(y_1), \quad \text{(A12)}$$

where

$$\mu_1^{\mp}=\frac{-\eta\mp\sqrt{\eta^2+4\eta\theta\alpha_1}}{2\eta\theta},$$

and

$$\lambda_1=\frac{-\eta-\sqrt{\eta^2+4\eta\theta\beta_1}}{2\eta\theta}.$$

The arbitary constants B_1-B_3 are obtained from the following boundary conditions.

(i) at $y_1=0$;

$$J_{ee}(y_1)|_{y_1=0}=0\rightarrow\left[\theta\frac{df_1(y_1)}{dy}+f_1(y_1)\right]_{y_1=0}$$

(ii) at $y_1=1$;

$$f_1(y_1)|_{y_1=1+}=f_1(y_1)|_{y_1=1-},$$

and

$$\left.\frac{df_1(y_1)}{dy_1}\right|_{y_1=1+}=\left.\frac{df_1(y_1)}{dy_1}\right|_{y_1=1-}.$$

[1] J. Faist, F. Capasso, D.L. Sivco, A.L. Hutchinson, and A.Y. Cho, Science **264**, 553 (1994).

[2] Y.B. Li, J.W. Cockburn, J.P. Duck, M.J. Birkett, M.S. Skolnick, I.A. Larkin, M. Hopkinson, R. Grey, and G. Hill, Phys. Rev. B **57**, 6290 (1998).

[3] S. Khan-ngern and I.A. Larkin, Phys. Lett. A **266**, 209 (2000).

[4] J. Faist, F. Capasso, C. Sirtori, D.L. Sivco, A.L. Hutchinson, M.S. Hybertsen, and A.Y. Cho, Phys. Rev. Lett. **76**, 411 (1996).

[5] B. Gelmont, V.B. Gorfinkel, and S. Luryi, Appl. Phys. Lett. **68**, 2171 (1996).

[6] V.B. Gorfinkel, S. Luryi, and B. Gelmont, IEEE J. Quantum Electron. **32**, 1995 (1996).

[7] V.F. Elesin and A.V. Krasheninnikov, Physica A **241**, 386 (1997).

[8] P. Kinsler, P. Harrison, and R.W. Kelsall, Phys. Rev. B **58**, 4771 (1998).

[9] P. Lugli and S.M. Goodnick, Phys. Rev. Lett. **59**, 716 (1987).

[10] S.M. Goodnick and P. Lugli, Phys. Rev. B **37**, 2578 (1988).

[11] P. Lugli, P. Bordone, L. Reggiani, M. Rieger, P. Kocevar, and S.M. Goodnick, Phys. Rev. B **39**, 7852 (1989).

[12] S.E. Esipov and Y.B. Levinson, Zh. Eksp. Teor. Fiz. **90**, 330 (1986) [Sov. Phys. JETP **63**, 191 (1986)].

[13] S.E. Esipov and Y.B. Levinson, Adv. Phys. **36**, 331 (1987).

[14] J.H. Smet, C.G. Fonstad, and Q. Hu, J. Appl. Phys. **79**, 9305 (1996).

[15] P.J. Price, Phys. Rev. B **30**, 2234 (1984).

[16] V.F. Elesin and Yu.V. Kopaev, Zh. Eksp. Teor. Fiz. **108**, 2186 (1995) [JETP **81**, 1192 (1995)].

[17] I.A. Larkin, Fiz. Tekh. Poluprovodn. **23**, 1664 (1989) [Sov. Phys. Semicond. **23**, 1028 (1989)].

[18] E.M. Liftshitz and L.P. Pitaevskii, *Physical Kinetics* (Butterworth-Heinemann, Oxford, 1997), Vol. 10.

[19] M.C. Tatham, J.F. Ryan, and C.T. Foxon, Phys. Rev. Lett. **63**, 1637 (1989).

[20] F.H. Julien, Z. Moussa, P. Boucaud, Y. Lavon, A. Saar, J. Wang, J.P. Leburton, V. Berger, J. Nagle, and R. Planel, Superlattices Microstruct. **19**, 69 (1996).

21 February 2000

PHYSICS LETTERS A

ELSEVIER

Physics Letters A 266 (2000) 209–215

www.elsevier.nl/locate/physleta

Phonon-assisted tunnelling in double quantum well structures

S. Khan-ngern, I.A. Larkin *

Department of Physics & Astronomy, University of Sheffield, Sheffield, S3 7RH, UK

Received 1 December 1999; accepted 8 December 1999
Communicated by V.M. Agranovich

Abstract

We calculate the tunnelling rates for interwell transitions due to electron–longitudinal-optical phonon (LO-phonon) scattering in GaAs–AlGaAs DQW heterostructures starting from the Fröhlich interaction and Fermi's golden rule. The rates are investigated as functions of the difference in energy between the E_1 level of the wider quantum well (QW1) and the E_1^* level of the narrower quantum well (QW2). We also compare our calculations of the LO-phonon assisted tunnelling with the conventional resonant tunnelling.

PACS: 72.10. – d; 73.40.Gk; 73.50. – h

1. Introduction

Long wavelength semiconductor lasers are in demand for many industrial and research applications. The conventional interband transition approach requires narrow band-gap semiconductor materials for realising mid- and long-wavelength IR lasers. An alternative approach utilising intersubband transition in semiconductor quantum well structures for long wavelength IR lasers was first suggested in 1971 by Kazarinov and Suris [1]. In this structure coherent photons generated by electron transitions from one confinement state to another while holes are not involved. Thus, wavelength of intersubband lasers is determined, not by the band gap, but by the small energy separation of conduction subbands arising from quantum confinement in quantum well structures based on wider band-gap semiconductor materials. The first intersubband laser was not realised until the recent demonstration of a so-called quantum cascade laser (QCL) reported by Faist et al. [2]. The QCL, a unipolar device, utilises photon emission between subbands in a staircase of coupled AlInAs–GaInAs quantum wells, in which each injected electron is recycled, ideally producing an additional photon, as it cascades through each period of the active region. The most prominent obstacle to intersubband lasing is the nonradiative relaxation between subbands due to optical phonon scattering which will be discussed in Section 2. The typical phonon relaxation time is much smaller than the radiative time resulting in a very low radiative efficiency. However, specially designed multiple barrier heterostructures can provide population inversion without reducing the current injection efficiency.

In our previous work [3] we have demonstrated that to achieve inverted population in a triple barrier resonant tunnelling structure (TBRTS) we should

* Corresponding author. Tel.: +44-114-222-4353; fax: +44-114-272-8079.
E-mail address: i.larkin@sheffield.ac.uk (I.A. Larkin).

0375-9601/00/$ - see front matter
PII: S0375-9601(99)00877-4

ensure efficient drain of carriers from the lower subband. Transport through TBRTS also has been intensively theoretically [4–6] and experimentally [7–9] studied. The physics of resonant tunnelling in these systems is much more than an extension of the results of the double-barrier case [10,11], since the former now involves the coupling of quasi-bound states between two adjacent quantum wells in the semiconductor heterostructure. In most cases the experimental resonant position corresponds to theoretical predictions based on the 1D self-consistent theory of Poisson and Schrödinger equations. However, the amplitude and width of the peaks differ significantly from the 1D model [8]. This discrepancy arises from scattering processes which accompany the tunnelling processes and resulting in sequential tunnelling rather than coherent tunnelling. This was clearly demonstrated [7–9] in experiments with an application of strong magnetic field parallel to the current. These papers experimentally prove the essential role of LO-phonons which appeared to be a major reason for sequential tunnelling. Theoretically, the role of LO-phonon assisted tunnelling in resonant tunnelling was also intensively studied [7,10–12]. The main result for TBRTS shows that the resonant peak in I–V curve became wider and a satellite peak appears at LO-phonon energy. Unfortunately, Refs. [10–12] studied the 3D–2D–3D tunnelling case whereas for QCL structures it is necessary to study 2D–2D tunnelling to ensure effective drain from localised states.

Another LO-phonon assisted tunnelling approach comes from the studies of vertical transport in superlattices [13,14], where it was shown that the LO-phonon mechanism is the most efficient process for hopping conductivities. Tsu and Döhler [13] also point out that the transport in superlattices can be reduced to DQW problems. To deal with the DQW problem we need to evaluate the transfer integral for the system [14]. However, the calculation reported in Ref. [14] does not take into account the orthogonality of the initial and final states, as a result the transfer integral was calculated only from the exponentially small wavefunction overlap in the barrier. This problem has been resolved numerically by Weil and Vinter [15], and their result shows that the main overlap occurs in the well regions and not as a result of the interbarrier overlap. This approach has been generalised by Harrison [16], and Ferreira and Bastard [17]. The calculations [16,17] take into account

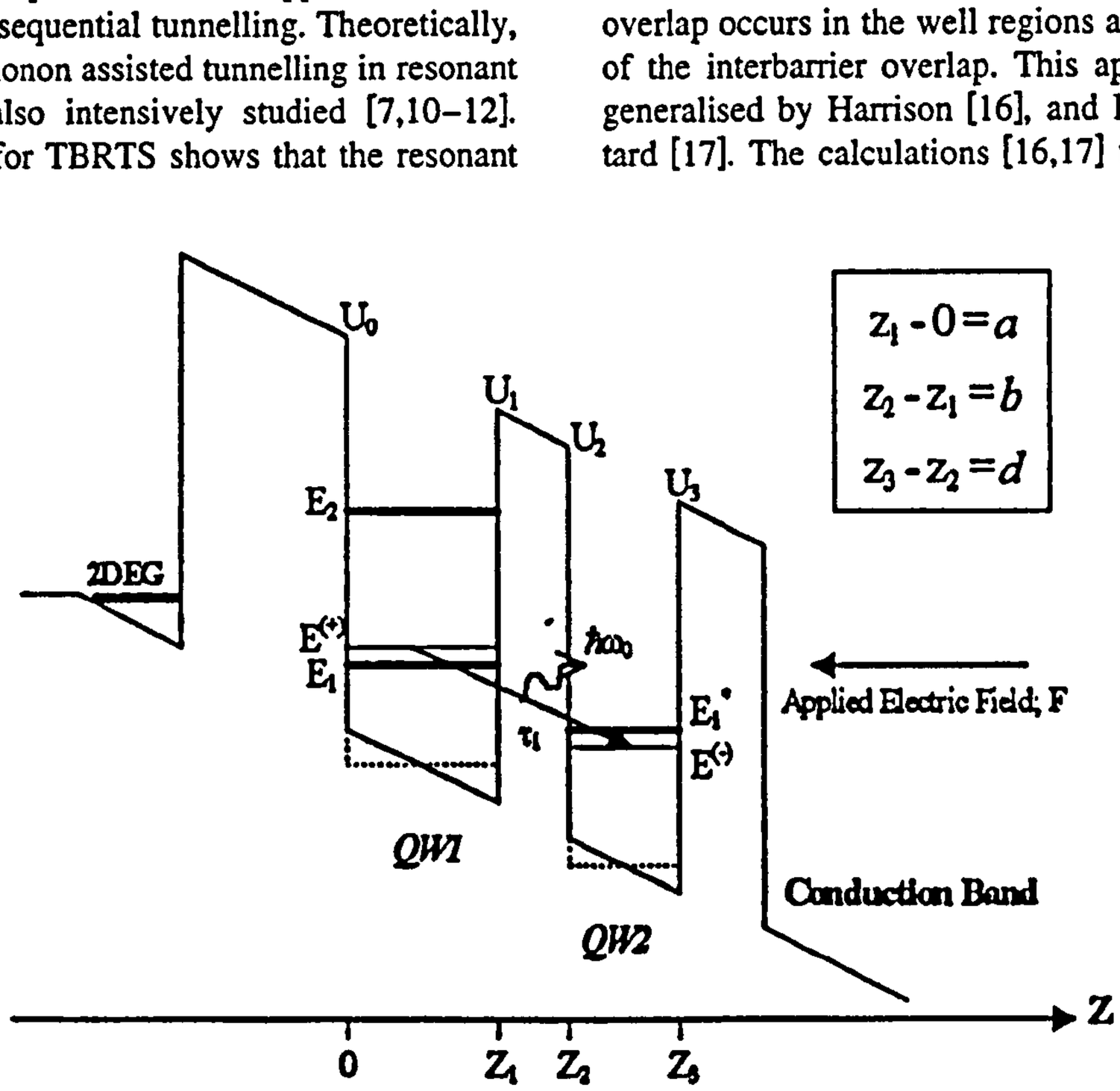

Fig. 1. Conduction band profile of the DQW structure with a wider well as a lasing unit and a narrower well as an electronic energy filter by tunnelling processes.

the slope of the conduction band in the heterostructure, which is affected by the applied electric field, and other various mechanism for interwell transitions, i.e. electron–electron and acoustic phonon scattering. However, in both papers [16,17] the 1D Schrödinger equation was treated numerically without correcting for the different effective mass of the electron in the quantum wells and barrier. This problem has been resolved analytically by Allen and Richardson [4]. Exact analytical solutions for the 1D Schrödinger equation have been given, however, the results are not practical for the purpose of calculating the LO-phonon matrix element.

The aim of the present work is to calculate the tunnelling rates for interwell transitions due to electron–LO-phonon scattering in DQW heterostructures. The focus is on the investigation of the tunnelling rates as functions of the difference in energy between the E_1 level of the wider quantum well (QW1) and the E_1^* level of the narrower quantum well (QW2); see also Fig. 1. We present our resulting calculation in an analytical form taking into account the different effective mass of the electron in the quantum wells and barrier [18,19]. In our approximation we assume that the barrier height is much larger than the energy levels in the wells. Our calculations given for a semiconductor GaAs–AlGaAs heterostructure show that the rates due to LO-phonon assisted tunnelling are less sensitive to the energy difference $E_1 - E_1^*$ than those for coherent tunnelling, i.e. LO-phonon assisted tunnelling has a wider energy range than coherent tunnelling. As a result it is easier to achieve the efficient drain of carriers from lower subband by the assistance of LO-phonon scattering. Moreover, we also find that to get a better drain the design parameters of the quantum wells and barrier must be such that the energy difference is close to LO-phonon energy, i.e. $E_1 - E_1^* \approx 36$ meV.

2. Theoretical frameworks

A modified GaAs–AlGaAs DQW structure is schematically shown in Fig. 1. This is occasionally used as an intersubband lasing structure that consists of a wider well (QW1) as a lasing unit and a narrower well (QW2) as an electronic energy filter by various type of tunnelling mechanisms. To create lasing efficiency it is necessary to achieve a sufficient population inversion between subbands E_1 and E_2 in the QW1. This happens when the device has the appropriate design parameters providing a good electron confinement at the upper subband E_2 and short electron lifetime at the lower subband E_1. In this present work we are interested in studying how to reduce the electron lifetime at the lower level to a proper value for lasing operation. We have investigated a variation of tunnelling rates, $1/\tau_1$, of the electron as functions of the energy difference $E_1 - E_1^*$; here τ_1 is the tunnelling time of the electron. The notations E_1, E_2, and E_1^* stand for the electron states in each of the wells when isolated from each other (see Fig. 1).

We investigate a system where two potential wells are connected via a barrier which permits a measure of quantum mechanical tunnelling. We first simplify the system as shown in Fig. 1 by neglecting the effect of linear potential drop in the wells, and undertake it as a rectangular quantum well with finite-wall problem. However, to make the results more realistic we take into account finite barrier height in first approximation that gives for the effective well widths of QW1, QW2 and barrier thickness in terms of a_c, d_c and b_c, respectively, as follows [18–20]:

$$a_c = a + \delta_0 + \delta_1,\ b_c = b - \delta_1 - \delta_2,$$
$$d_c = d + \delta_2 + \delta_3 \qquad (1)$$

where a and d are the well widths of QW1 and QW2, respectively, b refers to the middle barrier thickness, $\delta_i = \hbar/\sqrt{2\alpha m_w^* U_i}$, $i = 0, 1, 2, 3$, where $\alpha = m_w^*/m_b^*$, m_w^* is the effective mass of the electron in the quantum wells while m_b^* is the effective mass of the electron in the barriers, and U_i are the heights of the barriers adjusted to the quantum wells that take into account the applied electric field, given as

$$U_0 = V_0 + \frac{eFa}{2},\ U_1 = V_0 - \frac{eFa}{2},\ U_2 = V_0 + \frac{eFd}{2},$$
$$U_3 = V_0 - \frac{eFd}{2} \qquad (2)$$

where V_0 is the conduction band off-set in the semiconductor heterostructure, F is the magnitude of the electric field, and e is the electronic charge. This

approach works well if the barrier is high enough, i.e. $\pi^2\hbar^2/2m_w^* d_c^2 \ll V_0$. However, the overlap integral, in fact, depends weakly on this correction. It is mainly determined by the energy difference.

By using the approach above and neglecting the exponentially small tails of the wavefunctions as they give a small contribution to the LO-phonon matrix element, the ground state wavefunctions in each of the wells when isolated from each other can be given by

$$\varphi_1(z) = \begin{cases} \sqrt{\frac{2}{a_c}} \sin\frac{\pi(z+\delta_0)}{a_c}; & -\delta_0 < z < z_1 + \delta_1 \\ 0 & \text{;otherwise} \end{cases}, \quad (3a)$$

$$\varphi_2(z) = \begin{cases} \sqrt{\frac{2}{d_c}} \sin\frac{\pi(z_3+\delta_3-z)}{d_c}; & z_2 - \delta_2 < z < z_3 + \delta_3 \\ 0 & \text{;otherwise} \end{cases}, \quad (3b)$$

where φ_1 and φ_2 stand for the unperturbed states E_1 and E_1^*, respectively. Because wells are coupled, one can assume that the eigen wavefunction of the system is a linear combination of φ_1 and φ_2. Therefore, the energy eigenvalues when wells are coupled are determined by the condition [13]

$$E^{(\pm)} = \left(\frac{E_1 + E_1^*}{2}\right) \pm \sqrt{\left(\frac{E_1 - E_1^*}{2}\right)^2 + M^2} \quad (4)$$

where M stands for the magnitude of the transfer integral. Using the approach introduced by Bar-Joseph and Gurvitz [21] we can calculate M as

$$M = \left(\frac{2}{\sqrt{a_c d_c}}\right)\left(\frac{\hbar^2\kappa}{m_b^*}\right)\left(\frac{E_1 E_1^*}{U_1 U_2}\right)^{1/2} \exp(-\kappa b), \quad (5)$$

where

$$\kappa = \frac{1}{2}\left[\sqrt{\frac{2m_b^*}{\hbar^2}(U_1 - E_1)} + \sqrt{\frac{2m_b^*}{\hbar^2}(U_2 - E_1^*)}\right].$$

Calculations show that the value of M is 3–5 meV depending on the electric field F. Experimental data reported by Li et al. [22] gives M as about 10 meV. The actual energy splitting given by Eq. (4) clearly depends on the magnitude of the transfer integral M.

With the introduction of $\varepsilon = E_1 - E_1^*/2$ and $\omega = \sqrt{\varepsilon^2 + M^2}$, the normalised eigen wavefunctions are

$$\varphi^{(\pm)}(z) = C_1^{(\pm)}\varphi_1(z) + C_2^{(\pm)}\varphi_2(z), \quad (6)$$

where

$$C_1^{(\pm)} = \frac{\mp M}{\sqrt{(\omega \mp \varepsilon)^2 + M^2}}, \text{ and}$$

$$C_2^{(\pm)} \frac{\omega \mp \varepsilon}{\sqrt{(\omega \mp \varepsilon)^2 + M^2}}.$$

The LO-phonon scattering rates. According to Fermi's golden rule, the scattering rates of an electron from an initial state $\left|i, \vec{K}_i\right\rangle$ in the ith subband to all final states $\left|f, \vec{K}_f\right\rangle$ in the fth subband accompanied by absorption or emission of a phonon with energy $\hbar\omega$ is [17]

$$\frac{1}{\tau_i} = \frac{2\pi}{\hbar} \times \int \left|\left\langle \vec{K}_f, f \left| \hat{H}_{e\text{-}ph} \right| i, \vec{K}_i \right\rangle\right|^2 \delta(\varepsilon_i - \varepsilon_f \mp \hbar\omega)\, dN_f \quad (7)$$

where $\vec{K}_i$ and $\vec{K}_f$ are in-plane wave vectors, and ε_i and ε_f are the total energies of the electron at the initial and final state, respectively. The upper (lower) sign refers to emission (absorption) of the phonon. In this expression the integration is over the number of final density of states N_f.

For the LO-phonon scattering mode the rate is therefore [17,23]

$$\frac{1}{\tau_i} = C_0 \times \int\int I_{if}(Q)\left(N_0 + \frac{1}{2} \pm \frac{1}{2}\right) \times \delta(E_i - E_f \mp \hbar\omega_0)\, d^2\vec{K}_f, \quad (8)$$

with the appropriate variables given as follows:

$$C_0 = \frac{2\pi}{\hbar}\frac{1}{(2\pi)^3}(2\pi\hbar\omega_0)\left(\frac{e^2}{4\pi\varepsilon_0}\right)\left[\frac{1}{\kappa_\infty} - \frac{1}{\kappa_0}\right], \quad (9)$$

$$Q = \sqrt{K_i^2 + K_f^2 - 2K_i K_f \cos\theta}, \quad (10)$$

where κ_∞ and κ_0 are the high-frequency and static dielectric constants of the quantum wells, ε_0 is the permittivity of vacuum, $\hbar\omega_0 = 36$ meV is the LO-phonon energy, N_0 is a phonon distribution function, $\hbar Q$ is the in-plane phonon momentum which is equal to the electron in-plane momentum transfer, and θ is the angle between $\vec{K}_i$ and $\vec{K}_f$. The integral $I_{if}(Q)$ is defined as [23]

$$I_{if}(Q) = \frac{\pi}{Q}\int\int \varphi_i(z)\,\varphi_f(z)\exp(-Q|z-z'|) \times \varphi_i(z')\,\varphi_f(z')\;dz'\,dz \tag{11}$$

At low temperature we neglect the induced phonon emission/absorption and take into account only a spontaneous phonon emission; i.e. $N_0 = 0$. Therefore, Eq. (8) reduces to

$$\frac{1}{\tau_i} = C_0\int\int I_{if}(Q)\,\delta(\varepsilon_i - \varepsilon_f - \hbar\omega_0)\;d^2K_f. \tag{12}$$

In polar coordinates $\vec{K}_f$ can be determined as follows:

$$d^2\vec{K}_f = K_f\,d\theta\,dK_f = \frac{m_w^*}{\hbar^2}d\phi\,d\varepsilon',$$

where $\varepsilon' = \varepsilon_f + \hbar\omega_0$, and the scattering rate is finally obtained

$$\frac{1}{\tau_i} = C_0\left(\frac{m_w^*}{\hbar^2}\right)\int_0^{2\pi} I_{if}(Q)\,d\theta. \tag{13}$$

In particular for GaAs–AlGaAs heterostructures we find that $C_0\left(m_w^*/\hbar^2\right) = 1.54\times10^{10}$ Å^{-1} s^{-1}. The scattering rate given by Eq. (13) clearly depends on the integral $I_{if}(Q)$ which can be determined by using Eq. (11) if the electron wavefunctions are known.

3. Results and discussion

In this section we discuss semi-analytical calculations of the tunnelling rates based on the physical model presented in the preceding section. Our calculations focus on the investigation of the tunnelling rates due to electron–LO-phonon scattering in the DQW structure as shown in Fig. 1. We simplify the integral $I_{if}(Q)$ given by Eq. (11) by considering the results only for an extreme condition of small Q values; i.e. $Q \ll q_z$.

By substituting wave functions given by Eq. (6) into Eq. (11) we obtain

$$I_{if}(Q) \cong \frac{\pi}{Q}\left\{\frac{\left(C_1^{(+)}C_1^{(-)}\right)^2}{1+0.207Qa_c} + \frac{\left(C_2^{(+)}C_2^{(-)}\right)^2}{1+0.207Qd_c} + \frac{2\,C_1^{(+)}C_1^{(-)}C_2^{(+)}C_2^{(-)}}{1+Q\left(a_c/2+b_c+d_c/2\right)}\right\} \tag{14}$$

and the magnitude of the in-plane phonon wave vector Q given in Eq. (10) can be written as

$$Q = \sqrt{\left(\frac{2m^*}{\hbar^2}\right)\hbar\omega_0\,\beta} \times\left[1+\left(1+\frac{(\gamma-1)}{\beta}\right) - 2\sqrt{1+\frac{(\gamma-1)}{\beta}}\cos\theta\right]^{1/2} \tag{15}$$

where β and γ are dimensionless parameters defined as follows:

$$\beta = \frac{\hbar^2K_i^2}{2m_w^*\hbar\omega_0},$$

$$\gamma = \frac{E^{(+)}-E^{(-)}}{\hbar\omega_0} = 2\,\frac{\sqrt{\left(E_1-E_1^*\right)^2+M^2}}{\hbar\omega_0}. \tag{16}$$

The expression for the tunnelling rate due to electron–LO-phonon scattering given by Eq. (13) associated with Eqs. (14)–(16) can be applied for any scattering processes from the ith subband to the fth subband. It clearly shows that the rate depends on both β and γ. However, in this present work we investigate for the case of $\beta \to 0$ limits, so that the rate is finally formulated as a functions of $E_1 - E_1^*$ and M. The calculations have been done for a semiconductor GaAs–AlGaAs DQW heterostructure with relevant characteristic parameters: $a = 66$ Å, $b = 26$ Å and $d = 33$ Å. In Fig. 2 we show the results for the tunnelling rates, Eqs. (13)–(16), for $M = 5$ meV and $M = 10$ meV as a function of the energy difference $E_1 - E_1^*$. In these plots as shown in Fig. 2 we also compare our results in this present work (solid line) with the rates calculated from coherent tunnelling (dashed line) [22].

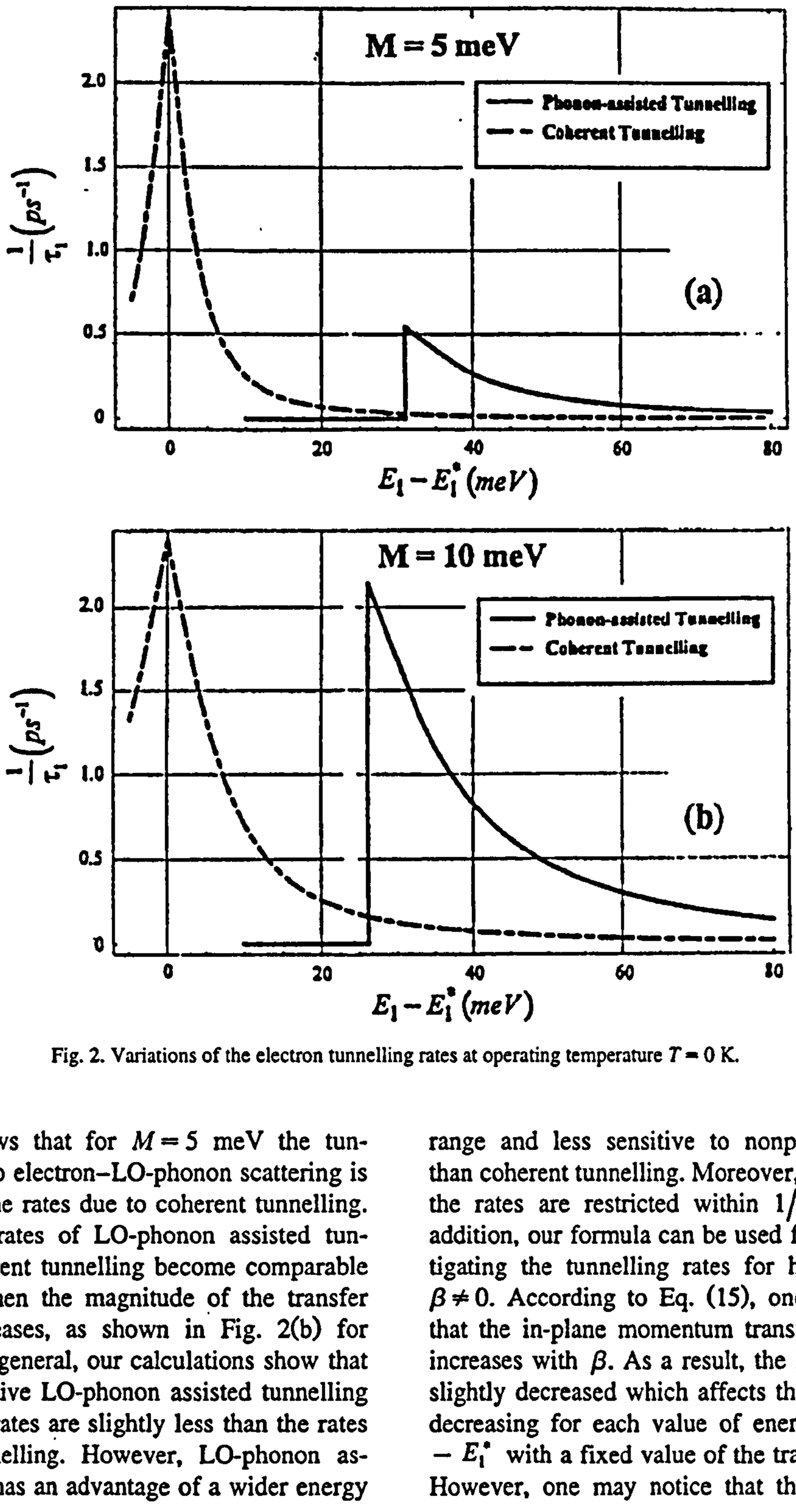

Fig. 2. Variations of the electron tunnelling rates at operating temperature $T = 0$ K.

Fig. 2(a) shows that for $M = 5$ meV the tunnelling rate due to electron–LO-phonon scattering is much less than the rates due to coherent tunnelling. However, these rates of LO-phonon assisted tunnelling and coherent tunnelling become comparable to each other when the magnitude of the transfer integral M increases, as shown in Fig. 2(b) for $M = 10$ meV. In general, our calculations show that we can get effective LO-phonon assisted tunnelling even though the rates are slightly less than the rates of coherent tunnelling. However, LO-phonon assisted tunnelling has an advantage of a wider energy range and less sensitive to nonparabolicity effect than coherent tunnelling. Moreover, we also find that the rates are restricted within $1/\tau \leq 2.5$ ps^{-1}. In addition, our formula can be used for roughly investigating the tunnelling rates for hot electrons, i.e. $\beta \neq 0$. According to Eq. (15), one can easily find that the in-plane momentum transfer $\hbar Q$ gradually increases with β. As a result, the integral $I_{if}(Q)$ is slightly decreased which affects the tunnelling rates decreasing for each value of energy difference $E_1 - E_1^*$ with a fixed value of the transfer integral M. However, one may notice that the maximum tun-

nelling rates for each value of M are almost independent of β.

4. Conclusions

Starting from the Fröhlich interaction and Fermi's golden rule, we can obtain Eq. (13) associated with Eqs. (14)–(16) for the tunnelling rates due to electron–LO-phonon scattering in semiconductor GaAs–AlGaAs DQW heterostructures. In general, the calculations mainly show that the tunnelling rates monotonically decrease with the energy difference, and strongly depend on the magnitude of the transfer integral. The rates are actually calculated at $T = 0$ K. However, the tunnelling rates formula given by Eq. (8) is quite simple and practical to generalise to other systems at $T \neq 0$ K. Another simplification we have made in this work is concerned with the third barrier. In our calculations we ignore the level width Γ in second quantum well (QW2). To make this assumption valid, we assume that $\Gamma \ll \hbar\omega_0$. On the other hand, the lifetime of the electron in QW2 ($\hbar/\Gamma$) should be much smaller than LO–phonon assisted tunnelling time (τ_1). For materials with small Fröhlich constant this condition is easily fulfilled; for GaAs, for example, 1.6 meV $\ll \Gamma \ll$ 36 meV. Practically, that means the thickness of the third barrier, 6 Å $< b_{RHS} <$ 30 Å for the QW2 of 33 Å well-width. For the large Γ threshold of the LO phonon emission smeared out for the value of Γ. Therefore, to calculate tunnelling rates more accurately for this case we have to treat the final states exactly as the states from the continuous spectrum. In this purpose we need to solve the 1D Schrödinger equation exactly, for example using the approach of Refs. [4,24].

In summary, we should mention that electron–electron scattering is also an effective inelastic scattering channel. In our geometry [3,13] the electron gas in front of the first barrier is likely to have suitable density to ensure effective inelastic scattering. To compare this calculation with experiments, we should also mention that only indirect measurements are available at the present moment. We found that the average phonon assisted tunnelling rate depends strongly on distribution function of in-plane kinetic energy. As a result, for any particular cases we need to know which part of distribution function is meaningful for the experiment. The results in our present work give a simple way to calculate this tunnelling time for various conditions and geometry's of the structure.

Acknowledgements

This work has been supported in part by EPSRC, and the Royal Thai Government as a part of providing a scholarship for S.K. The authors are also grateful to L.R. Wilson, J.P. Duck, J. W. Cockburn and M.S. Skolnick for various discussions.

References

[1] R.F. Kazarinov, R.A. Suris, Sov. Phys. Semicond. 6 (1972) 120.
[2] J. Faist, F. Capasso, D.L. Sivco, C. Sirtori, A.L. Hutchinson, A.Y. Cho, Science 264 (1994) 553.
[3] Y.B. Li, J.W. Cockburn, J.P. Duck, M.J. Birkett, M.S. Skolnick, I.A. Larkin, M. Hopkinson, R. Grey, G. Hill, Phys. Rev. B 57 (1998) 6290.
[4] S.S. Allen, S.L. Richardson, Phys. Rev. B 50 (1994) 11693.
[5] T.B. Boykin, J. Appl. Phys. 78 (1995) 6818.
[6] X.D. Zhao, H. Yamamoto, Y. Nakano, K. Taniguchi, Superlatt. Microstruct. 23 (1998) 1273.
[7] C. Wirner, Y. Awano, T. Mori, N. Yokoyama, T. Nakagawa, H. Bando, S. Muto, Appl. Phys. Lett. 69 (1996) 1596.
[8] L.D. Macks, S.A. Brown, R.G. Clark, R.P. Starrett, M.A. Reed, M.R. Deshpande, C.J.L. Fernando, W.R. Frensley, Phys. Rev. B 54 (1996) 4857.
[9] Y. Ji, Y. Chen, K. Luo, H. Zheng, Y. Li, C. Li, W. Cheng, F. Yang, Appl. Phys. Lett. 72 (1998) 3309.
[10] N. Zou, K.A. Chao, Phys. Rev. Lett. 69 (1992) 3224.
[11] P. Roblin, W.R. Liou, Phys. Rev. B 47 (1993) 2146.
[12] C.H. Grein, E. Runge, H. Ehrenreich, Phys. Rev. B 47 (1993) 12590.
[13] R. Tsu, G. Döhler, Phys. Rev. B 12 (1975) 680.
[14] D. Calecki, J.F. Palmier, A. Chomette, J. Phys. C 17 (1984) 5017.
[15] T. Weil, B. Vinter, J. Appl. Phys. 60 (1986) 3227.
[16] P. Harrison, Semicond. Sci. Technol. 12 (1997) 1487.
[17] R. Ferreira, G. Bastard, Phys. Rev. B 40 (1989) 1074.
[18] G. Bastard, Phys. Rev. B 24 (1981) 5693.
[19] Q.G. Zhu, H. Kroemer, Phys. Rev. B 27 (1983) 3519.
[20] L.D. Landau, E.M. Liftshitz, Quantum Mechanics: Nonrelativistic Theory, Pergamon Press, London, 1977.
[21] I. Bar-Joseph, S.A. Gurvitz, Phys. Rev. B 44 (1991) 3332.
[22] Y.B. Li, J.W. Cockburn, I.A. Larkin, J.P. Duck, M.J. Birkett, M.S. Skolnick, M. Hopkinson, R. Grey, G. Hill, Solid-State Electron. 42 (1998) 1533.
[23] P.J. Price, Ann. Phys. (N.Y.) 133 (1981) 217.
[24] D.C. Hutchings, Appl. Phys. Lett. 55 (1989) 1082.